TECHNICAL UNIVERSITY OF MUNICH

TUM SCHOOL OF NATURAL SCIENCES

DEPARTMENT OF PHYSICS

Master's Thesis in Physics

Development and Validation of a Fit to Extract Resonance Parameters of $\tau^- \to \pi^+\pi^-\pi^-\nu_\tau$ Decays at Belle II

Author:	Godo Kurten
1^{st} Examiner and Supervisor:	Prof. Dr. Stephan Paul
Advisor:	Dr. Stefan Wallner
Submission Date:	July 6, 2026

I confirm that this master's thesis in physics is my own work and I have documented all sources and material used.

Munich, July 6, 2026 Godo Kurten

Abstract

In the quark-model picture the simplest strongly bound systems are light mesons, which are modeled as quark-antiquark pairs, where each quark is an up, down or strange quark. As modeling the properties of these light mesons requires approximate methods, experimental input is required to validate them. For some resonances, such as the $a_1(1260)$, this experimental input is not very precise. In order to contribute a precise measurement, we develop an analysis of $\tau^- \to \pi^+\pi^-\pi^-\nu_\tau$ decays at Belle II to measure the masses and widths of a_1 and ρ-like mesons. These decays offer a clean environment, providing excellent conditions for precise measurements of resonances. In order to extract the resonance parameters, a partial-wave analysis is performed in a two-step approach. The first step disentangles the data into contributions of different partial waves that are identified by their quantum numbers, and measures their amplitudes as a function of the invariant mass of the 3π system $m_{3\pi}$. This step was already developed and tested in previous works. The second step models the $m_{3\pi}$ dependence of the partial waves explicitly, and extracts the masses and widths of the resonances in the partial waves. In this work we develop and validate this approach using simulated data. We find that the input model is recovered with small intrinsic analysis biases. For the $a_1(1260)$ the biases on mass and width are around $3\,\mathrm{MeV}/c^2$. For the other resonances they are slightly larger. In all cases they remain smaller than the uncertainties currently quoted by the Particle Data Group (PDG). Furthermore, we investigate our sensitivity to the $a_1(1420)$ signal found by the COMPASS collaboration. This signal has an unclear origin, as the quark-model picture does not predict such a meson. One possible origin is the triangle singularity. We determine the conditions under which we expect to differentiate between the hypothesis of a triangle singularity and a genuine resonance as the source of the $a_1(1420)$ signal. Lastly, we investigate the possibility of a more elaborate model for the second step, in which a K-matrix approach is implemented. We test its validity on our pseudo-data samples and determine the limitations of this approach.

Contents

1 Introduction

In our current understanding, four fundamental interactions govern our universe: gravitation, the electromagnetic, the strong and the weak interaction. Gravitation is described by general relativity [1], while the other three forces are combined in the framework of the Standard Model of particle physics (SM) [2]. The predictions of the SM have been tested rigorously against experimental observations, and no firmly established deviations have been observed to date. However, we know that the SM is not a complete theory, as it cannot explain important observations such as the nature of dark matter [3], or the matter-antimatter asymmetry observed in the universe [4].

The electromagnetic interaction is described in the SM by quantum electrodynamics (QED) [5, 6]. Exploring the excitation spectrum of the simplest electromagnetically bound system, the hydrogen atom, led to the development of QED. In the same way, mapping out the simplest strongly bound systems helped to develop and constrain the underlying theory of the strong interaction, quantum chromodynamics (QCD). The simplest strongly bound systems are mesons, which in the quark-model picture consist of a constituent quark and antiquark pair [7, 8]. We categorize a meson as a light meson if it is built from up, down or strange quarks.

QCD describes the interactions between strongly interacting particles, i.e., quarks and gluons. At energy scales of about 1 GeV, the strong coupling constant α_S is large, and QCD cannot be solved perturbatively. Since mesons lie in this low-energy regime, first-principles QCD predictions for the mesonic states are very limited. However, it is possible to solve QCD numerically at low energies with a method called lattice QCD [9]. These numerical calculations often require simplifying assumptions, such as unphysically heavy quark masses, with the results subsequently extrapolated to the physical limit. To verify these predictions, it is necessary to map out the mesonic excitation spectrum through measurements.

One promising way to study the mesonic excitation spectrum is through τ-lepton decays, as their high mass of $m_\tau = (1776.93 \pm 0.09)\,\mathrm{MeV}/c^2$ [10] allows them to decay hadronically. τ^- leptons are produced in large numbers at B-factories such as Belle II, where they decay in a particularly clean environment, as few additional

Table 1.1: Resonance parameters as listed by the Particle Data Group [10]. The left column lists the resonance name. The two following columns summarize the estimate on the masses and widths of these resonances. For some resonances only a range for the width was listed.

Resonance	Mass [MeV/c^2]	Width [MeV/c^2]
$a_1(1260)$	1230 ± 40	250-600
$a_1(1640)$	1655 ± 16	250 ± 40
$\pi(1300)$	1300 ± 100	200-600
$\rho(1450)$	1465 ± 25	400 ± 60

particles accompany the reaction. About 9 % of τ^- decays proceed into the $\pi^+\pi^-\pi^-\nu_\tau$[1] channel [10], making the $\tau^- \to \pi^+\pi^-\pi^-\nu_\tau$ decay an excellent opportunity to study the mesonic excitation spectrum. Extracting the spectrum requires identifying and measuring the mesonic resonances in the data sample, which is done by performing a partial-wave analysis (PWA).

Several experiments have performed measurements of the excitation spectrum of light-meson resonances. We will discuss two of these experiments. The COMPASS collaboration measured both non-strange and strange light-mesons in diffractive scattering of a π^- or a K^- impinging on a hydrogen target, decaying into, e.g., $\pi^+\pi^-\pi^-$ [11, 12] and $K^-\pi^+\pi^-$ [13, 14] final states, respectively. The Belle collaboration [15] in Japan has also performed hadron-spectroscopy measurements as reviewed in ref. [16]. We would like to highlight one preliminary measurement, in which $\tau^- \to \pi^+\pi^-\pi^-\nu_\tau$ decays were studied [17, 18]. This preliminary analysis demonstrated that a PWA of this channel is feasible and motivates a dedicated measurement at Belle II.

Although the mesonic excitation spectrum has already been thoroughly investigated, there still remain many open questions. In particular, many parameters of the mesonic excitation spectrum remain poorly determined. Table 1.1 lists resonances that we expect to contribute in our data sample as well as their resonance parameters, i.e., their masses and widths, as the Particle-Data Group (PDG) lists them. Many of these resonance parameters are not precisely known. The $a_1(1260)$ resonance, for example, is only listed with a range for its width, as many measurements yield widely varying values. Conventionally, the resonances are parametrized using the Breit–Wigner amplitude, which is an approximation valid for narrow and isolated resonances. As the $a_1(1260)$ is rather wide for its mass, this approximation may break down, which could contribute to the large spread in the measured values. More elaborate models, such as a K-matrix approach [19], that do not rely on the assumption of narrow isolated resonances may provide a cleaner extraction of resonance parameters.

[1] The charge-conjugated case is always implied, even if it is not explicitly written.

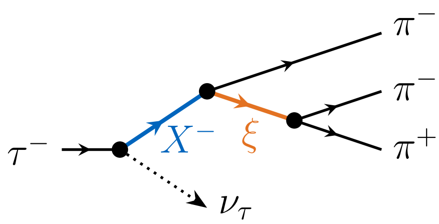

Figure 1.1: Illustration of the $\tau^- \to \pi^+\pi^-\pi^-\nu_\tau$ decay over an intermediate resonance X^-.

Another open question concerns the $a_1(1420)$ signal that was observed by the COMPASS collaboration in their $\pi^- + p \to \pi^+\pi^-\pi^- + p$ diffractive scattering data, whose origin is disputed [20, 21]. It does not fit quark-model expectations[2]. One possible explanation is that it is not a genuine resonance but a triangle singularity, where first an $a_1(1260)$ is produced, whose decay products then rescatter in a certain way that produces a signal like the one observed by COMPASS. Due to large background contributions in the COMPASS data, no final conclusion could be drawn on the nature of the $a_1(1420)$ signal. The same signal was observed in the preliminary Belle analysis of $\tau^- \to \pi^+\pi^-\pi^-\nu_\tau$ decays [17, 18].

In order to study these resonances and to separate their contributions, the analysis needs to disentangle the different intermediate states in the 3π final state. To this end, the isobar model [22, 23] is employed. In the isobar model, the decay is modeled as two subsequent decays, as visualized in fig. 1.1. The τ^- first decays into an intermediate state X^- with spin-parity quantum numbers J^P. The intermediate state then decays into one π^- and an isobar ξ^0, which subsequently decays into the final 2π. One possible combination of J^P quantum numbers with a specific decay mode is called a partial wave. The PWA is performed in a two-step approach. First, the data is disentangled into the contributions of the different partial waves in a partial-wave decomposition (PWD), in which the dependence of each partial wave on the invariant mass $m_{3\pi}$ of the 3π final state is measured. After this step, the yields of the partial waves, i.e., the number of modeled events in a partial wave, can be extracted. Second, the mass dependence of these contributions is modeled explicitly in the resonance-model fit (RMF), from which the resonance content and its properties, such as mass and width, are extracted. From the RMF result we additionally obtain the yields of the intermediate resonances, i.e., the number of modeled events in an intermediate state. Both the partial wave and intermediate resonance yields are necessary to determine fit fractions. The PWD was already developed in previous works by refs. [24, 25].

As per the unblinding rules of the Belle II collaboration, the full analysis chain must

[2] See chapter 9 for a list of reasons.

be validated on simulated data before real experimental data can be used, which is why all studies shown in this work are carried out on Belle II Monte-Carlo pseudo-data with a known input model. This validation requires many dedicated studies, each of which involves performing several PWDs. As one goal of this thesis, we therefore develop a streamlined execution of the PWD that allows these studies to be carried out quickly and reproducibly. The main goal of this thesis is to develop and validate the RMF. To this end, we extract the resonance parameters and yields and compare them to their input values, which lets us assess the intrinsic biases of the analysis chain. We further investigate how these biases compare to the uncertainties currently quoted by the PDG. We then study the conditions under which we could determine whether the $a_1(1420)$ signal originates predominantly from a triangle singularity or from a genuine resonance. Finally, we implement the K-matrix approach in the RMF and investigate under which conditions it reproduces our expectations and where its limitations lie.

The thesis is structured as follows. Chapter 2 introduces the Belle II detector and the SuperKEKB accelerator. In chapter 3 we discuss the event reconstruction and the selection that we impose to obtain a clean $\tau^- \to \pi^+\pi^-\pi^-\nu_\tau$ data sample. This is followed by chapter 4, where the full PWD formalism used in this work is explained. The streamlining of the analysis pipeline is described in chapter 5. The RMF formalism is then introduced in chapter 6. Chapter 7 presents the analysis setup common to all subsequent studies: the input model, the Monte-Carlo samples and pseudo-data generation, the PWD model, and the base RMF model used throughout this work. In chapter 8 we perform input-output studies to assess the intrinsic biases of the analysis chain. In chapter 9 we investigate our sensitivity to distinguish the nature of the $a_1(1420)$ signal. Chapter 10 discusses our implementation of the K-matrix approach and investigates its validity and limitations. Finally, in chapter 11 we summarize the most important aspects of this work and provide an outlook on the further development of this analysis.

2 Belle II

The Belle II experiment is located at the SuperKEKB accelerator in Tsukuba, Japan. Like its predecessor, the Belle experiment at the KEKB accelerator, it uses electron-positron (e^+e^-) pairs accelerated to center-of-mass energies around the $\Upsilon(4S)$ resonance mass. The $\Upsilon(4S)$ has a branching fraction of over 96 % to the $B\bar{B}$ decay channel [10], which is the origin of its designation as a B-factory. The collisions do not only produce vast numbers of B-mesons, but also other particles, such as $\tau^+\tau^-$ pairs (see table 2.1).

The main goal of the Belle II experiment is to use all of the produced particles to search for flavor physics phenomena, as well as perform precise measurements of Standard Model (SM) parameters, either confirming the SM's predictions or revealing discrepancies that point to physics beyond it. In this thesis the simulated τ^--lepton pairs produced in e^+e^- scattering events are analyzed.

Section 2.1 introduces the SuperKEKB accelerator. Section 2.2 introduces the main detector components of the Belle II experiment, and how these components measure the final-state particles. A detailed overview of SuperKEKB and Belle II can be found in refs. [26, 27], which provide the basis of this chapter.

Table 2.1: Cross-section of $e^+e^- \to f\bar{f}$ at center-of-mass energies of 10.58 GeV. Table adapted from ref. [28].

$e^+e^- \to$	Cross-section [nb]
e^+e^-	40
$\mu^+\mu^-$	1.16
$\tau^+\tau^-$	0.94
$b\bar{b}$	1.05
$c\bar{c}$	1.30
$s\bar{s}$	0.35
$u\bar{u}$	1.39
$d\bar{d}$	0.35

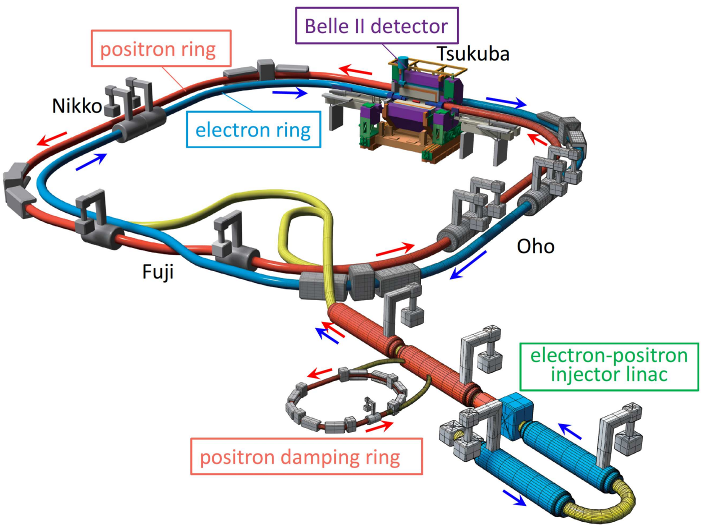

Figure 2.1: Schematic view of the SuperKEKB accelerator. Figure taken from ref. [29].

2.1 SuperKEKB Accelerator

SuperKEKB first accelerates electrons and positrons in the injector linear accelerator (linac) to 7 GeV and 4 GeV, respectively. The electrons and positrons are then injected into the high-energy ring (HER) and low-energy ring (LER), respectively. Both rings have a circumference of 3 km. The two beams collide at the interaction point (IP), around which the Belle II detector is built (see fig. 2.1), with a center-of-mass energy of $\sqrt{s} = 10.58\,\mathrm{GeV}$. The asymmetric beam energies yield movement of the $\Upsilon(4S)$ and its $B\bar{B}$ decay products along the e^--direction in the laboratory frame, spatially separating the decay vertices of the two B mesons and thereby enabling decay-time-dependent measurements. The performance of the accelerator can be quantified by its luminosity $\mathcal{L}$, which corresponds to a proportionality factor between the event rate $\frac{\mathrm{d}N}{\mathrm{d}t}$ and the cross section σ of a given process:

$$\frac{\mathrm{d}N}{\mathrm{d}t} = \mathcal{L}\sigma. \tag{2.1}$$

SuperKEKB was designed to reach luminosities of up to $8 \times 10^{35}\,\mathrm{cm}^{-2}\,\mathrm{s}^{-1}$, which is 40 times larger than the previous KEKB peak luminosity [29]. This is achieved using the so-called nano-beam scheme, in which the transverse beam size at the IP is reduced by a factor of roughly 20 compared to KEKB, down to approximately 50 nm, while the beam currents are approximately doubled. At the end of May 2026, SuperKEKB achieved a new world record luminosity of $5.281 \times 10^{34}\,\mathrm{cm}^{-2}\,\mathrm{s}^{-1}$ [30]. The total dataset size is quantified by the time-integrated luminosity:

$$\mathcal{L}_{\mathrm{int}} = \int_0^T \mathcal{L}(t')\mathrm{d}t'. \tag{2.2}$$

The final goal of Belle II is a total integrated luminosity of $50\,\mathrm{ab}^{-1}$, about 50 times higher than what Belle collected [31]. So far, the Belle II experiment has recorded about $900\,\mathrm{fb}^{-1}$ of integrated luminosity [32].

2.2 Belle II Detector

The Belle II detector surrounds the IP, as shown in fig. 2.2. It is composed of several subdetectors that measure various quantities, such as the position, momentum, energy, and species of particles. From the IP outwards, the subdetectors are:

1. Tracking detectors, that reconstruct charged-particle tracks and decay vertices (see section 2.2.3), consisting of:
    - Pixel Vertex Detector (PXD)
    - Silicon Vertex Detector (SVD)
    - Central Drift Chamber (CDC)
2. Particle-Identification Detectors (PID), that reconstruct the particle species (see section 2.2.4), consisting of:
    - Time-Of-Propagation Counter (TOP)
    - Aerogel Ring-Imaging CHerenkov Detector (ARICH)
3. Electromagnetic Calorimeter (ECL), that measures the energy of γ and $e^{\pm}$ (see section 2.2.5)
4. Detector Solenoid, that generates a magnetic field to enable momentum measurement of charged particles (see section 2.2.2)
5. K_L^0 and μ Chamber (KLM), that specifically detects K_L^0 and μ particles that have not been detected by the inner subdetectors (see section 2.2.6)

Overall, the Belle II detector has a width and height of about $8\,\mathrm{m}$ and weighs about $1400\,\mathrm{t}$.

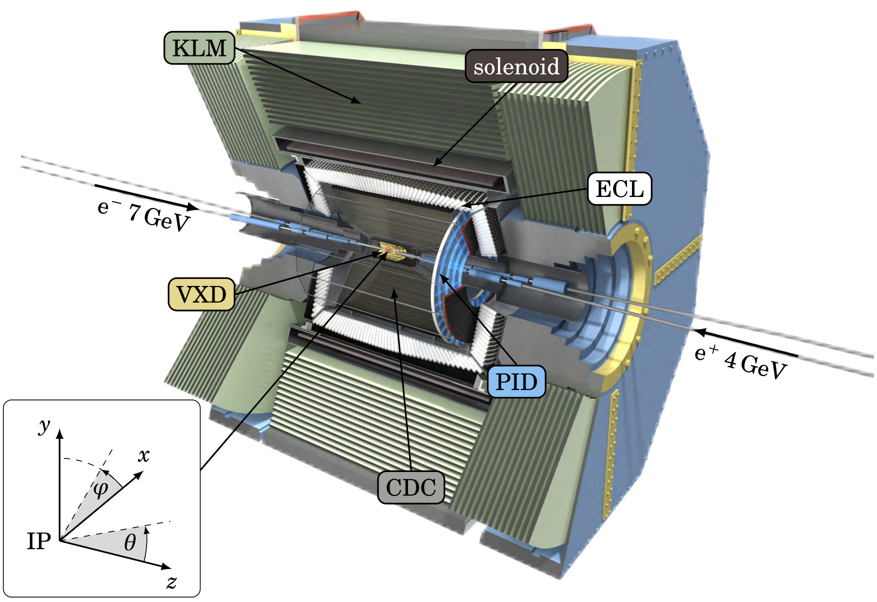

Figure 2.2: Schematic view of the Belle II detector. The individual subdetectors are labeled. The coordinate system with its origin in the IP is shown in the box. Figure taken from ref. [33].

2.2.1 Coordinate System

The coordinate system of Belle II is defined in ref. [34] as a right-handed coordinate system. The IP is used as the origin. The bisector of the two beams defines the z-axis, with its positive direction along the e^--beam. The y-axis points upwards. The x-axis is perpendicular to both the y- and z-axes, pointing radially outwards from the center of the accelerator ring. As can be seen in fig. 2.2, the azimuthal angle φ is the angle of the position vector of a point measured counterclockwise from the x-axis around the z-axis. The polar angle θ is the angle between the z-axis and the position vector of a point.

2.2.2 Detector Solenoid

While the solenoid is technically not a detector, it is a crucial part of the experiment. The magnetic field bents charged particles onto helical trajectories, allowing the determination of momentum from the radius of curvature of the particle tracks. To this end, Belle II uses a superconducting solenoid that generates a magnetic field of 1.5 T within a cylindrical volume of 3.4 m in diameter and 4.4 m in length surrounding the ECL.

2.2.3 Tracking

The tracking of charged particles is performed using three distinct detectors, the PXD, SVD and CDC. These detectors cover the full azimuthal angle range and polar angles from 17 to 150°. They have to fulfill different requirements as they are positioned at different distances from the IP. The following will discuss each subdetector.

Pixel Vertex Detector (PXD)

The PXD consists of two layers with radii of 14 and 22 mm. Due to the high beam-induced background close to the IP, the occupancy in this region would be too high for strip-based detectors. Pixel detectors provide finer segmentation, keeping the occupancy at a manageable level while also providing precise position measurements for vertex reconstruction. The pixels are based on the DEPleted Field Effect Transistor (DEPFET) technology. A charged particle ionizes the fully depleted silicon bulk by passing through it. This creates electron-hole pairs that are collected and converted to an electrical signal by the readout electronics [35].

Silicon Vertex Detector (SVD)

Following the innermost two layers of the PXD, the SVD adds 4 additional layers with radii of 38, 80, 115, and 140 mm. The SVD consists of double-sided silicon strip detectors. At larger distances from the IP, the beam-induced background is sufficiently reduced for strip detectors to be used instead of pixels, while still providing precise vertex reconstruction. The basic function of this detector is the similar the PXD.

Central Drift Chamber (CDC)

The CDC is located around the PXD and SVD. It is a cylindrical chamber with 56 total layers of sense wires, grouped into 9 superlayers. These layers alternate in their orientation relative to the beam axis. Axial wires align with the beam axis, while stereo wires are oriented at angles of 45.4 to 74 mrad relative to the beam axis. The angles are chosen in both positive and negative directions to enable full 3D track reconstruction.

Unlike the PXD and SVD, the CDC is not a semiconductor-based detector. It is based on drift chamber technology. Charged particles passing through the detector ionize the $He{-}C_2H_6$ gas mixture. The ionization electrons drift toward the nearest sense wire, where an avalanche is induced. The drift time, combined with the known electron drift velocity in the gas, yields the distance of the particle's track from the wire [35].

The CDC also provides PID information in addition to tracking. The charged particles lose energy while traversing the gas mixture. For the fixed gas mixture of the CDC, the energy loss per unit distance $\mathrm{d}E/\mathrm{d}x$ through ionization of the gas depends only on the velocity of the singly-charged particle. Thus, measuring $\mathrm{d}E/\mathrm{d}x$ provides the velocity of the particle. The ratio β of the particle's velocity v to the speed of light c, given by

$$\beta = \frac{v}{c} = \frac{1}{\sqrt{1 + \frac{m^2c^2}{p^2}}}, \tag{2.3}$$

provides a unique relationship between velocity, mass and momentum of a particle. When the knowledge on the momentum of a particle from tracking is combined with its velocity, the particle's mass can be determined, which is characteristic for its species [10].

2.2.4 Particle-Identification (PID)

The PID detectors reconstruct the species of charged particles. Although the CDC already provides information on the particle's species at low momenta via $\mathrm{d}E/\mathrm{d}x$, the TOP and ARICH are dedicated PID detectors, which extend the PID capability to higher momenta where the $\mathrm{d}E/\mathrm{d}x$ curves of different species are too similar to separate. Both of these detectors determine the particle's species by relying on the Cherenkov radiation emitted by particles. When a charged particle moves through a material faster than light would propagate in that material, Cherenkov radiation is emitted. The angle θ_C under which the Cherenkov radiation is emitted is given by the relation:

$$\cos\theta_C = \frac{1}{n\beta}, \tag{2.4}$$

where n is the known refractive index of the radiator material and β is as defined in eq. (2.3). Both TOP and ARICH measure the Cherenkov angle θ_C as discussed in the following. With knowledge of the refractive index in both TOP and ARICH, the particle's speed β is determined. As discussed in section 2.2.3 for the CDC, the particle's velocity together with its momentum provides its species.

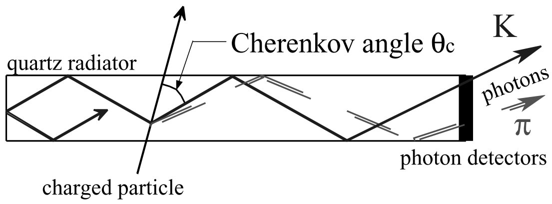

Figure 2.3: Schematic view of the TOP detector. Cherenkov photons are generated in a quartz radiator and detected by photon detectors. The arrival time of the photons and their impact position are used for particle identification. Figure taken from ref. [27].

Time-Of-Propagation Counter (TOP)

The TOP is located in the central cylindrical region of the Belle II detector, referred to as the barrel region. When a particle passes through the quartz bar of the TOP, Cherenkov photons are generated, as can be seen in fig. 2.3. These photons are then internally reflected within the quartz bars until they reach the micro-channel plate photomultiplier tubes (MCP-PMTs). The MCP-PMTs measure the exact time and impact position of the arriving photons. Together with the known particle trajectory from tracking, which provides the emission point along the bar, the Cherenkov angle is reconstructed from the photon arrival time and impact position on the MCP-PMTs.

Aerogel Ring-Imaging Cherenkov Detector (ARICH)

The ARICH is positioned in the forward endcap, i.e., in the direction of the e^--beam. The charged particles pass through 2 cm of aerogel radiator generating Cherenkov radiation (see fig. 2.4). The photons then propagate through 20 cm of expansion volume, allowing Cherenkov rings to form. Using Hybrid Avalanche Photo-Detectors (HAPD) the position and radius of the Cherenkov rings are determined. From the radius of the rings, the Cherenkov angle is reconstructed. The ARICH is designed to separate kaons from pions in the momentum range of 0.4 to 4 GeV/c.

2.2.5 Electromagnetic Calorimeter (ECL)

The ECL measures the energy deposited by particles passing through it. It was specifically designed to fully contain electromagnetic showers produced by photons and electrons, allowing their full energy to be determined precisely. Hadrons also leave energy

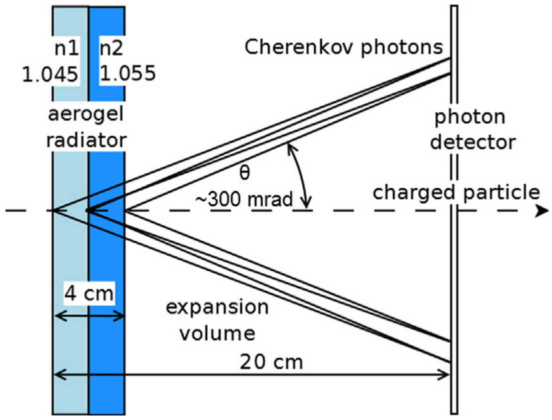

Figure 2.4: Schematic view of the ARICH detector. Cherenkov photons are generated in two layers of aerogel radiator and detected by photon detectors. The radius of the resulting Cherenkov ring, determined from the photon impact positions, encodes the Cherenkov angle and is used for particle identification. Figure taken from ref. [36].

in the ECL by ionisation or small hadronic showers. However, hadrons are generally not fully contained in the ECL and deposit only a fraction of their energy there, before being detected by the KLM. The ECL is therefore crucial to determine the energy of photons and π^0 as they are uncharged and leave no track. The ECL consists of a barrel section and forward and backward endcaps, covering in total a polar angle range of 12.4 to 155.1°. It is equipped with 8736 thallium-doped caesium iodide crystals. These crystals induce electromagnetic showers when incoming photons and electrons interact with them. Each crystal is paired with two photodiodes, which are used to measure the magnitude and timing of energy deposits in the detector.

2.2.6 K_L^0 and μ Chamber (KLM)

The last and outermost detector is the KLM. Its main purpose is to detect K_L^0 and μ that are not fully absorbed by the inner detectors. The KLM covers a polar angle range of 25 to 155°. It consists of alternating layers of iron plates and active detector elements. The iron plates serve a dual purpose: as absorber material for incoming particles and as the flux return yoke for the solenoid. In the barrel region, glass-electrode resistive plate chambers (RPCs) are used as detector elements. In the endcaps, the background is worse than in the barrel region due to limited shielding of particles generated externally along the beam lines. The large dead time of the RPCs results in efficiencies below 50 % in this region; therefore silicon photomultipliers (SiPMs) are used in the endcaps as detector material.

K_L^0 and μ create different signatures in the KLM, allowing these two particle types to be distinguished. K_L^0 mesons, as well as other neutral hadrons that reach the KLM, produce hadronic showers in the iron plates of the KLM, while μ leptons traverse the detector as minimum-ionising particles, depositing only small amounts of energy in each layer.

3 Event Selection

This chapter describes the procedure used to select a sample of $\tau^- \to \pi^+\pi^-\pi^-\nu_\tau$ events. The selection is performed in three consecutive stages. First, the event topology is established and the relevant particle candidates are reconstructed. Second, kinematic cuts are applied to suppress background contributions while retaining signal events with high efficiency. Third, multivariate analysis (MVA) techniques and PID criteria are used to obtain a sample purity sufficient for the subsequent partial-wave analysis.

The selection is based on the event selection used for a measurement of $|V_{us}|$ using hadronic τ^- decays at Belle II [37], which was refined to meet the purity requirements of our partial-wave analysis. The summary of the refined selection can be found in ref. [38]. As the real experimental data remain blinded under the Belle II unblinding policy, a run-dependent Belle II Monte-Carlo data sample is used for the development of the selection. Run-dependent Monte Carlo reproduces the detector and beam-background conditions of the individual data-taking periods, so that the simulation matches the conditions under which the corresponding data were recorded. It provides a realistic description of both signal and background contributions under run-dependent detector conditions. This sample is referred to as the MC15rd sample thereafter. The MC15rd sample is weighted by luminosity to correspond to a dataset with an integrated luminosity of $\mathcal{L} = 361.654\,\mathrm{fb}^{-1}$.

This chapter outlines the variables used for the selection process in section 3.1. Section 3.2, section 3.3, and section 3.4 summarize the employed event reconstruction, preselection, and fine selection, respectively. Section 3.5 summarizes the expected background components still found in the final data sample after the selection process.

3.1 Phase Space Variables

Our data samples contain the four-momenta p_i of the particles measured by the detector. We order the three pions in the final state such that $\tau^- \to \pi_1^+\pi_2^-\pi_3^-\nu_\tau$, where $|\vec{q}_3| > |\vec{q}_2|$

in the rest frame of the $\pi^+\pi^-\pi^-$ system, with $\vec{q}_i$ denoting the three-momentum of π_i in the 3π rest frame. Using these four-momenta, we can calculate the phase-space variables. The four-momenta comprise 16 kinematic variables. Due to energy-momentum conservation and the known masses of the final-state particles, the phase space is fully described by eight independent variables, e.g., three invariant-mass variables and five angular variables. We collectively denote this full set of phase-space variables by τ[1]. Since the neutrino escapes detection at Belle II, two of the five angular variables cannot be determined. The mass variables will be discussed in section 3.1.1. The angular variables will be discussed in section 3.1.2.

3.1.1 Mass Variables

The three invariant-mass variables are constructed from the four-momenta of the pions. The invariant mass of the 3π system is given by:

$$m_{3\pi} = \sqrt{\left(\sum_{i=1}^{3} p_i\right)^2}. \tag{3.1}$$

Additionally, two invariant masses of two-pion subsystems are necessary for full parametrization of the phase space:

$$m_{12} = \sqrt{(p_1 + p_2)^2}, \qquad m_{23} = \sqrt{(p_2 + p_3)^2}. \tag{3.2}$$

The third two-pion invariant mass m_{13} can be calculated from m_{12}, m_{23} and $m_{3\pi}$.

3.1.2 Angular Variables

The system is additionally described by five angles: three Euler angles $(\alpha, \cos\beta, \gamma)$ and two helicity angles $(\cos\theta, \Phi)$. Due to the ν_τ not being measured by the detector, α and Φ cannot be determined and are integrated over. Our angles are defined following the convention of ref. [39, 40].

Euler Angles

The three Euler angles fix the orientation of the 3π decay plane within the 3π rest frame, and we extract them geometrically from the pion momenta in that frame. Two

[1] Throughout this thesis, τ as a standalone symbol refers to a point in phase space and should not be confused with the τ^- lepton, which carries its charge explicitly (e.g. τ^-, $\tau^+\tau^-$) or appears in subscripts such as m_τ and E_τ.

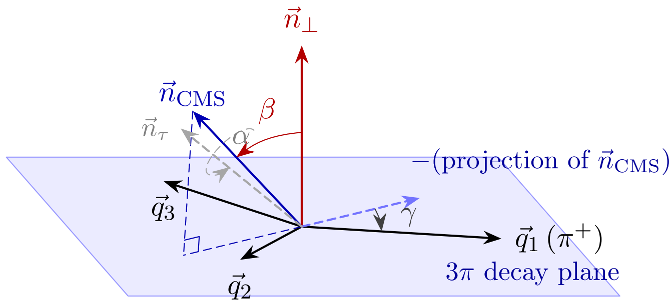

Figure 3.1: Geometric definition of the Euler angles for $\tau^- \to \pi^+\pi^-\pi^-\nu_\tau$. The pion momenta $\vec{q}_i$ span the 3π decay plane with normal $\vec{n}_\perp$ (see eq. (3.4)). The polar angle β is the angle between $\vec{n}_\perp$ and $\vec{n}_{\text{CMS}}$ (see eq. (3.5)), the vector opposite to the summed three-pion momenta in the CMS frame. γ is measured within the decay plane from the projection of $-\vec{n}_{\text{CMS}}$ to $\hat{q}_1$ (see eqs. (3.6) and (3.7)). The angle α (see eqs. (3.9) and (3.10)) is the azimuth about $\vec{n}_{\text{CMS}}$, measured between the projections of $\vec{n}_\perp$ and of the τ^- flight direction $\vec{n}_\tau$ onto the plane perpendicular to $\vec{n}_{\text{CMS}}$. Since $\vec{n}_\tau$ is not measurable, α cannot be determined.

reference directions are needed. The first, $\vec{n}_{\text{CMS}}$, points opposite to the summed three-pion momentum measured in the center-of-mass (CMS) frame of the e^+e^- system:

$$\vec{n}_{\text{CMS}} = -\frac{\vec{p}_1^{\,*} + \vec{p}_2^{\,*} + \vec{p}_3^{\,*}}{|\vec{p}_1^{\,*} + \vec{p}_2^{\,*} + \vec{p}_3^{\,*}|}, \tag{3.3}$$

where a * marks quantities evaluated in the CMS frame. The second, $\vec{n}_\perp$, is the normal to the 3π decay plane:

$$\vec{n}_\perp = \frac{\vec{q}_2 \times \vec{q}_3}{|\vec{q}_2 \times \vec{q}_3|}, \tag{3.4}$$

with $\vec{q}_i$ the pion three-momenta in the 3π rest frame. From these two directions the Euler angles follow as illustrated in fig. 3.1. The cosine of the polar angle β is obtained from the projection of $\vec{n}_\perp$ onto $\vec{n}_{\text{CMS}}$:

$$\cos\beta = \vec{n}_{\text{CMS}} \cdot \vec{n}_\perp. \tag{3.5}$$

For γ we evaluate $\sin\gamma$ and $\cos\gamma$ separately,

$$\sin\gamma = \frac{(\vec{n}_{\text{CMS}} \times \vec{n}_\perp) \cdot \hat{q}_1}{|\vec{n}_{\text{CMS}} \times \vec{n}_\perp|}, \tag{3.6}$$

$$\cos\gamma = -\frac{\vec{n}_{\text{CMS}} \cdot \hat{q}_1}{|\vec{n}_{\text{CMS}} \times \vec{n}_\perp|}, \tag{3.7}$$

where $\hat{q}_1$ is the unit vector along the π^+ momentum in the 3π rest frame, and recover the angle through

$$\gamma = \text{atan2}(\sin\gamma, \cos\gamma). \tag{3.8}$$

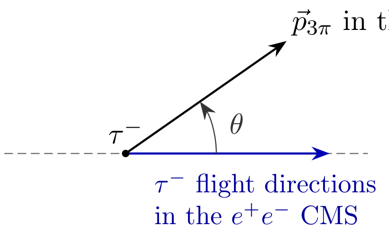

Figure 3.2: Illustration of the helicity angle θ between the τ^- flight direction in the CMS frame and the flight direction of the X^- system in the τ^- rest frame.

The remaining angle α additionally involves the τ^- flight direction $\vec{n}_\tau$ in the 3π rest frame. Its sine and cosine read

$$\sin\alpha = -\frac{\vec{n}_\tau \cdot (\vec{n}_{\mathrm{CMS}} \times \vec{n}_\perp)}{|\vec{n}_{\mathrm{CMS}} \times \vec{n}_\tau||\vec{n}_{\mathrm{CMS}} \times \vec{n}_\perp|} \tag{3.9}$$

$$\cos\alpha = \frac{(\vec{n}_{\mathrm{CMS}} \times \vec{n}_\tau) \cdot (\vec{n}_{\mathrm{CMS}} \times \vec{n}_\perp)}{|\vec{n}_{\mathrm{CMS}} \times \vec{n}_\tau||\vec{n}_{\mathrm{CMS}} \times \vec{n}_\perp|}, \tag{3.10}$$

so that

$$\alpha = \mathrm{atan2}(\sin\alpha,\, \cos\alpha). \tag{3.11}$$

In our decays, however, $\vec{n}_\tau$ is not accessible: the escaping neutrino prevents a reconstruction of the τ^- flight direction, and α therefore cannot be determined.

Helicity Angle

The helicity angle θ in the $\tau^- \to X^-\nu_\tau$ decay corresponds to the angle between the τ^- flight direction in the CMS frame and the flight direction of the X^- system in the τ^- rest frame as illustrated in fig. 3.2. We can not reconstruct the τ^- rest frame due to the escaping neutrino. However, we kinematically reconstruct this angle using four-momentum conservation from the energy of the hadronic system as:

$$\cos\theta = \frac{2E_{3\pi}\frac{m_\tau^2}{E_\tau} - m_\tau^2 - m_{3\pi}^2}{(m_\tau^2 - m_{3\pi}^2)\sqrt{1 - \frac{m_\tau^2}{E_\tau^2}}}, \tag{3.12}$$

where $E_{3\pi}$ is the energy of the 3π system in the CMS frame, and E_τ and m_τ are the energy in the CMS frame and mass of the τ^- lepton, respectively.

3.2 Event Reconstruction

The SuperKEKB collider operates at a CMS energy of $E_{\mathrm{CMS}} = 10.58\,\mathrm{GeV}$, producing about 340×10^6 $\tau^+\tau^-$ pairs via $e^+e^- \to \tau^+\tau^-$ in $361.654\,\mathrm{fb}^{-1}$ of integrated luminosity.

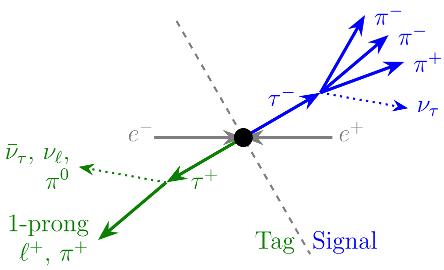

Figure 3.3: Illustration of the tag and signal side decay of the $\tau^+\tau^-$ pair produced in e^+e^- collisions in the CMS. Tag and signal side are separated by the gray thrust axis. Figure taken from ref. [25].

The τ^--leptons have a boost of $\beta\gamma = 2.804$, and an average lifetime of 290×10^{-15} s [10]. They thus have a mean decay length of about 244 µm and therefore decay before reaching any detector element. In the CMS frame, the $\tau^+\tau^-$ pairs are produced back-to-back, which provides a natural separation of their decay products. We divide the event into two hemispheres using the thrust T, defined as

$$T = \max_{\hat{n}} \frac{\sum_i |\vec{p}_i^{\,*} \cdot \hat{n}|}{\sum_i |\vec{p}_i^{\,*}|}, \tag{3.13}$$

where $\vec{p}_i^{\,*}$ are the momenta of the final state particles in the CMS frame and $\hat{n}$ is the unit vector that maximizes T [41, 42]. The plane perpendicular to the thrust axis $\hat{n}$ splits the event into two hemispheres, as illustrated in fig. 3.3. The thrust angle θ_{thrust} is defined as the angle between the thrust axis $\hat{n}$ and the beam axis. The hemisphere containing the $\tau^- \to \pi^+\pi^-\pi^-\nu_\tau$ candidate is referred to as the signal side, while the opposite hemisphere is the tag side. The $\tau^+\tau^-$ pairs dominantly decay into 2, 4, or 6 charged tracks. The $\tau^- \to \pi^+\pi^-\pi^-\nu_\tau$ decay has a branching fraction of about 9 % [10]. In order to separate our signal decay from other possible τ^- decays, we use the 3×1 prong topology, i.e., require exactly three good charged tracks on the signal side and one good charged track on the tag side.

A charged track is considered good if it fulfills two requirements. First, the track must originate from within $\mathrm{d}r < 1$ cm of the IP in the transverse plane. Second, the distance from the IP along the longitudinal axis must satisfy $|\mathrm{d}z| < 3$ cm. These requirements reject particles originating outside of the interaction region, while retaining most charged particles produced at the IP.

In addition to the ν_τ and charged tracks, other neutral particles can be produced. We reconstruct π^0 candidates from pairs of photon candidates. Photons used to reconstruct π^0 candidates must satisfy the following requirements:

- a timing requirement of $|\Delta t| < 200$ ns

- the ECL polar-angle acceptance of $-0.866 < \cos\theta < 0.9563$
- the ECL cluster must register more than 1.5 hits
- the distance to the nearest charged track must exceed 40 cm, or the photon energy must exceed 400 MeV
- the two-photon invariant mass must satisfy $115 \leq m_{\gamma\gamma} < 152\,\mathrm{MeV}/c^2$.

Photon candidates not associated with a π^0 that also satisfy the timing, angular acceptance, and cluster quality requirements are collected into two lists according to their energy: a good photon list containing candidates with $E_\gamma > 200\,\mathrm{MeV}$, and a loose photon list with $E_\gamma > 100\,\mathrm{MeV}$. These lists are further refined using MVA-based background suppression in the fine selection, as described in section 3.4.

3.3 Preselection

The preselection reduces the data volume while retaining a high fraction of signal events. It proceeds in two steps. First, the tau-thrust skim pre-filters events consistent with $\tau^+\tau^-$-pair decays by requiring 1 to 7 charged tracks, the thrust to exceed 0.8, and the visible energy, i.e., the sum of the energies of all detected particles in the CMS frame, to be below 10.4 GeV. Events must additionally satisfy at least one of the ECL-based trigger bits `lml2`, `lml6`–`lml10`, or `hie`. The `lml` bits correspond to low-energy multi-cluster conditions, where the index distinguishes different combinations of cluster variables [37]. The `hie` bit requires the total ECL energy sum to exceed 1 GeV in the absence of an ECL Bhabha veto.

Second, additional kinematic requirements are imposed on the visible energy, thrust, thrust angle, three-pion invariant mass, squared missing mass, and neutral-particle multiplicities in each hemisphere. These cuts exploit the characteristic topology of $\tau^+\tau^-$-pair events to suppress non-τ^- backgrounds. The missing four-momentum is defined as

$$p_{\text{miss}} = p_{e^+e^-} - \sum_i p_i, \tag{3.14}$$

where $p_{e^+e^-}$ is the initial e^+e^- four-momentum in the laboratory frame and the sum runs over all reconstructed final-state particles. It corresponds primarily to the undetected neutrino. The squared missing mass $m^2_{\text{miss}} = p^2_{\text{miss}}$ and the polar angle θ_{miss} of the missing momentum vector in the laboratory frame are used as discriminating variables. The complete set of requirements is listed in table 3.1.

Table 3.1: Kinematic requirements applied during preselection.

Variable	Requirement
Visible energy (CMS)	$3.5 \leq E^*_{\mathrm{vis}} < 10.5\,\mathrm{GeV}$
Thrust	$0.8 \leq T < 0.99$
Three-pion invariant mass	$m_{3\pi} < 2.0\,\mathrm{GeV}/c^2$
Thrust angle (I)	$-0.7 \leq \cos\theta_{\mathrm{thrust}} < 0.9$
Thrust angle (II)	$\cos\theta_{\mathrm{thrust}} > 0.9\,\theta_{\mathrm{miss}} - 1.575$
	or
	$\cos\theta_{\mathrm{thrust}} < -1.4\,\theta_{\mathrm{miss}} + 2.45$
Missing mass squared (I)	$-3 \leq m^2_{\mathrm{miss}} < 45\,\mathrm{GeV}^2/c^4$
Missing mass squared (II)	$m^2_{\mathrm{miss}} < \frac{-35\,\mathrm{GeV}^2/c^4}{\pi-1.1}\,(\theta_{\mathrm{miss}} - 1.1) + 45\,\mathrm{GeV}^2/c^4$
Photon multiplicity (1-prong)	$N_\gamma^{\text{1-prong}} < 5$
Photon multiplicity (3-prong)	$N_\gamma^{\text{3-prong}} < 5$
π^0 multiplicity (1-prong)	$N_{\pi^0}^{\text{1-prong}} < 2$
π^0 multiplicity (3-prong)	$N_{\pi^0}^{\text{3-prong}} < 2$

3.4 Fine Selection

As a final step of our selection process, we perform the fine selection in three steps. In the first step, we use multivariate analysis (MVA) techniques to further separate background from signal events. In the second step, we correct for discrepancies between the Belle II detector simulation and the real detector. As these corrections are available only in certain detector regions, we restrict the analysis to those regions. In the last step, we restrict the kinematics to the physically allowed phase space.

Separation of Background and Signal Events

A large fraction of signal events have photon candidates reconstructed on the signal side that do not originate from physical decay products. The photon candidates can stem from beam backgrounds or fake photons. The former correspond to photons originating from beam-related activity rather than from the decay itself. The latter correspond to ECL clusters that do not originate from a real photon, but from hadronic split-off. In a hadronic split-off the shower of a charged hadron deposits energy away from its primary cluster. As this cluster does not correspond to any track, it is misidentified

Table 3.2: Input variables used for the BDT.

Kinematic Variables			
Thrust T			
θ^*_{miss}	$\lvert\vec{p}^{\,*}_{\text{miss}}\rvert$	E^*_{vis}	
E^*_{3prong}	$p^*_{t,\text{3prong}}$	m_{miss}	
$N^{\text{3prong}}_{\pi^0}$	$N^{\text{1prong}}_{\pi^0}$		
$\mathrm{d}r^{\text{3prong}}_1$	$\mathrm{d}r^{\text{3prong}}_2$	$\mathrm{d}r^{\text{3prong}}_3$	
$\chi^2_{\text{vtx,3prong}}$	$\Delta_{\text{vtx,3prong}}$		
γ rejection with MVA background suppression variables			
$N^{\text{3prong}}_{\gamma,\text{MVA,good}}$	$N^{\text{1prong}}_{\gamma,\text{MVA,good}}$	$E^{\text{3prong}}_{\gamma,\text{MVA,good}}$	$E^{\text{1prong}}_{\gamma,\text{MVA,good}}$
$N^{\text{3prong}}_{\gamma,\text{MVA,loose}}$	$N^{\text{1prong}}_{\gamma,\text{MVA,loose}}$	$E^{\text{3prong}}_{\gamma,\text{MVA,loose}}$	$E^{\text{1prong}}_{\gamma,\text{MVA,loose}}$

as a photon. These artificial photon candidates are suppressed using two MVA-based discriminants provided by the Belle II software framework [43], `beamBackgroundSuppression` and `fakePhotonSuppression`. Photon candidates with a score below 0.5 for either discriminant are removed from the photon lists.

To suppress the dominant $\tau^- \to \pi^+\pi^-\pi^-\pi^0\nu_\tau$ background, a boosted decision tree (BDT) was trained. The BDT uses the MVA-filtered photon lists as well as additional kinematic variables listed in table 3.2 as input features. This BDT and its input variables follow the implementation introduced in ref. [44]. The BDT assigns each event a score between zero and one. Only events with a score above $T_{\text{BDT}} = 0.633$ are retained, which corresponds to a sample purity of 90 % as estimated using MC15rd simulated data.

Finally, to reduce the number of τ^--decays to kaons in the final state, we apply a cut on the neural-network-based PID variable `kaonIDNN` [45]. The variables `kaonIDNN` and `pionIDNN` correspond to the probabilities, assigned by a neural network, that a given track is a kaon or a pion, respectively. Both variables sum to one. We reject events where `kaonIDNN` > 0.6 for any of the signal-side tracks.

Monte Carlo Corrections

We correct for PID discrepancies between the Belle II detector simulation and the real detector. These corrections were developed in ref. [46]. We assign a weight to every charged track on the signal side. True pion tracks are adjusted based on the efficiency of the `kaonIDNN` < 0.6 selection for pions in real data, $\epsilon_\pi^{\text{data}}$, and in Monte Carlo simulation, ϵ_π^{MC}. This efficiency corresponds to the fraction of true pion tracks that pass the `kaonIDNN` < 0.6 requirement. The pion weight is then given by:

$$w_\pi(p, \cos\theta) = \frac{\epsilon_\pi^{\text{data}}(p, \cos\theta)}{\epsilon_\pi^{\text{MC}}(p, \cos\theta)}. \tag{3.15}$$

True kaon tracks that pass this selection, and are thus misidentified as pions, are given a weight equal to the ratio of the kaon fake rate F_K in real data and Monte Carlo simulation. F_K corresponds to the probability that a kaon passes the `kaonIDNN` < 0.6 requirement. The weight is therefore:

$$w_K(p, \cos\theta) = \frac{F_K^{\text{data}}(p, \cos\theta)}{F_K^{\text{MC}}(p, \cos\theta)}. \tag{3.16}$$

In the end, every event is weighted with the product of the three signal-side track weights:

$$w_{\text{event}} = w_1 w_2 w_3. \tag{3.17}$$

These PID corrections are available only within the momentum range $0.15 < p < 5.0\,\text{GeV}/c$. We restrict our sample to contain only events within this valid range. Additionally, we exclude the region $(\cos\theta < -0.866 \wedge 3.5 < p < 4.5\,\text{GeV}/c)$.

Cuts on Phase Space

As a final step, we restrict the sample to the kinematically allowed phase space for $\tau^- \to \pi^+\pi^-\pi^-\nu_\tau$. Energy-momentum conservation forbids the region outside these boundaries, so any event in this region must be misreconstructed and is removed. The two-pion invariant masses m_{12}, m_{13}, and m_{23} are kinematically constrained. As a lower bound, we require m_{12} and m_{23} to be at least $2m_\pi$. We additionally require $m_{\pi\pi}^2 \leq (m_{3\pi} - m_\pi)^2$ as an upper bound on m_{12}^2 and m_{23}^2. For the limits on m_{13} we follow the parametrization of ref. [10]. The maximum for m_{13}^2 is

$$m_{13(\text{max})}^2 = (E_2 + E_3)^2 - \left(\sqrt{E_2^2 - m_2^2} - \sqrt{E_3^2 - m_3^2}\right)^2, \tag{3.18}$$

and its minimum is

$$m_{13(\text{min})}^2 = (E_2 + E_3)^2 - \left(\sqrt{E_2^2 - m_2^2} + \sqrt{E_3^2 - m_3^2}\right)^2. \tag{3.19}$$

The energies of particles 2 and 3 in the m_{12} rest frame are given by:

$$E_2 = \frac{m_{12}^2 - m_1^2 + m_2^2}{2m_{12}}, \quad E_3 = \frac{m_{3\pi}^2 - m_{12}^2 - m_3^2}{2m_{12}}. \tag{3.20}$$

Beyond the kinematic boundary, we apply an additional, tighter restriction. Near the phase-space boundaries the event density vanishes, leaving these regions too sparsely populated for the background modelling described in section 4.9 to function reliably.

Table 3.3: Expected event yields broken down into signal and background contributions, estimated from the MC15rd sample weighted to $\mathcal{L} = 361.654\,\mathrm{fb}^{-1}$. Table adapted from ref. [25].

Contribution	Weighted Events	Fraction [%]
Signal $\tau^- \to \pi^+\pi^-\pi^-\nu_\tau$	17 034 420	90.5
$\tau^- \to \pi^+\pi^-\pi^-\pi^0\nu_\tau$	1 109 637	5.9
$e^+e^- \to q\bar{q}$	305 406	1.6
Other τ_{Bkg}	312 782	1.7
Rest	64 573	0.3
Total Background	1 792 399	9.5

We therefore apply a more restrictive cut, removing a small margin inside the boundary. We adopt the cuts developed in ref. [25]:

$$m_{13}^2 \leq m_{13,\max}^2 - 0.09\,\mathrm{GeV}^2/\mathrm{c}^4 \tag{3.21}$$

$$m_{12}^2 \geq (2m_\pi)^2 + 0.005\,\mathrm{GeV}^2/\mathrm{c}^4. \tag{3.22}$$

3.5 Background Composition

After the complete event selection, the final data sample is expected to contain a background contribution of approximately 9.5 %, as estimated from the MC15rd sample. Table 3.3 summarizes the expected event yields for signal and each background contribution. The dominant background is from $\tau^- \to \pi^+\pi^-\pi^-\pi^0\nu_\tau$ decays, which enter the selected sample when the π^0 escapes detection, causing the event to mimic the signal topology. This is followed by continuum $e^+e^- \to q\bar{q}$ production, where q denotes the u, d, s, and c quarks. These quarks hadronize and can produce a final state that satisfies the event selection criteria. The category labeled Other τ_{Bkg} comprises all remaining backgrounds from τ^- decays that pass the event selection. The remaining category, labeled Rest, contains all other types of background. Figure 3.4 shows the signal and background contributions as a function of $m_{3\pi}$, evaluated on the MC15rd sample.

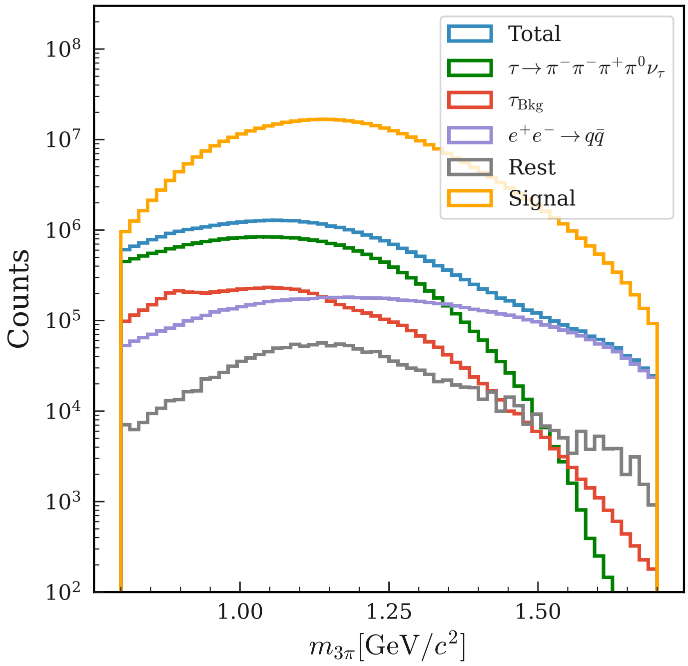

Figure 3.4: Signal and background contributions of the MC15rd sample as a function of $m_{3\pi}$.

4 Partial-Wave Decomposition

In chapter 3 we have established the criteria upon which we select $\tau^- \to \pi^+\pi^-\pi^-\nu_\tau$ decay candidates. Hadronic τ^--decays are known to proceed via intermediate light-meson resonances [47, 48], as established by earlier experiments and confirmed by a partial-wave analysis at the Belle experiment [17]. It is the goal of this analysis to identify and measure the properties of these resonances, such as their quantum numbers, masses, and widths. To this end, we perform a partial-wave analysis (PWA). The PWA formalism we employ consists of two steps. First, the partial-wave decomposition (PWD) decomposes the data sample into contributions from different partial waves. Second, in the resonance-model fit (RMF) resonances are identified in the partial waves and their parameters, such as masses and widths, are measured.

In section 4.1 we introduce the isobar model, which is used to model the decay. Section 4.2 explains the barrier factors used throughout the thesis. The following sections describe the decay rate in section 4.3, the symmetrization of the decay amplitudes in section 4.4, their normalization in section 4.5, and the observables extracted from the fit in section 4.6. The dynamic amplitudes used to parametrize resonances are discussed in section 4.7. As discussed in chapter 3, we expect our sample to contain about 9.5 % background events. The modeling of these background contributions, together with the extended maximum-likelihood fit, is discussed in sections 4.8 and 4.9. Section 4.10 discusses the necessity of thresholds in the PWD formalism. The RMF will be discussed in chapter 6.

4.1 Isobar Model

The $\tau^- \to \pi^+\pi^-\pi^-\nu_\tau$ decay proceeds in two stages. First, the τ^- decays weakly into a ν_τ and an off-shell W-boson. Second, the W-boson hadronizes into the 3π final state. This hadronic decay is described in the isobar model [22, 23], where the decay into the 3π final state is modeled via two subsequent decays (see fig. 4.1). First, the W-boson hadronizes into an intermediate state X^- with quantum numbers J^P, where J corresponds to the spin and P to the parity. The X^- intermediate state then decays into a bachelor π^- and an isobar two-body resonance ξ^0, where the isobar's spin is given by J_ξ. The bachelor π^- and the isobar ξ^0 are produced with relative orbital

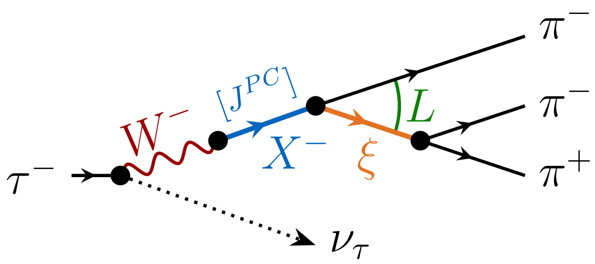

Figure 4.1: Schematic view of the reaction $\tau^- \to \pi^+\pi^-\pi^-\nu_\tau$ in the isobar model, where intermediate state X^- decays into the $\pi^+\pi^-\pi^-$ final state via an isobar ξ^0.

angular momentum L. The isobar then decays into the final two π. An intermediate state with given J^P quantum numbers, together with its decay mode, is summarized as one partial wave. We assign to each possible partial wave a unique partial-wave label

$$a = J^P \xi \pi L \tag{4.1}$$

that identifies it. The goal of the PWD is to decompose the data into contributions from these different partial waves, and to extract the complex partial-wave amplitudes, which model the coupling of each partial wave as a function of $m_{3\pi}$. To obtain this $m_{3\pi}$ dependence, we bin the data into 45 narrow $m_{3\pi}$ bins in the range $0.8\,\mathrm{GeV}/c^2 \leq m_{3\pi} \leq 1.7\,\mathrm{GeV}/c^2$. The PWD is performed independently in each $m_{3\pi}$ bin, so that the $m_{3\pi}$ dependence of the complex amplitudes is obtained without assuming any resonance model.

4.2 Centrifugal Barrier Factors

In a two-body decay, each of the two daughter particles carries momentum of magnitude q_i, the two-body breakup-momentum, in the rest frame of the decaying system:

$$q_i(s) = q(s; m_1, m_2) = \sqrt{\frac{(s - (m_1 + m_2)^2)(s - (m_1 - m_2)^2)}{4s}}, \tag{4.2}$$

where i labels the decay channel, i.e., the two daughter particles with masses m_1 and m_2 that the parent particle decays into, and s corresponds to the squared invariant mass of the decaying system. The strong interaction has a finite range of about 1 fm [10]. Via the uncertainty relation, this range corresponds to a characteristic momentum scale of $q_R \approx 0.2\,\mathrm{GeV}/c$, which sets the scale of the strong interaction. When a decaying particle produces two daughter particles with relative orbital angular momentum L, a centrifugal barrier suppresses the decay whenever the breakup momentum q_i is small compared to q_R. The centrifugal barrier factors model this behavior. We use the parametrization from von Hippel and Quigg [49], which is based on the Blatt-Weisskopf barrier factors [50].

The barrier factor can be separated into two contributions,

$$b^L(q_i^2) = \sqrt{\frac{T_L(q_i^2)}{F_L(q_i^2)}}. \tag{4.3}$$

We refer to the numerator $\sqrt{T_L(q_i^2)}$ as the threshold factor, where T_L is a monomial proportional to q_i^{2L}. The threshold factor suppresses the production of daughter particles with higher orbital angular momenta L near the two-body mass threshold. We refer to $\sqrt{F_L(q_i^2)}$ as the finite-size correction, where F_L is a polynomial of order L in q_i^2 with a non-vanishing constant term. Without it, the barrier factor would grow indefinitely with increasing s, which is unphysical. This factor accounts for the finite range of the interaction, which is related to the size of the decaying meson. Once the two daughter particles are far outside the interaction range, the barrier factor saturates to a constant, i.e., $\lim_{s\to\infty} b^L(q_i^2(s)) \to \text{const}$. The explicit expressions for T_L and F_L are listed in ref. [51][1].

4.3 Decay Rate

The $\tau^- \to \pi^+\pi^-\pi^-\nu_\tau$ decay rate Γ differential in the four-body $\pi^+\pi^-\pi^-$ phase-space Φ is given by

$$\frac{\mathrm{d}\Gamma}{\mathrm{d}\Phi} = |\mathcal{M}|^2, \tag{4.4}$$

where $\mathcal{M}$ is the matrix element that encodes the dynamics of the decay. We follow the parametrization for the matrix element $\mathcal{M}$ from ref. [39, 52]. Our semi-leptonic decay is governed by two different currents: the leptonic current ℓ_μ and the hadronic current J^μ. The former encodes the dynamics of the weak decay of the τ^-, while the latter encodes the dynamics of the hadronic system. The matrix element is then proportional to the two currents:

$$\mathcal{M} \propto \ell_\mu J^\mu. \tag{4.5}$$

The leptonic current coupling to the W-boson is a Vector−Axial (V−A) interaction of the form

$$\ell^\mu = \bar{u}_\nu \gamma^\mu (1-\gamma^5) u_\tau, \tag{4.6}$$

where $\bar{u}_\nu$ and u_τ correspond to the ν_τ and τ^- spinors, respectively.

As the hadron current J^μ encodes the dynamics of the strong interaction, it cannot be calculated ab initio. We model the hadron current as a coherent sum

$$J^\mu = \sum_a c_a j_a^\mu \tag{4.7}$$

[1] In ref. [51] the ratio $b^L = \sqrt{\frac{T_L}{F_L}}$ are shown.

over individual hadronic currents j_a^μ times complex partial wave amplitudes c_a for each partial wave a. The couplings encode the relative strengths and phases of the individual partial waves a. These are not known and have to be measured from data. The j_a^μ encode the kinematic and angular structure, and can be calculated within the isobar model. They are parametrized as

$$j_a^\mu = \frac{\mathcal{D}_\xi(m_{\pi^+\pi^-}^2)\mathcal{Z}_a^\mu(\tau)}{\sqrt{F_L\left(q^2(m_{3\pi}^2; m_{\pi^+\pi^-}, m_{\pi^-})\right) F_{J_\xi}\left(q^2(m_{\pi^+\pi^-}^2; m_\pi, m_\pi)\right)}}. \tag{4.8}$$

The dynamic amplitude $\mathcal{D}_\xi$, as a function of the invariant mass of the $\pi^+\pi^-$ system[2], represents the propagation of the isobar. We model most of the isobars with the relativistic Breit–Wigner amplitude (see eq. (4.29)). Some waves require more elaborate parametrizations, all of which will be discussed in section 4.7. $\mathcal{Z}_a^\mu$ encodes the spin dependence of both X^- and ξ^0. We employ the covariant tensor formalism, in which $\mathcal{Z}_a^\mu$ already contains the threshold factor $\sqrt{T_L}$ of eq. (4.3), which suppresses amplitudes of high orbital angular momentum L near the two-body mass threshold, so that only the finite-size correction factors F_L and F_{J_ξ} are needed to fully account for the centrifugal barrier.

In order to calculate the decay rate, the absolute square of the matrix element $\mathcal{M}$ is necessary. It is convenient to first consider $|\mathcal{M}^{\lambda_\tau}|^2$, the squared matrix element for a single τ^- helicity λ_τ[3]. It is given by:

$$\begin{aligned} |\mathcal{M}^{\lambda_\tau}|^2 &= \sum_{a,b} c_a c_b^* \left(j_a^\mu \ell_\mu^{\lambda_\tau}\right)\left(j_b^\nu \ell_\nu^{\lambda_\tau}\right)^* \\ &= \sum_{a,b} c_a c_b^* \left(\ell_\mu^{\lambda_\tau} \ell_\nu^{\lambda_\tau *}\right)\left(j_a^\mu j_b^{\nu *}\right) \\ &= \sum_{a,b} c_a c_b^* L_{\mu\nu}^{\lambda_\tau} H_{ab}^{\mu\nu}, \end{aligned} \tag{4.9}$$

where we introduce the lepton tensor $L_{\mu\nu}^{\lambda_\tau} = \ell_\mu^{\lambda_\tau} \ell_\nu^{\lambda_\tau *}$ and the hadron tensor $H_{ab}^{\mu\nu} = j_a^\mu j_b^{\nu *}$. The τ^--leptons do not have a preferred helicity, since the Belle II beam is unpolarized [53]. Therefore, the lepton tensor is averaged over the τ^- helicities:

$$\tilde{L}_{\mu\nu} = \frac{1}{2}\sum_{\lambda_\tau} L_{\mu\nu}^{\lambda_\tau}. \tag{4.10}$$

The angle α is not experimentally accessible (see section 3.1.2), due to the undetected ν_τ. Therefore, we further marginalize the lepton tensor $\tilde{L}_{\mu\nu}$ over the angle α:

$$\overline{L}_{\mu\nu} = \frac{1}{2\pi}\int \mathrm{d}\alpha\, \tilde{L}_{\mu\nu}. \tag{4.11}$$

[2] We impose a certain ordering of the two π^- (see section 3.1). In section 4.4 we symmetrize over both possible configurations.

[3] Here, we assume a fixed neutrino helicity.

The eigenvalue decomposition of the combined helicity-averaged and α-marginalized lepton tensor replaces the tensor contraction with a sum of at most four scalar products, significantly reducing the computational cost. The v^i_μ are constructed from the eigenvalues λ_i and eigenvectors $\tilde{v}^i_\mu$ of $\bar{L}_{\mu\nu}$ as:

$$v^i_\mu = \sqrt{\lambda_i}\,\tilde{v}^i_\mu. \tag{4.12}$$

Therefore, $\bar{L}_{\mu\nu}$ is given by:

$$\overline{L}_{\mu\nu} = \sum_{i=1}^{4} v^i_\mu v^{i*}_\nu. \tag{4.13}$$

This leads to the final expression for the helicity-averaged and α-marginalized squared matrix element[4] $\overline{|\mathcal{M}|^2}$:

$$\begin{aligned}
\overline{|\mathcal{M}|^2} &= \sum_{a,b} c_a c_b^* \,\overline{L}_{\mu\nu} H^{\mu\nu}_{ab} \\
&= \sum_{a,b} c_a c_b^* \sum_{i=1}^{4} v^i_\mu v^{i*}_\nu j^\mu_a j^{\nu*}_b \\
&= \sum_{a,b} \sum_{i=1}^{4} c_a c_b^* \,\psi'^i_a \psi'^{i*}_b \\
&= \sum_{i=1}^{4} \left| \sum_a c_a \psi'^i_a \right|^2
\end{aligned} \tag{4.14}$$

with the decay amplitudes defined as:

$$\psi'^i_a = v^i_\mu j^\mu_a. \tag{4.15}$$

4.4 Symmetrization of Decay Amplitudes

As discussed in section 3.1, our final state $\pi_1^+\pi_2^-\pi_3^-\nu_\tau$ contains two indistinguishable π^- mesons. Since they are identical bosons, the decay amplitudes ψ'^i_a, defined in eq. (4.15), must be symmetric under the exchange of the two π^- by the requirement of Bose statistics. To impose Bose symmetry on the matrix element, the decay amplitudes are written as a coherent sum of the two possible pion assignments:

$$\tilde{\psi}^i_a = \psi'^i_{a,(\pi_1,\pi_2,\pi_3)} + \psi'^i_{a,(\pi_1,\pi_3,\pi_2)}. \tag{4.16}$$

[4] All constant proportionality factors are absorbed into the complex partial wave amplitudes c_a: the constant factors omitted in eq. (4.5), and the factors from the helicity averaging and the α-marginalization.

4.5 Normalization of Decay Amplitudes

The Bose-symmetrized decay amplitudes $\tilde{\psi}_a^i$ are normalized to fix their absolute scale. We define the normalized decay amplitude ψ_a^i as:

$$\psi_a^i(\tau) = \frac{\tilde{\psi}_a^i(\tau)}{\sqrt{\mathcal{R}_a(m_{3\pi})}}, \tag{4.17}$$

where $\mathcal{R}_a(m_{3\pi})$ is the normalization integral, given by:

$$\mathcal{R}_a(m_{3\pi}) = \sum_{i=1}^{4} \int_{\text{bin}} \mathrm{d}\Phi(\tau)\, |\tilde{\psi}_a^i(\tau)|^2, \tag{4.18}$$

where the integral runs over the four-body phase space within one $m_{3\pi}$ bin. The integral is approximated using Monte-Carlo integration[5] over a simulated sample that is uniformly distributed in phase space [54]. The normalization integral $\mathcal{R}_a$ can be interpreted as the phase-space volume filled by partial wave a, as it incorporates the $\pi^+\pi^-\pi^-$ phase space accessible at $m_{3\pi}$. The normalized decay amplitudes satisfy:

$$\sum_{i=1}^{4} \int_{\text{bin}} \mathrm{d}\Phi(\tau)\, |\psi_a^i(\tau)|^2 = 1. \tag{4.19}$$

4.6 Observables

In order to relate the formalism introduced in the past sections to real measurable quantities, we first define the model intensity $\mathcal{I}(\tau)$. It describes the distribution of events predicted by our model, differential in the phase space $\Phi(\tau)$. This quantity is proportional to the decay rate defined in eq. (4.4). We absorb the proportionality factor into the complex partial wave amplitude c_a. Therefore, the model intensity is given by:

$$\mathcal{I}(\tau) = \frac{\mathrm{d}\hat{N}(\tau)}{\mathrm{d}\Phi(\tau)} = \sum_{i=1}^{4} \sum_{a,b} c_a c_b^* \psi_a^i(\tau) \psi_b^{i*}(\tau). \tag{4.20}$$

From the model intensity the number of events $\hat{N}$ predicted by our model can be calculated as:

$$\begin{aligned}
\hat{N}(m_{3\pi}) &= \int \mathrm{d}\Phi(\tau)\, \mathcal{I}(\tau) \\
&= \int \mathrm{d}\Phi(\tau) \sum_{i=1}^{4} \sum_{a,b} c_a c_b^* \psi_a^i(\tau) \psi_b^{i*}(\tau) \\
&= \sum_{a,b} c_a I_{ab} c_b^*,
\end{aligned} \tag{4.21}$$

[5]The integral is evaluated as $\mathcal{R}'_a(m_{3\pi}) = \mathcal{R}_a(m_{3\pi})/V_4(m_{3\pi})$, where V_4 is the four-body phase-space volume. Dividing out the four-body phase-space volume $V_4(m_{3\pi})$ at a given $m_{3\pi}$ bin does not change the PWD fit results.

where we introduce the phase-space integral matrix:

$$I_{ab}(m_{3\pi}) = \sum_{i=1}^{4} \int_{\text{bin}} \mathrm{d}\Phi(\tau)\, \psi_a^i(\tau)\psi_b^{i*}(\tau). \tag{4.22}$$

I_{ab} is evaluated using Monte Carlo integration over a simulated signal sample at generator level, i.e., before detector simulation [25]. Due to the normalization of the decay amplitudes in eq. (4.19), the diagonal elements I_{aa} of the phase-space integral matrix are all equal to one. We can further introduce the spin-density matrix

$$\rho_{ab} = c_a c_b^*, \tag{4.23}$$

which simplifies eq. (4.21) to:

$$\hat{N}(m_{3\pi}) = \sum_{a,b} I_{ab}\rho_{ab}. \tag{4.24}$$

When limiting the sum in eq. (4.24) to a single partial wave a and summing over all $m_{3\pi}$ bins, the number of events in that wave is obtained:

$$\hat{N}_a = \sum_{m_{3\pi}} I_{aa}\rho_{aa} = \sum_{m_{3\pi}} \rho_{aa}. \tag{4.25}$$

We refer to $\hat{N}_a$ as the yield of partial wave a.

As our detector is not perfect, the probability that a decay event at phase-space point τ is reconstructed and passes all selection criteria is encoded in the acceptance $\eta(\tau)$. The distribution of events that we actually measure in the detector must therefore be weighted with this acceptance[6]:

$$\frac{\mathrm{d}\hat{\hat{N}}(\tau)}{\mathrm{d}\Phi(\tau)} = \eta(\tau)\mathcal{I}(\tau). \tag{4.26}$$

The model prediction for the number of measured events is consequently:

$$\begin{aligned}\hat{\hat{N}}(m_{3\pi}) &= \int \mathrm{d}\Phi(\tau)\, \eta(\tau)\mathcal{I}(\tau) \\ &= \int \mathrm{d}\Phi(\tau)\, \eta(\tau) \sum_{i=1}^{4} \sum_{a,b} c_a c_b^* \psi_a^i(\tau)\psi_b^{i*}(\tau) \\ &= \sum_{a,b} \rho_{ab}\bar{I}_{ab},\end{aligned} \tag{4.27}$$

where we introduce the accepted integral matrix:

$$\bar{I}_{ab}(m_{3\pi}) = \sum_{i=1}^{4} \int_{\text{bin}} \mathrm{d}\Phi(\tau)\, \eta(\tau)\, \psi_a^i(\tau)\psi_b^{i*}(\tau). \tag{4.28}$$

The accepted integral matrix $\bar{I}_{ab}$ is the acceptance-weighted analogue of I_{ab}, with $\eta(\tau)$ folded into the phase-space integral. $\bar{I}_{ab}$ is evaluated analogously to I_{ab}, using a signal Monte Carlo sample after detector simulation and event selection.

[6] In this formalism the detector resolution is neglected. A dedicated study in chapter 8 indicates that this approximation has a negligible impact on the results.

4.7 Dynamic Amplitudes

As discussed in section 4.3, the dynamic amplitude $\mathcal{D}_\xi$ represents the propagation of the isobar. Different isobars require different parametrizations. In the following we discuss four different parametrizations, each modelling different kinds of resonances. A more general approach to parametrizing resonances will be discussed in chapter 10.

Relativistic Breit–Wigner

The most common parametrization for resonance lineshapes is the relativistic Breit–Wigner amplitude [10]. It is an approximation for narrow, isolated resonances, and is given by:

$$\mathcal{D}_{\mathrm{BW}}(s; m_0, \Gamma_0) = \frac{m_0 \Gamma_0}{m_0^2 - s - i m_0 \Gamma(s)}, \tag{4.29}$$

with the Breit–Wigner mass m_0 and width Γ_0 parameters of the resonance. In the denominator, the energy-dependent width $\Gamma(s)$ models the decay rate of the resonance as a function of s. For very narrow states, like the $\omega(782)$, the mass dependence can be dropped by using $\Gamma(s) = \Gamma_0$. The energy-dependent width is given by:

$$\Gamma(s; m_0, \Gamma_0) = \Gamma_0 \frac{q(s)}{q(m_0^2)} \frac{m_0}{\sqrt{s}} \frac{(b^L(s))^2}{(b^L(m_0^2))^2}. \tag{4.30}$$

The two-body breakup momenta q^2 are defined in eq. (4.2) and the barrier factors b^L in eq. (4.3). This form of the energy-dependent width assumes a single, two-body decay channel with orbital angular momentum L. Resonances with significant coupling to additional channels require more elaborate parametrizations.

Gounaris–Sakurai

The $\rho(770)$ is one of the best-studied light-meson resonances, measured precisely in many experiments. It is a broad state, with a width of about $150\,\mathrm{MeV}/c^2$ at a mass of $770\,\mathrm{MeV}/c^2$ [10]. Its width and the wealth of precise data motivated a dedicated parametrization of the $\pi\pi$ P-wave, the Gounaris–Sakurai amplitude [55]. We use the parametrization defined in ref. [56]. It differs from the relativistic Breit–Wigner amplitude only by the addition of a single real term $f_{GS}(s)$ in the denominator:

$$\mathcal{D}_{GS}(s; m_0, \Gamma_0) = \frac{m_0 \Gamma_0}{m_0^2 - s + f_{GS}(s) - i m_0 \Gamma(s)}, \tag{4.31}$$

where $f_{GS}(s)$ corresponds to the real part of the self-energy, given by:

$$f_{GS}(s; m_0, \Gamma_0) = \frac{\Gamma_0 m_0^2}{q^3(m_0^2)} \left[q^2(s) \left(h(s) - h(m_0^2) \right) + q^2(m_0^2) h'(m_0^2)(m_0^2 - s) \right], \tag{4.32}$$

with the two-body breakup momentum $q(s)$ (see eq. (4.2)) and

$$h(s) = \frac{2}{\pi}\frac{q(s)}{\sqrt{s}}\ln\left(\frac{\sqrt{s}+2q(s)}{2m_\pi}\right), \tag{4.33}$$

where m_π is the pion mass. The h' in eq. (4.32) is the derivative of h.

Flatté Amplitude

Another isobar resonance that cannot be accurately modeled by the Breit–Wigner amplitude is the $f_0(980)$. This resonance has a mass close to the $K\bar{K}$ threshold, making a Breit–Wigner parametrization insufficient. More details on the reasons that the Breit–Wigner amplitude fails to describe this system are discussed in chapter 10. We therefore use the Flatté parametrization [57], with the parameters extracted by the BES collaboration in ref. [58]. The amplitude is given by:

$$\mathcal{D}_{\text{Flatté}}(s;\gamma_1,\gamma_{21}) = \frac{1}{m_0^2 - s - i\gamma_1\left(2\sqrt{\frac{q_{\pi\pi}^2(s)}{s}} + 2\gamma_{21}\sqrt{\frac{q_{KK}^2(s)}{s}}\right)}. \tag{4.34}$$

The $q_{\pi\pi}(s)$ and $q_{KK}(s)$ factors correspond to the breakup momenta defined in eq. (4.2) for the $\pi\pi$ and $K\bar{K}$ systems, respectively. γ_1 and γ_{21} encode the constant couplings to the $\pi\pi$ and $K\bar{K}$ channels of the $f_0(980)$ resonance.

Au-Morgan-Pennington-Kachaev (AMPK) Amplitude

The $\pi\pi$ S-wave cannot be described well by any of the parametrizations introduced so far. Due to its broad structure, a dedicated parametrization is necessary for this isobar. We use the Au–Morgan–Pennington–Kachaev (AMPK) amplitude [59, 60]. The AMPK amplitude is constructed from an M-matrix formalism, similar to the K-matrix formalism introduced in chapter 10. The M-matrix accounts for $\pi\pi$ scattering through multiple coupled channels, such as $\pi\pi \to \pi\pi$ and $\pi\pi \to K\bar{K}$. The scattering amplitude is encoded in the transition (T-)matrix, whose element T_{ij} describes the transition from channel j to channel i and which is obtained from the M-matrix. The $\pi\pi$ S-wave isobar amplitude is then given by the $\pi\pi \to \pi\pi$ element T_{11}:

$$\mathcal{D}_{\text{AMPK}}(s) = T_{11}(s). \tag{4.35}$$

In our model the $f_0(980)$ is already included as a separate isobar with its own Flatté parametrization (see eq. (4.34)). To avoid describing this resonance twice, we use the modification of Kachaev, which removes the $f_0(980)$ pole and the associated $\pi\pi \to K\bar{K}$ channel coupling from the amplitude. The AMPK amplitude thus describes only the broad $f_0(500)$ component of the $\pi\pi$ S-wave.

4.8 Partial-Wave Decomposition Fit

As discussed in the previous sections, nearly all quantities are predetermined and can be calculated. Only the partial wave amplitudes c_a are unknowns in our formalism. To obtain the c_a and their $m_{3\pi}$ dependence, we perform independent extended maximum-likelihood fits[7] in each $m_{3\pi}$ bin, where the complex partial wave amplitudes are free parameters. The likelihood is given by:

$$\mathcal{L}_{\mathrm{PWD}} = \frac{\hat{\hat{N}}^{\bar{N}}\, e^{-\hat{\hat{N}}}}{\bar{N}!} \prod_{e=1}^{\bar{N}} P(\tau_e, m_{3\pi}). \tag{4.36}$$

The fraction corresponds to the Poisson probability to measure $\bar{N}$ events given we expect to measure $\hat{\hat{N}}$ events. The product runs over all measured events e, multiplying the probabilities P of an event in a given $m_{3\pi}$ bin. The probability of a single event reads:

$$P(\tau_e, m_{3\pi}) = \frac{\eta(\tau_e)\,\Phi(\tau_e)\,\mathcal{I}(\tau_e)}{\hat{\hat{N}}(m_{3\pi})}. \tag{4.37}$$

Taking the negative logarithm of the likelihood converts the product into a sum. The negative log-likelihood (NLL) function then reads:

$$-\ln \mathcal{L}_{\mathrm{PWD}} = -\sum_{e=1}^{\bar{N}} \ln \left(\sum_{i=1}^{4} \sum_{a,b} c_a c_b^*\, \psi_a^i(\tau_e) \psi_b^{i*}(\tau_e) \right) + \hat{\hat{N}} + \text{const}. \tag{4.38}$$

As constant terms only shift the overall NLL value without changing its minimum, they can be dropped in the fitting process. Note that the NLL only contains complex partial wave amplitude pairs $c_a c_b^*$, rendering the model invariant under a global phase rotation $c_a \to e^{i\varphi} c_a$. To resolve this ambiguity, we fix the couplings of one wave, the reference wave, to be real and positive.

As mentioned in chapter 3, we expect about 9.5 % background in the final real data sample. So far, however, background contributions have not been accounted for in the PWD formalism. To account for background events, we extend the probability of one event by the product of the true reconstructed background yield $\hat{\hat{N}}_B$ and the background probability density function P_B:

$$\begin{aligned} P(\tau_e, m_{3\pi}) &= \frac{\eta(\tau_e)\,\Phi(\tau_e)\mathcal{I}(\tau_e) + \hat{\hat{N}}_B\, P_B(\tau_e)}{\hat{\hat{N}}(m_{3\pi}) + \hat{\hat{N}}_B(m_{3\pi})} \\ &= \frac{\eta(\tau_e)\,\Phi(\tau_e)\left[\mathcal{I}(\tau_e) + \hat{\hat{N}}_B\, B(\tau_e)\right]}{\hat{\hat{N}}(m_{3\pi}) + \hat{\hat{N}}_B(m_{3\pi})}, \end{aligned} \tag{4.39}$$

where $\hat{\hat{N}}_B$ corresponds to the background yield, i.e., the number of events modeled as background events. In the second line we introduce the background function

$$B(\tau) = \frac{P_B(\tau)}{\eta(\tau)\,\Phi(\tau)}. \tag{4.40}$$

[7]The model we use to fit and the pseudo data we fit to are described in chapter 7.

With the background function being introduced the acceptance $\eta(\tau)$ and phase space $\Phi(\tau)$ can be factored out of the probability. This is a necessary step, as only then these factors appear as individual summands in the NLL independent of the fit parameters and can be neglected in the NLL. We parametrize the background function using a neural-network approach [25]. To this end, we implement the binary classifier approach of refs. [61, 62]. The binary classifier learns to separate events into two categories: phase-space distributed signal $\tilde{S}$ and background. The implementation of the binary classifier approach is described in section 4.9. The output of the neural network NN corresponds to the probability of an event being a signal event:

$$\mathrm{NN}(\tau) = P(\tilde{S}|\tau) = \frac{P_{\tilde{S}}(\tau)}{P_{\tilde{S}}(\tau) + P_B(\tau)}, \tag{4.41}$$

where $P_{\tilde{S}}$ is the phase-space signal probability density function that is uniform in phase space $P_{\tilde{S}}(\tau) \propto \eta(\tau)\Phi(\tau)$. The background function is then obtained as

$$B(\tau) = \frac{1 - \mathrm{NN}(\tau)}{\mathrm{NN}(\tau) \cdot \mathcal{N}}, \tag{4.42}$$

with the normalization:

$$\mathcal{N} = \int_{\mathrm{bin}} \mathrm{d}\Phi(\tau)\, \eta(\tau)\, \frac{1 - \mathrm{NN}(\tau)}{\mathrm{NN}(\tau)}. \tag{4.43}$$

Finally, the NLL for signal and background events is:

$$-\ln \mathcal{L}_{\mathrm{PWD}} = -\sum_{e=1}^{\bar{N}} \ln\left(\sum_{i=1}^{4}\sum_{a,b} c_a c_b^*\, \psi_a^i(\tau_e)\psi_b^{i*}(\tau_e) + \hat{\bar{N}}_B\, B(\tau_e)\right) + \hat{\bar{N}} + \hat{\bar{N}}_B + \text{const.} \tag{4.44}$$

We minimize the NLL with respect to the complex partial wave amplitudes c_a using the `iminuit` package [63, 64]. The covariance matrix of the fitted parameters is estimated from the Hessian of the NLL at the minimum. For more details on the PWD fit and the background modelling, we refer the reader to ref. [25].

4.9 Background Modelling

During the development of the neural network, several different neural-network architectures were tested [25]. We use the so-called sliding-window approach, which we briefly introduce here. In total, the full $m_{3\pi}$ range is modeled by 11 different neural networks. Each was trained in an $m_{3\pi}$ window of size $0.18\,\mathrm{GeV}/c^2$, corresponding to 9 $m_{3\pi}$ bins (see fig. 4.2). In the PWD fit each neural network is only used for an $m_{3\pi}$ range that is smaller than the $m_{3\pi}$ range it was trained for. At the borders of the $m_{3\pi}$ range, the networks are used in only two $m_{3\pi}$ bins of the PWD fit. In between, one network is used for 4–5 adjacent $m_{3\pi}$ bins.

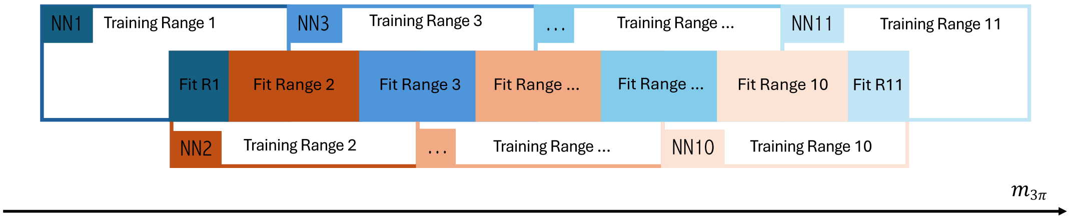

Figure 4.2: Visualization of the $m_{3\pi}$ ranges of the 11 neural networks in the sliding-window approach. The transparent squares, noted as NNx where $x \in \{1, \dots, 11\}$, denote the training range of neural network x. The filled squares correspond to the $m_{3\pi}$ ranges in which neural network x is used in the PWD fit. Taken from ref. [25].

4.10 Thresholding

In input-output studies performed in ref. [25] it was found that, in low $m_{3\pi}$ bins, some partial waves exhibit very similar shapes. The fitter can then no longer distinguish between these partial waves, leading to strongly inflated uncertainties and unphysically high intensities. To resolve these ambiguities, we exclude the affected partial waves from the $m_{3\pi}$ bins in which they cannot be distinguished. As this problem occurs only at low $m_{3\pi}$, the exclusion is applied only in the low-$m_{3\pi}$ region. The method used to determine which partial waves to exclude is described in ref. [25].

5 Automatizing PWD Workflow

The PWD introduced in chapter 4 involves 454 different steps. Many steps require certain other steps to be performed before their own execution, thus a difficult dependency tree, i.e., a structure that encodes the dependencies of the tasks, is built between the steps. Executing all 454 steps by hand is very error-prone, as keeping track of the executed steps and starting a step only after its dependencies have completed is highly complex. To avoid this, an analysis pipeline was built, that automatically resolves the dependencies and executes the tasks in the correct order without manual intervention. In order to realize this analysis pipeline we chose the `b2luigi` package, developed by the Belle II collaboration [65, 66]. In the following, we explain the structure of the analysis pipeline and how it is designed to work efficiently.

`b2luigi` stands for *bringing batch to luigi* and is built on top of the `luigi` Python package [67]. `luigi` is a workflow manager designed to ease the development of long-running batch pipelines: it chains steps together, resolves their dependencies automatically, and executes steps in parallel. `b2luigi` extends `luigi` by automatically submitting steps to computing clusters. Therefore, we can focus on developing the physics of the steps and not worry about the dependencies. In `b2luigi`, each step is implemented as a task, for which one defines both the computation to be performed and its dependencies on other tasks. At runtime, `b2luigi` recursively resolves these dependencies: a task is submitted as soon as all tasks it depends on have completed, and any tasks whose dependencies are satisfied are executed simultaneously. This means parallelism occurs not only within a single stage of the pipeline, but across the entire dependency tree. Cached outputs from previous runs are reused where available.

The workflow of our analysis pipeline is visualized in fig. 5.1. We require `b2luigi` to run a top-level task called `FullPipeline`, whose sole purpose is to build the full dependency tree. Once the dependency tree is built, it is executed from bottom to top. In the following, we go through the different tasks and explain their meaning.

The analysis pipeline requires three different datasets. The first is the data sample to which the PWD model is fit, referred to as *FittedData*. The second dataset, *GenMCData*,

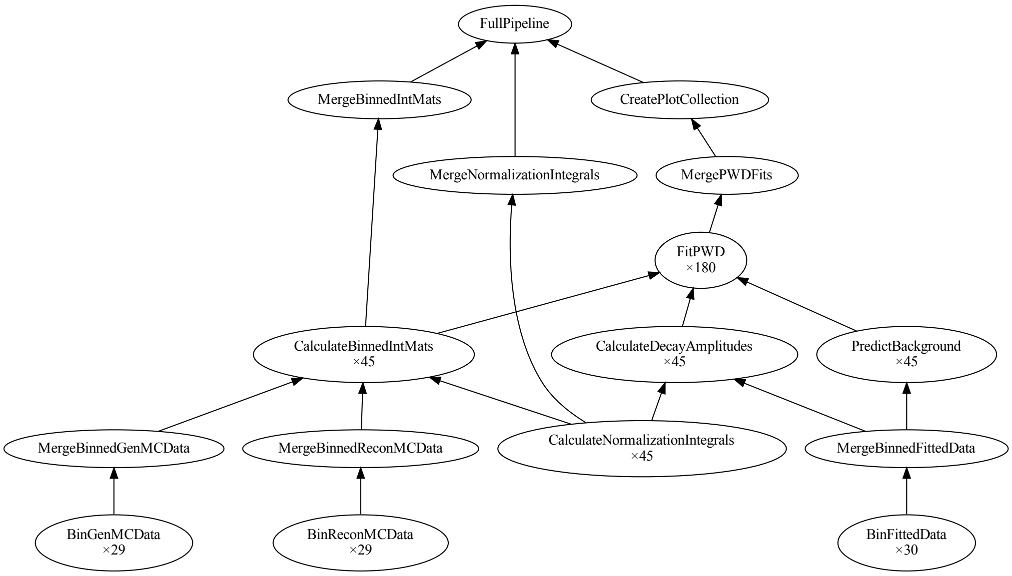

Figure 5.1: Visualization of the analysis pipeline. Tasks at the bottom are executed first. Arrows indicate which tasks must complete before the task at the arrow tip can begin. The multiplicity label $\times N$ on a node indicates how many instances of that task are executed, reflecting that some tasks are run independently for different input data or conditions, such as different $m_{3\pi}$ bins or different data chunks.

is used to calculate the phase-space integral matrix (see eq. (4.22)). The third dataset, *ReconMCData*, is used to calculate the acceptance integral matrix (see eq. (4.28)). The datasets will be discussed in chapter 7. Due to the size of all three datasets, they are stored in separate chunks of equal physical distribution[1]. As a first stage, the tasks `BinGenMCData`, `BinReconMCData`, and `BinFittedData` each load one chunk and bin the data into 45 $m_{3\pi}$ bins, with all chunks processed in parallel. The individual bins are then merged by `MergeBinnedGenMCData`, `MergeBinnedReconMCData`, and `MergeBinnedFittedData`, producing one file per $m_{3\pi}$ bin[2].

Simultaneously, the normalization integrals (see eq. (4.18)) are calculated by `CalculateNormalizationIntegrals`. Since this task is independent for each $m_{3\pi}$ bin, all

[1] *FittedData* is stored in 30 chunks, while *GenMCData* and *ReconMCData* are stored in 29 separate chunks. The different number of chunks results from different data generation processes that were not matched.

[2] The merge tasks could in principle also be parallelized, by splitting each merge task into per-bin sub-tasks, so that all $m_{3\pi}$-bins are merged in parallel. However, each merge task finishes quickly, so the additional scheduling overhead of this splitting would outweigh any time saved.

bins are processed in parallel.

The task `CalculateBinnedIntMats` calculates the phase-space and accepted integral matrices (see eqs. (4.22) and (4.28)). These tasks require the binned and merged *GenMCData* and *ReconMCData* as well as the normalization integrals. As soon as the normalization integral for a given $m_{3\pi}$ bin is available and both merged data samples exist, the integral matrices for that bin are calculated. This task is parallelized across all $m_{3\pi}$ bins.

Once the *FittedData* is binned and merged and the normalization integrals are available, the decay amplitudes (see eq. (4.15)) are calculated by `CalculateDecayAmplitudes`. These can also be computed simultaneously across all $m_{3\pi}$ bins. At the same time, `PredictBackground` evaluates the background function (see eq. (4.40)) in bins of $m_{3\pi}$ using the binned and merged *FittedData*.

Once the decay amplitudes, integral matrices, and background functions for a given $m_{3\pi}$ bin are available, the PWD fit is performed by `FitPWD`. We decided to split up the 100 fit attempts performed per $m_{3\pi}$ bin into several tasks with fewer fit attempts each. This decision was motivated by a key observation: during the fitting process, some $m_{3\pi}$ bins converge quickly while others require considerably more time, meaning the total runtime was dominated by a few slow bins. As the `FitPWD` task needs to load the evaluated background function, the decay amplitudes and the integral matrices, it is not feasible to perform each fit attempt in a single task due to the overhead of loading the data. We found that splitting the 100 fit attempts into four tasks of 25 attempts each was sufficient to remove this bottleneck in practice. We did not further optimize this choice, as no additional overhead was observed beyond this point. Since this splitting is applied independently in each of the 45 $m_{3\pi}$ bins, it results in $4 \times 45 = 180$ `FitPWD` tasks in total, consistent with the multiplicity shown in fig. 5.1. These 180 tasks can be executed in parallel wherever their dependencies are already resolved. How many run simultaneously at any given time is limited by the computing infrastructure, as discussed at the end of this chapter, not by the pipeline itself. This change strongly reduced the bottleneck, and no comparable bottleneck has been observed since. A further benefit is that additional fit attempts can be requested after the analysis pipeline has finished: `b2luigi` schedules only the new tasks while reusing the already completed results.

The fit results are then merged into a single file by `MergePWDFits`. Similarly, `MergeBinnedIntMats` and `MergeNormalizationIntegrals` combine the integral matrices and normalization integrals into single files for use in the subsequent RMF steps. `CreatePlotCollection` then generates an object containing all relevant fit-result information, enabling efficient downstream plotting. Once all of these tasks are complete, `FullPipeline` is marked as done.

This analysis pipeline removes the risk of human error in determining the correct order and timing of task execution. It automatically schedules the tasks and resolves their dependencies without manual intervention. The example shown in fig. 5.1 consists of 454 individual tasks that are executed with a single command that starts the analysis pipeline. As most tasks are computationally expensive but do not require a lot of memory, 30 to 50 tasks can be executed simultaneously on our computing infrastructure, reducing the time for the whole analysis pipeline to finish from two days to about four hours. As several studies required executing the same tasks, `b2luigi`'s caching allowed us to reuse cached results from previous runs, further reducing the computational time required to complete the pipeline.

6 Resonance-Model Fit

As discussed in chapter 4, we perform the PWA in a two-step approach. First, we measure the amplitudes of the partial waves in narrow $m_{3\pi}$ bins using the PWD fit discussed in chapter 4. In this first step we do not impose a model for the $m_{3\pi}$ dependence. The goal of the second step, the resonance-model fit (RMF), is to extract the resonant structure of the partial waves. To this end, the $m_{3\pi}$ dependence of the amplitudes is modeled explicitly. From a χ^2-fit of the model to the partial-wave amplitudes, the resonances are identified and their parameters, such as mass and width, extracted. In general, we fit all PWD partial waves simultaneously, but the formalism allows us to choose a subset of the PWD partial waves on which to perform the RMF. In this analysis, this feature was mainly used for the RMFs discussed in chapter 10. The RMF formalism we implemented follows the formalism introduced in ref. [51].

We first introduce in section 6.1 how the partial-wave amplitudes are modeled in the RMF. Then, in section 6.2, the fit formalism is introduced. We can also extract fit fractions from the RMF, which is described in section 6.3.

6.1 Modelling the Spin-Density Matrix

In the PWD we have factorized the hadron current (see eq. (4.7)) into individual hadronic currents j_a^μ (see eq. (4.8)) for each partial wave a, whose kinematic and angular structure can be constructed from the quantum numbers of the partial wave, and complex-valued partial-wave amplitudes c_a. These complex-valued partial-wave amplitudes summarize the full unknown dynamics of the partial waves. In order to identify the intermediate resonances in the partial waves, we describe these partial-waves amplitudes by an explicit model. Our model $\hat{c}_a$ for the partial-wave amplitudes is given by:

$$\hat{c}_a(m_{3\pi}) = \sqrt{\mathcal{R}_a(m_{3\pi})} \sum_{k\in\mathbb{S}_a} {}^k\mathcal{C}_a \, \mathcal{D}_k(m_{3\pi}; \zeta_k). \tag{6.1}$$

The expression factorizes into a kinematic prefactor $\sqrt{\mathcal{R}_a}$ and a coherent sum of model components k. The coherent sum runs over all model components $k \in \mathbb{S}_a$, the set of components included in the model for partial wave a. Each model component combines two ingredients. First, the dynamic amplitude $\mathcal{D}_k(m_{3\pi}; \zeta_k)$ describes the lineshape of component k. In the RMF we will predominantly use the Breit–Wigner amplitude introduced in eq. (4.29). The shape parameters ζ_k encode the resonance parameters, e.g., mass and width of a Breit–Wigner resonance. Second, a complex-valued RMF coupling amplitude ${}^k\mathcal{C}_a$[1] encodes the overall strength and phase with which component k contributes to the partial wave a. ${}^k\mathcal{C}_a$ is an independent complex constant for each component k and wave a. The kinematic prefactor restores the normalization and phase-space conventions absorbed in the PWD step: due to the normalization of the decay amplitudes that we chose (see eq. (4.19)), the factor is given by the square root of the normalization integral (see eq. (4.18))[2]. $\mathcal{R}_a$ is a function of $m_{3\pi}$, with one value per $m_{3\pi}$ bin.

Analogously to the PWD, we cannot measure a global phase in the RMF. Therefore, we require that the RMF coupling amplitude ${}^k\mathcal{C}_a$ of one model component k in one partial wave a be real-valued and positive. This component k in partial wave a is then called the reference component.

Analogously to the spin-density matrix in the PWD formalism (see eq. (4.23)), we construct the model $\hat{\rho}_{ab}$ for the spin-density matrix as follows:

$$\hat{\rho}_{ab}(m_{3\pi}) = \hat{c}_a(m_{3\pi})\,[\hat{c}_b(m_{3\pi})]^* \,. \tag{6.2}$$

6.2 χ^2 Formalism

The spin-density matrix model $\hat{\rho}_{ab}$ defined in eq. (6.2) contains several free parameters, i.e., the complex-valued RMF coupling amplitudes ${}^k\mathcal{C}_a$ and the shape parameters ζ_k of the dynamic amplitudes. All other parameters are known a priori. In order to extract the free ζ_k parameters from the partial-wave amplitudes obtained in the PWD, a χ^2 fit is performed. The χ^2 fit minimizes the deviation between the measured and modeled spin-density matrices. To this end, we introduce the real-valued spin-density matrix Λ_{ab}

$$\Lambda_{ab}(m_{3\pi}) = \begin{cases} \mathrm{Re}\,(\rho_{ab}(m_{3\pi})) & ,\ \text{if a} \leq \text{b} \\ \mathrm{Im}\,(\rho_{ba}(m_{3\pi})) & ,\ \text{if a} > \text{b} \end{cases}, \tag{6.3}$$

which only contains real valued entries by being constructed out of the real and imaginary parts of the spin-density matrix. Note that here the partial-wave labels a and b are indices running from 0 to $n_{\text{waves}} - 1$, where n_{waves} is the number of partial waves. The

[1] Note that this RMF coupling amplitude ${}^k\mathcal{C}_a$ is a different coupling than the complex-valued partial-wave amplitude c_a.

[2] The Monte-Carlo estimator of the normalization integral (see eq. (4.18)) yields $\mathcal{R}'_a(m_{3\pi}) = \mathcal{R}_a(m_{3\pi})/V_4(m_{3\pi})$ rather than $\mathcal{R}_a(m_{3\pi})$, where $V_4(m_{3\pi})$ is the $\tau^- \to \pi^+\pi^-\pi^-\nu_\tau$ four-body phase-space volume. In our implementation we therefore multiply $\mathcal{R}'_a(m_{3\pi})$ by $V_4(m_{3\pi})$ to recover $\mathcal{R}_a(m_{3\pi})$. In eq. (6.1) this factor is contained in $\mathcal{R}_a(m_{3\pi})$ by definition (see eq. (4.18)) and is not written separately.

diagonal elements Λ_{aa} correspond to the intensity of partial wave a. The upper triangle of Λ_{ab} corresponds to the real parts of the ρ_{ab} elements, whereas the lower triangle corresponds to the imaginary parts of the ρ_{ba} elements. The real-valued spin-density matrix Λ_{ab} contains the same information as the spin-density matrix ρ_{ab}, as ρ_{ab} is a hermitian matrix, i.e., $\rho_{ab} = \rho^*_{ba}$.

To further simplify the notation we introduce $\vec{\lambda}$, the vectorized form of Λ_{ab}, given by:

$$\lambda_i(m_{3\pi}) = \Lambda_{ab}(m_{3\pi}), \qquad \text{where} \quad i = a \cdot n_{\text{waves}} + b. \tag{6.4}$$

Analogously we define the analogous quantities for the spin-density matrix model $\hat{\rho}_{ab}$. They read

$$\hat{\Lambda}_{ab}(m_{3\pi}) = \begin{cases} \text{Re}\left(\hat{\rho}_{ab}(m_{3\pi})\right) & \text{, if a} \leq \text{b} \\ \text{Im}\left(\hat{\rho}_{ba}(m_{3\pi})\right) & \text{, if a} > \text{b} \end{cases} \tag{6.5}$$

and

$$\hat{\lambda}_i(m_{3\pi}) = \hat{\Lambda}_{ab}(m_{3\pi}), \qquad \text{where} \quad i = a \cdot n_{\text{waves}} + b. \tag{6.6}$$

We can now use both, the measured and modeled real-valued spin-density vectors given in eqs. (6.4) and (6.6), respectively, to construct the χ^2 function as:

$$\chi^2_{\text{RMF}} = \sum_{m_{3\pi}} \sum_{i,j=0}^{n^2_{\text{waves}}-1} \Delta\lambda_i(m_{3\pi})\, \text{Prec}\left[\lambda_i(m_{3\pi}), \lambda_j(m_{3\pi})\right] \Delta\lambda_j(m_{3\pi}), \tag{6.7}$$

where $\Delta\lambda_i$ represents the difference between the measured and modeled real-valued spin-density vectors, i.e.,

$$\Delta\lambda_i(m_{3\pi}) = \lambda_i(m_{3\pi}) - \hat{\lambda}_i(m_{3\pi}). \tag{6.8}$$

The precision matrix $\text{Prec}\left[\lambda_i(m_{3\pi}), \lambda_j(m_{3\pi})\right]$ is conventionally defined as the inverse of the covariance matrix $\text{Cov}\left[\lambda_i(m_{3\pi}), \lambda_j(m_{3\pi})\right]$. We obtain the full covariance matrix of the real and imaginary parts of the partial-wave couplings c_a extracted from the PWD fit vectorized as $c^{\mathbb{R}} = (\text{Re}\, c_0, \text{Im}\, c_0, \text{Re}\, c_1, \text{Im}\, c_1, \dots)^T$. We propagate the statistical uncertainties of $c^{\mathbb{R}}$ to the real-valued spin-density vector λ entries by a first order Taylor expansion as [10]:

$$\text{Cov}\left[\lambda_i, \lambda_j\right] \approx \sum_{k,l} \left.\frac{\partial \lambda_i}{\partial c^{\mathbb{R}}_k} \frac{\partial \lambda_j}{\partial c^{\mathbb{R}}_l}\right|_{c^{\mathbb{R}}} \text{Cov}\left[c^{\mathbb{R}}_k, c^{\mathbb{R}}_l\right], \tag{6.9}$$

where $\text{Cov}\left[c^{\mathbb{R}}_k, c^{\mathbb{R}}_l\right]$ is the covariance matrix of $c^{\mathbb{R}}$, the vectorized real valued partial-wave couplings[3].

As the spin-density matrix has n^2_{waves} entries, while the partial-wave couplings extracted from the PWD have only $2n_{\text{waves}} - 1$ real degrees of freedom, the covariance matrix

[3]All quantities are functions of $m_{3\pi}$. This dependence was left out for ease of notation. The fits, and hence these quantities, are performed and treated independently across different $m_{3\pi}$ bins.

$\mathrm{Cov}\,[\lambda_i, \lambda_j]$ does not have full rank. A conventional inverse of it therefore cannot be constructed, since some of its eigenvalues are exactly zero. To circumvent this, we use the pseudoinverse of $\mathrm{Cov}\,[\lambda_i, \lambda_j]$ as the precision matrix.

Finally, we minimize the χ^2 function with respect to the free parameters. We start multiple fit attempts, each with its own set of start parameter values. We deem a single fit result to be valid if its covariance matrix is positive definite, i.e., all its eigenvalues are positive, and if none of the fit parameters has reached its parameter limits. Additionally, we require that the same valid χ^2-minimum is found in at least two fit attempts. The values for the free parameters are obtained from the minimum of the χ^2 function. The covariance matrix of the fitted parameters is estimated from the Hessian of the χ^2 function at the minimum.

One of the main advantages of the χ^2 formalism is that it directly provides an indication of how well one model describes the data compared to another. The χ^2 value quantifies the deviation between the modeled and measured real-valued spin-density matrices, thus a larger value generally indicates a worse description of the data. This comparison is only meaningful, however, if the two models have a comparable number of free parameters. For large differences in the number of free parameters, a lower χ^2 value cannot be taken as an indication of a better model, as the additional free parameters may simply allow the model to describe statistical noise more flexibly, without necessarily capturing the underlying physics better.

6.3 Fit Fractions

In this analysis we can extract two different types of fit fractions. The first is the fit fraction of a partial wave a. It is defined as:

$$\mathcal{F}_a = \frac{\tilde{N}_a}{\tilde{N}_{\text{total}}}, \tag{6.10}$$

where $\tilde{N}_a$ is defined analogously to eq. (4.25) as the yield of a partial wave as modeled by the RMF and reads

$$\tilde{N}_a = \sum_{m_{3\pi}} \hat{\rho}_{aa}(m_{3\pi}). \tag{6.11}$$

$\tilde{N}_{\text{total}}$ is the yield of $\tau^- \to \pi^+\pi^-\pi^-\nu_\tau$ decays as modeled by the RMF. It is analogously defined to a sum over the $m_{3\pi}$ bins of eq. (4.24) and is given by

$$\tilde{N}_{\text{total}} = \sum_{m_{3\pi}} \sum_{a,b} \hat{\rho}_{ab}(m_{3\pi}) I_{ab}(m_{3\pi}), \tag{6.12}$$

where I_{ab} is the phase-space integral matrix defined in eq. (4.22). Due to the interference terms between the partial waves generally $\sum_a \mathcal{F}_a \neq 1$ is true. The second fit fraction, is the fit fraction of a model component k in a partial wave a and reads[4]

$$ {}^{k}\mathcal{F}_a = \frac{{}^{k}\tilde{N}_a}{\tilde{N}_a}, \tag{6.13} $$

where ${}^{k}\tilde{N}_a$ corresponds to the yield of a single resonance in partial wave a. We obtain ${}^{k}\tilde{N}_a$ after the RMF model is fit to the PWD fit results, by extracting the model couplings

$$ {}^{k}\hat{c}_a(m_{3\pi}) = \sqrt{\mathcal{R}(m_{3\pi})}\,{}^{k}\mathcal{C}_a\mathcal{D}_k(m_{3\pi};\zeta_k) \tag{6.14} $$

for a single component k in partial wave a. Equivalently to eq. (4.25), we define the corresponding yield ${}^{k}\tilde{N}_a$ as a sum over the $m_{3\pi}$ bins of the absolute square of the model coupling:

$$ {}^{k}\tilde{N}_a = \sum_{m_{3\pi}} |{}^{k}\hat{c}_a(m_{3\pi})|^2. \tag{6.15} $$

We obtain the uncertainties on this yield from a toy Monte Carlo study. Using the fit parameters extracted from the RMF together with their full covariance matrix, we generate 1000 samples from the corresponding multivariate normal distribution, assuming the fit values to be distributed normally. The yield is evaluated for each of the 1000 samples, and from the spread of these yields we extract its standard deviation.

[4] Similarly to eq. (6.10) generally $\sum_k {}^{k}\mathcal{F}_a \neq 1$ due to the interference between the model components k.

7 Analysis Setup and Pseudo-Data Generation

This chapter introduces the analysis setup common to all subsequent studies. We begin in section 7.1 by presenting the base input model used to generate our pseudo-data samples. We call it the base input model, since throughout the rest of the thesis, this input model serves as a base model, and in following studies only small changes will be made to the model. We will mention these changes explicitly. In section 7.2 we describe the simulated data samples used to perform the studies presented in this work. In section 7.3 we present the PWD model used throughout this thesis. Analogously to the input model, we introduce a base RMF model in section 7.4, since all resonance-model fits performed in this thesis are based on this model, and in following studies only small changes will be made to it. We will mention these changes explicitly. Finally, section 7.5 presents the standard plot format used throughout, together with the definition of the pulls shown in all result figures.

7.1 Input Model

In order to be able to perform the studies shown in this work, an input model is needed to generate pseudo-data samples, and to be able to compare the extracted parameters to it. To this end, we need a set of partial-waves, their complex partial-wave couplings, the resonances that contribute to each partial wave as well as their resonance parameters, e.g., masses and widths. We used the analysis of the Belle $\tau^- \to \pi^+\pi^-\pi^-\nu_\tau$ decays [17] as inspiration for our own analysis, adopting nine of the observed partial waves together with their partial-wave couplings. Since no full RMF was performed in that analysis, the resonance content of each wave is not known a priori. Instead, we construct a model for each wave that reproduces the intensity and phase structures observed in that analysis. Table 7.1 shows the partial waves we chose, the intermediate resonances X^- we model into each partial wave and the partial wave amplitude we used to model the partial wave. We use the resonance parameters determined by the PDG [10] as input values. Table 7.2 lists the resonance parameters as well as their lineshapes as used in our input model. All 3π resonances X^- are modeled by a Breit–Wigner

Table 7.1: Base input model for data generation. The left column lists the partial waves included in our input model. The middle column lists the resonancese X contributing to each partial wave. The last column lists the coupling of each resonance in our model. The couplings are inspired from ref. [17].

Partial wave	Intermediate resonance X	Coupling
$1^{+}\rho(770)\pi S$	$a_1(1260)$	7389
$1^{+}\sigma\pi P$	$a_1(1260)$	$2700e^{i121^\circ}$
	$a_1(1640)$	$270e^{i91^\circ}$
$1^{+}\rho(770)\pi D$	$a_1(1260)$	$507.6e^{i12^\circ}$
	$a_1(1640)$	$907.2e^{i-168^\circ}$
$1^{+}\rho(1450)\pi D$	$a_1(1640)$	$451.3e^{i154^\circ}$
$1^{+}f_2(1270)\pi P$	$a_1(1260)$	$613.4e^{i-86^\circ}$
$1^{+}f_0(980)\pi P$	$a_1(1420)$	$390e^{i-154^\circ}$
$0^{-}\rho(770)\pi P$	$\pi(1300)$	$405e^{i-64^\circ}$
$0^{-}f_0(980)\pi S$	$\pi(1300)$	$81e^{i-28^\circ}$
$1^{-}\omega(782)\pi P$	$\rho(1450)$	$351.9e^{i145^\circ}$

Table 7.2: Input parameters of 3π and isobar resonances. The left column lists the name of the resonance. The next two columns list the mass and width of the resonances. The last column lists the lineshape of the resonance: Breit–Wigner (eq. (4.29)), Gounaris–Sakurai (eq. (4.31)), Flatté (eq. (4.34)), and Pennington (eq. (4.35)). For the Flatté and Au-Morgan-Pennington-Kachaev parameterizations the input parameters are discussed in section 4.7.

Resonance	Mass [MeV/c^2]	Width [MeV/c^2]	Lineshape
$a_1(1260)$	1230	425	Breit–Wigner
$a_1(1420)$	1410	150	Breit–Wigner
$a_1(1640)$	1660	250	Breit–Wigner
$\pi(1300)$	1300	400	Breit–Wigner
$\rho(1450)$	1465	400	Breit–Wigner
$\rho(770)$	775.26	147.4	Gounaris–Sakurai
$f_2(1270)$	1275.5	186.7	Breit–Wigner
$\omega(782)$	782.66	8.68	Breit–Wigner
σ			Pennington
$f_0(980)$			Flatté

amplitude (see eq. (4.29)), evaluated for the dominant decay channel of each resonance[1]. The isobars, however, are not all modeled by Breit–Wigner amplitudes: the $\rho(770)$ uses the Gounaris–Sakurai parameterization (see eq. (4.31)), while the σ and $f_0(980)$ are described by the Au-Morgan-Pennington-Kachaev (see eq. (4.35)) and Flatté (see eq. (4.34)) parameterizations, respectively.

7.2 Data Samples

We use several data samples in this work. In chapter 3, the MC15rd sample was introduced. This sample contains both signal and background events. As this sample is computationally very expensive to create, it contains only about 73×10^6 events[2]. The generation of the pseudo data, described below, retains only a small fraction of the events, so the MC15rd sample would be too small for the input-output studies. Therefore, we use a second, run-independent Monte-Carlo sample, referred to as MC15ri. In contrast to the MC15rd sample, it does not reproduce the conditions of the individual data-taking periods, so a larger sample can be generated at lower computational cost. It contains about 165×10^6 signal events and no background events.

Using the input model described in section 7.1, pseudo data samples are generated from the MC15ri sample via an accept-reject procedure [68]. This procedure retains less than 2 % of the events and yields a sample whose distribution follows that of the input model. We then merge the background events from the MC15rd sample into the pseudo data sample, retaining the background-to-signal fractions of the MC15rd sample [25].

Additionally, the MC15ri sample is also used to calculate the phase-space and reconstructed integral matrices (see eqs. (4.22) and (4.28))[3]. Because the accept-reject procedure retains only a small fraction of the events, the pseudo-data sample and the sample used to compute the integral matrices are effectively statistically independent. Reusing the same MC15ri sample for both purposes therefore does not introduce a relevant correlation between them. For the phase-space integral matrix, the MC15ri sample before detector simulation and event selection is used, so that no resolution or acceptance effects enter. For the reconstructed integral matrix, the generator-level kinematic variables of the MC15ri sample after detector simulation and event selection

[1] The dominant decay channel enters through the dynamic width $\Gamma(s)$ (see eq. (4.29)). As an example, all lineshapes of the $a_1(1260)$ are evaluated for the decay into $\rho(770)\pi$ in an S-wave configuration.
[2] The MC15rd sample is weighted to correspond to an integrated luminosity of $\mathcal{L} = 361.654\,\mathrm{fb}^{-1}$. The luminosity weights are not used in the PWD, therefore only the event numbers are relevant here.
[3] Note that the MC15ri sample is generated with a physics model that we need to weight out. This process is described in ref. [25].

Table 7.3: Thresholds of the partial waves used throughout this thesis. Values taken from ref. [25].

Partial wave	$m_{3\pi}^{\min}$ [GeV/c^2]	**Partial wave**	$m_{3\pi}^{\min}$ [GeV/c^2]
$1^{+}\rho(770)\pi S$	0.80	$0^{-}\rho(770)\pi P$	0.86
$1^{+}(\pi\pi)_S\pi P$	0.80	$0^{-}f_0(980)\pi S$	1.20
$1^{+}\rho(770)\pi D$	0.86	$1^{-}\omega(782)\pi P$	0.80
$1^{+}\rho(1450)\pi D$	1.06		
$1^{+}f_2(1270)\pi P$	0.80		
$1^{+}f_0(980)\pi P$	1.10		

are used. The acceptance effects thereby enter implicitly through the event losses during detector simulation, reconstruction, and event selection, which is precisely what the reconstructed integral matrix is intended to model.

7.3 PWD Model

In the PWD we model all the partial waves included in the input model, using the same isobar lineshapes as listed in table 7.2. This choice of partial waves requires thresholds on the fitted $m_{3\pi}$ range of several partial waves (see section 4.10 for details). The threshold values, listed in table 7.3, were determined in ref. [25], to which we refer for details on how they were obtained. We choose the $1^{+}\rho(770)\pi S$ wave as the reference wave, since it is the dominant wave.

7.4 Base RMF Model

In the following we will describe the RMF model used for most of the RMF studies performed in this work. If it is not explicitly stated otherwise, we use the model explained here. Generally, we fit all partial waves listed in table 7.1 simultaneously. We include the full $m_{3\pi}$ ranges as listed in table 7.4. Due to the thresholding in the PWD it was not necessary to exclude PWD fit results from the RMF. This must be investigated again when we use the data sample obtained from the Belle II detector. We model each partial wave with the same resonances as in the input model (see table 7.1), where we leave all resonance parameters, i.e., mass and widths of the resonances, as free parameters in the fit. We impose certain limits on the resonance parameter limits for two main reasons. First, we want to restrict the RMF to not find unphysical

Table 7.4: $m_{3\pi}$ ranges that each partial wave is modeled in by the RMF. Note that the values shown here correspond to the bin centers, e.g. if one bin goes from 1.68 to 1.70 GeV/c^2 its bin center is at 1.69 GeV/c^2.

Partial wave	$m_{3\pi}$ range [GeV/c^2]	
$1^+\rho(770)\pi S$	0.81	1.69
$1^+(\pi\pi)_S\pi P$	0.81	1.69
$1^+\rho(770)\pi D$	0.87	1.69
$1^+\rho(1450)\pi D$	1.07	1.69
$1^+f_2(1270)\pi P$	0.81	1.69
$1^+f_0(980)\pi P$	1.11	1.69
$0^-\rho(770)\pi P$	0.87	1.69
$0^-f_0(980)\pi S$	1.21	1.69
$1^-\omega(782)\pi P$	0.81	1.69

Table 7.5: Limits on the Breit–Wigner resonance parameters in the base RMF model.

Resonance		Limits [MeV/c^2]	
		lower	upper
$a_1(1260)$	m_0	1000	1400
	Γ_0	10	1000
$a_1(1420)$	m_0	1200	1800
	Γ_0	10	600
$a_1(1640)$	m_0	1500	1800
	Γ_0	10	600
$\pi(1300)$	m_0	1100	1800
	Γ_0	10	900
$\rho(1450)$	m_0	1100	1800
	Γ_0	10	700

results. Therefore, we restrict the range of the resonance parameters to the physically possible region, making the ranges large enough to not bias the results. Second, we do not want two resonances in the same partial wave to overlap or be interchangeable. Therefore, we choose limits on the mass parameter of the $a_1(1260)$ and $a_1(1640)$ so that they are distinct. The parameter limits imposed on the resonance parameters are listed in table 7.5, and were chosen based on the input parameters in table 7.2. We choose the $a_1(1260)$ in the $1^+\rho(770)\pi S$ wave as the reference component in the

RMF.

7.5 Visualization and Pulls

As most of the plots resulting from an RMF follow the same scheme, we will introduce these types of plots in the following. Figure 7.1 shows an exemplary RMF intensity spectrum. The plot is separated into two parts. The upper part shows the intensity of the PWD fit results as blue dots. The RMF result curve is depicted by a solid red curve. The input model is shown by a dashed red curve. The lower part shows the pulls [69], which we define as

$$\mathrm{pull}_i = \frac{f_i - \hat{f}_i}{\sigma_i}, \tag{7.1}$$

where the index i denotes the $m_{3\pi}$ bin, f_i corresponds to the PWD fit result, $\hat{f}_i$ to the RMF curve value, and σ_i to the statistical uncertainty on the PWD fit result. The pulls in the RMF fit region are shown by blue bars. More generally, eq. (7.1) is used throughout this work with f_i denoting the measured quantity, $\hat{f}_i$ the expected value, and σ_i the statistical uncertainty on the measured quantity. The pull quantifies, in units of the standard deviation σ, how far a measured quantity deviates from its expected value. Figure 7.2 shows the relative phase spectrum of a partial wave versus the reference wave. Its scheme is analogous to fig. 7.1.

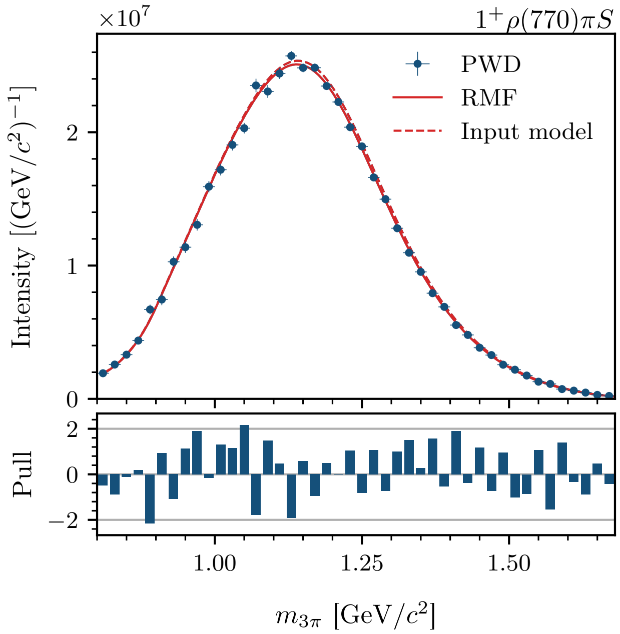

Figure 7.1: Exemplary intensity spectrum of an RMF result, for the partial-wave labeled in the top right corner. The upper part shows the intensity spectrum as a function of $m_{3\pi}$. The blue data points correspond to the intensities obtained from the PWD. The solid red curve corresponds to the RMF result. The dashed red curve is the intensity of the input model (see section 7.1). The model curve is rescaled such that the modeled number of measured signal events matches the total number of signal events in the pseudo data sample. Both the RMF and model curves are calculated for 45 $m_{3\pi}$ bins. We interpolate between them using a cubic spline, resulting in 300 intensity model points in total. This procedure avoids non-smooth features between adjacent bins. The lower part shows the pulls between the PWD data points and the RMF curve, as defined in eq. (7.1). The pulls in the RMF fit region are shown by blue bars.

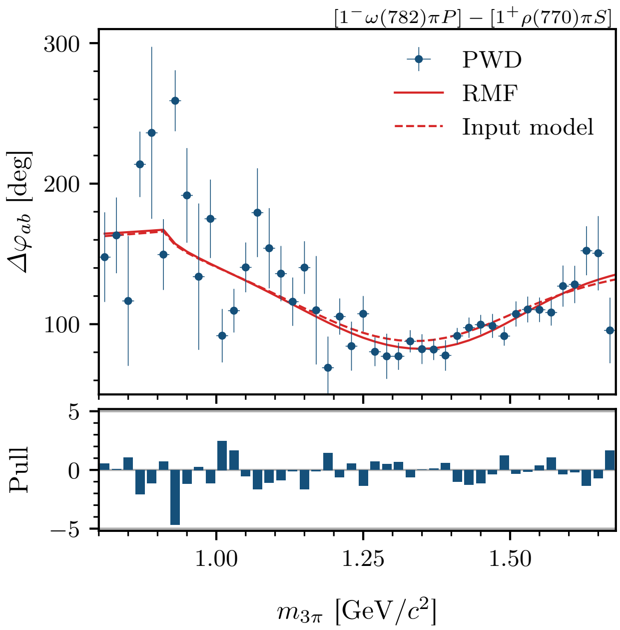

Figure 7.2: Exemplary relative phase of an RMF result. The two partial-wave names in the top right corner indicate the waves between which the relative phase is calculated, with the subtrahend corresponding to the reference wave. The upper part shows the phase motion in dependence on the invariant mass of the 3π system. The blue data points correspond to the phase motions obtained from the PWD. The solid red curve corresponds to the RMF result. The dashed red curve is the phase motion of the input model. The lower part shows the pulls between the PWD data points and the RMF curve, as defined in eq. (7.1). The pulls in the RMF fit region are shown by blue bars.

8 Consistency Studies for the RMF

The RMF formalism introduced in chapter 6 is well established and used in many analyses, such as in refs. [12, 14, 17]. To validate its applicability to our analysis and its correct implementation in our fit framework, we perform input-output studies. Rigorously determining the intrinsic analysis bias would require generating and analysing many pseudo-data samples, which is computationally not feasible. We therefore perform two input-output studies on two different pseudo-data samples to obtain an estimate of the intrinsic analysis bias.

For these input-output studies we generate two different pseudo-data samples. The first is generated to be as close as possible to the data we expect from the real measurement. We inject the input model described in section 7.1 onto the MC15ri sample and merge background events from the MC15rd sample into it. We refer to this sample as the reconstructed pseudo-data sample. The second sample is generated similarly, but the four-momenta are used as generated by the Monte-Carlo simulation, so that this sample contains no resolution effects, and no background events are merged in. We refer to this sample as the signal-only pseudo-data sample.

These two pseudo-data samples let us investigate different properties of the PWA. Each of them individually provides an estimate of the intrinsic analysis bias. Taken together, they let us investigate the effect of including background events and resolution effects in our sample. As resolution effects are neglected in our PWA formalism, comparing the two samples lets us observe their impact on the extracted results. Section 8.1 presents the input-output study performed on the signal-only pseudo-data sample, and section 8.2 the one performed on the reconstructed pseudo-data sample.

8.1 RMF to Signal-Only Pseudo-Data Sample

We first investigate the resonance parameters extracted from the RMF to the signal-only pseudo-data sample in table 8.1. We observe that the deviations from their input values are of the order of $10\,\mathrm{MeV}/c^2$ for all resonances except the $\rho(1450)$, which shows deviations of the order of $50\,\mathrm{MeV}/c^2$. Compared to their statistical uncertainties the $a_1(1260)$

Table 8.1: Resonance parameters obtained from the RMF to the signal-only pseudo-data sample. The left column names the resonance. The second column shows the obtained mass in the RMF. The third column shows the deviation of the mass from the input value shown in table 7.2. The last two columns show the same, but for the obtained width.

Resonance	Mass [MeV/c^2]	Δ(Mass) [MeV/c^2]	Width [MeV/c^2]	Δ(Width) [MeV/c^2]
$a_1(1260)$	1227.79 ± 0.30	-2.21	424.2 ± 0.7	-0.8
$a_1(1420)$	1408.7 ± 1.9	-1.3	156 ± 4	6
$a_1(1640)$	1654.5 ± 2.6	-5.5	260 ± 5	10
$\pi(1300)$	1312 ± 11	12	407 ± 25	7
$\rho(1450)$	1496 ± 12	30	350 ± 40	-50

Table 8.2: Yields of the partial waves obtained from the RMF fitted to the signal-only pseudo-data sample are shown in the second column (see eq. (6.11)). The third column shows the corresponding yield of the input model. The fourth column shows the yield of the partial waves as obtained from the PWD using eq. (4.25). The last two columns show the deviation of the RMF and PWD yield from the input value, respectively.

Wave	RMF ($\times 10^3$)	Input ($\times 10^3$)	PWD ($\times 10^3$)	$\Delta_{\mathrm{RMF-Input}}$ ($\times 10^3$)	$\Delta_{\mathrm{PWD-Input}}$ ($\times 10^3$)
$1^+\rho(770)\pi S$	9517 ± 15	9651	9469 ± 35	-168	-182
$1^+(\pi\pi)_S\pi P$	1272 ± 6	1259	1276 ± 10	13	17
$1^+\rho(770)\pi D$	177.9 ± 3.4	174.3	175 ± 4	3.6	0.7
$1^+\rho(1450)\pi D$	32.1 ± 1.1	35.9	35.4 ± 1.5	3.8	-0.5
$1^+f_2(1270)\pi P$	64.1 ± 1.8	66.4	64.7 ± 2.3	2.3	-1.7
$1^+f_0(980)\pi P$	27.1 ± 0.8	26.9	28.6 ± 1.0	-0.2	1.7
$0^-\rho(770)\pi P$	18.1 ± 1.8	29.0	20.8 ± 2.1	-8.9	-8.2
$0^-f_0(980)\pi S$	1.08 ± 0.34	1.16	1.58 ± 0.34	-0.08	0.42
$1^-\omega(782)\pi P$	15.5 ± 0.9	21.9	19.6 ± 1.2	-6.4	-2.3

stands out, as the deviation of its mass parameter is large compared to its small statistical uncertainty, leading to a pull of $7.4\,\sigma$ (see eq. (7.1)). The other resonance parameters lie within a $3\,\sigma$ interval of their input parameter.

We then also investigate the partial-wave yields as extracted by the RMF and PWD and their deviations from their input model values as shown in table 8.2. The dominating $1^+\rho(770)\pi S$ wave stands out, with a deviation of both the RMF and PWD from the input value of about 180×10^3. When compared to the absolute value of the yield,

Table 8.3: Yields of the resonance components in the partial waves. Only the two partial waves with more than one model component are shown. The left column indicates the wave or the resonance within the partial wave. If the partial wave is shown the RMF and input yield of the partial wave are shown. These are the same values as already shown in table 8.2. If a resonance name is shown, then the second column shows the yield of the resonance component in a partial wave obtained in the RMF (see eq. (6.15)). The third column shows the input value for the yield. The last column shows the deviation of RMF yield from input yield.

Wave	RMF ($\times 10^3$)	Input ($\times 10^3$)	$\Delta_{\text{RMF}-\text{Input}}$ ($\times 10^3$)
$1^+(\pi\pi)_S\pi P$	1272 ± 6	1259	13
$a_1(1260)$	1309 ± 9	1287	22
$a_1(1640)$	18.7 ± 1.1	12.8	5.9
$1^+\rho(770)\pi D$	177.9 ± 3.4	174.3	3.6
$a_1(1260)$	38.7 ± 1.5	45.5	-6.8
$a_1(1640)$	141.2 ± 3.4	145.2	4.0

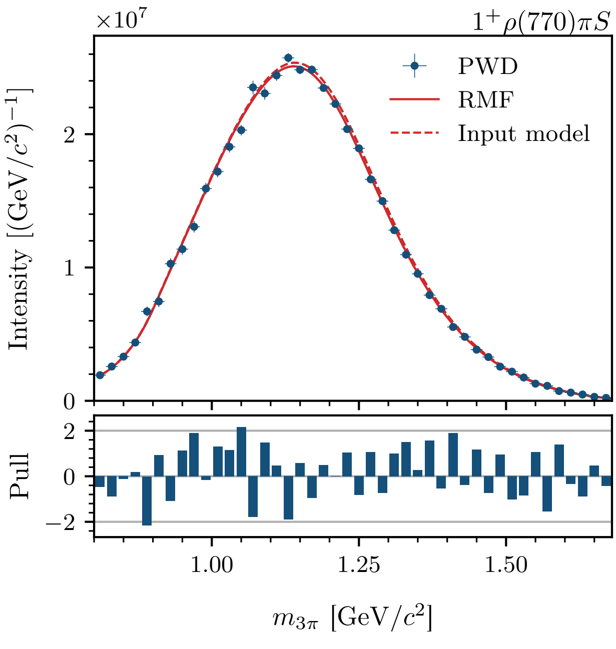

Figure 8.1: Same as fig. 7.1, but showing the intensity spectrum of the $1^+\rho(770)\pi S$ wave of the input-output study on the signal-only pseudo-data sample.

this corresponds to a deviation of about 2 %. Due to the small statistical uncertainties, this results in a pull of about $11\,\sigma$ for the RMF compared to the input. Towards partial waves with smaller yields, the absolute deviation decreases. One of these waves, the $1^{-}\omega(782)\pi P$ wave, has a deviation of -6.4×10^{3} from RMF to input model. Compared to its absolute value this deviation is about 40 %, and leads to a pull of about $7\,\sigma$ for the RMF compared to the input. All other waves have pulls of less than $5\,\sigma$.

Table 8.3 shows the yields of the individual resonance components in the two partial waves to which more than one model component contributes. The yields are compared to their input value. As in table 8.2, the deviations are small when compared to their absolute value.

Figure 8.1 shows the intensity spectrum of the dominating $1^{+}\rho(770)\pi S$ wave. As already observed from the resonance parameters of the $a_1(1260)$ and the yield of this wave, we see little deviation of the RMF from the input model curve. Although the resonance parameters and the yields deviate significantly from their input values, the RMF curve lies close to the input model curve.

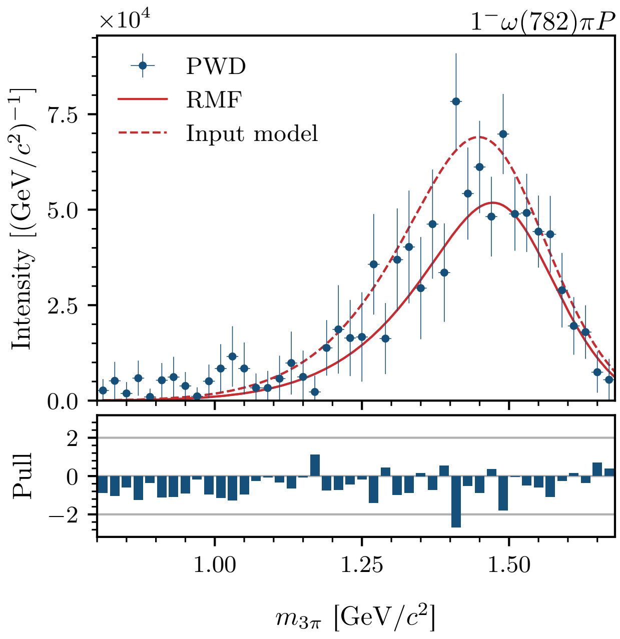

Figure 8.2: Same as fig. 7.1, but showing the intensity spectrum of the $1^{-}\omega(782)\pi P$ wave of the input-output study on the signal-only pseudo-data sample.

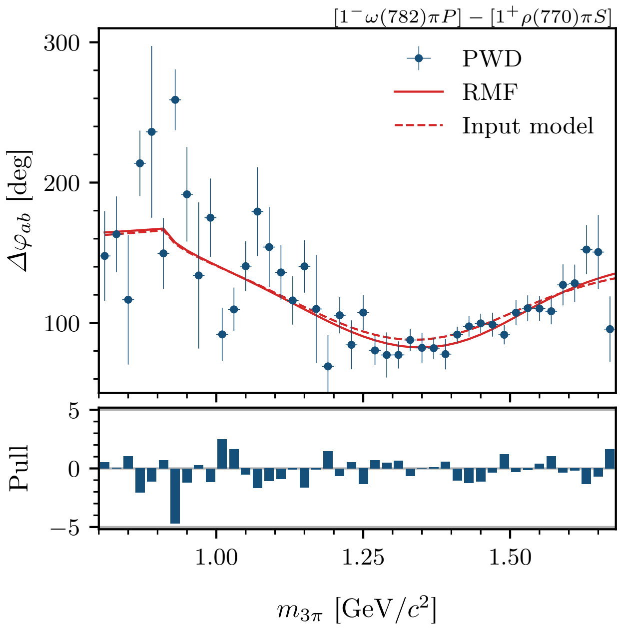

Figure 8.3: Same as fig. 7.1, but showing the relative phase spectrum of the $1^{-}\omega(782)\pi P$ wave compared to the $1^{+}\rho(770)\pi S$ wave of the input-output study on the signal-only pseudo-data sample.

We then investigate the intensity spectrum of another partial wave, which contains much less intensity, the $1^{-}\omega(782)\pi P$ wave shown in fig. 8.2. In this wave only the $\rho(1450)$ resonance contributes. Its resonance parameters deviate less significantly from their input values than those of the $a_1(1260)$, but show a larger overall deviation. This can be observed in the intensity spectrum, as the peaks of the RMF and input model are clearly shifted relative to one another. We also observe in the plot that the RMF curve has less intensity than the input model, as can also be seen from the yield of this wave shown in table 8.2. But we also observe that the PWD results already deviate from their input values. The pulls of the RMF from the PWD results show mostly values below $2\,\sigma$. The corresponding phase spectrum can be observed in fig. 8.3. It shows a pull of up to $5\,\sigma$ in one $m_{3\pi}$ bin, but overall the pulls are low and similar in size to those in the intensity spectrum.

8.2 RMF to the Reconstructed Pseudo-Data Sample

Table 8.4 shows the resulting resonance parameters from an RMF to the reconstructed pseudo-data sample. Resonances found in partial waves with high intensity show small

Table 8.4: Resonance parameters resulting from the RMF to the reconstructed pseudo-data sample. The columns show the same quantities as table 8.1.

Resonance	Mass [MeV/c^2]	Δ(Mass) [MeV/c^2]	Width [MeV/c^2]	Δ(Width) [MeV/c^2]
$a_1(1260)$	1227.0 ± 0.4	-3.0	425.0 ± 0.9	0.0
$a_1(1420)$	1418.0 ± 2.2	8	149 ± 4	-1
$a_1(1640)$	1646.5 ± 2.9	-13.5	268 ± 6	18
$\pi(1300)$	1343 ± 10	43	370 ± 21	-30
$\rho(1450)$	1444 ± 11	-21	390 ± 40	-10

Table 8.5: Same columns as table 8.2 for the reconstructed pseudo-data sample.

Wave	RMF ($\times 10^3$)	Input ($\times 10^3$)	PWD ($\times 10^3$)	$\Delta_{\mathrm{RMF-Input}}$ ($\times 10^3$)	$\Delta_{\mathrm{PWD-Input}}$ ($\times 10^3$)
$1^+\rho(770)\pi S$	9107 ± 17	9598	9240 ± 4	-491	-358
$1^+(\pi\pi)_S\pi P$	1208 ± 7	1254	1255 ± 12	-46	1
$1^+\rho(770)\pi D$	176.4 ± 3.4	173.8	172 ± 4	2.6	-1.8
$1^+\rho(1450)\pi D$	31.7 ± 1.2	35.8	32.0 ± 1.5	-4.1	-3.8
$1^+f_2(1270)\pi P$	55.2 ± 1.8	66.3	55.3 ± 2.7	-11.1	-11.0
$1^+f_0(980)\pi P$	27.8 ± 0.9	26.9	21.4 ± 0.9	0.9	-5.5
$0^-\rho(770)\pi P$	22.5 ± 2.0	28.9	31.5 ± 2.9	-6.4	2.6
$0^-f_0(980)\pi S$	1.5 ± 0.4	1.2	2.3 ± 0.4	0.3	1.1
$1^-\omega(782)\pi P$	28.9 ± 1.6	21.8	30.0 ± 1.8	7.1	8.2

absolute deviations from their input parameters, but due to the high statistical precision on the input parameters this results in large pulls. For example, the mass of the $a_1(1260)$ deviates by $-3.0\,\mathrm{MeV}/c^2$ from its input value, resulting in a pull of $-7.5\,\sigma$. Resonances found in partial waves with decreasing intensities show larger deviations from their input value, but due to smaller statistical precision the pulls are smaller. The $\rho(1450)$, for example, deviates by $-21\,\mathrm{MeV}/c^2$ from its mass input value, resulting in a pull of about $2\,\sigma$.

Tables 8.5 and 8.6 show the partial-wave yields and resonance-component yields, respectively. Here, the $1^+\rho(770)\pi S$ wave is worth studying more closely. The deviation of the RMF from the input value is -491×10^3. The resulting pull is about $-28\,\sigma$. We also observe that the PWD already deviates from the input value, with a pull of over $-80\,\sigma$. The deviation between the PWD and RMF, however, is comparably small, with only 133×10^3. All the other partial waves show smaller deviations, below $6\,\sigma$.

Table 8.6: Same columns as table 8.3 for the reconstructed pseudo-data sample.

Wave	RMF ($\times 10^3$)	Input ($\times 10^3$)	$\Delta_{\text{RMF}-\text{Input}}$ ($\times 10^3$)
$1^+(\pi\pi)_S\pi P$	1208 ± 7	1254	-46
$a_1(1260)$	1211 ± 10	1281	-70
$a_1(1640)$	7.5 ± 0.8	12.8	-5.3
$1^+\rho(770)\pi D$	176.4 ± 3.4	173.8	2.6
$a_1(1260)$	35.4 ± 1.7	45.4	-10.0
$a_1(1640)$	165 ± 4	145	20

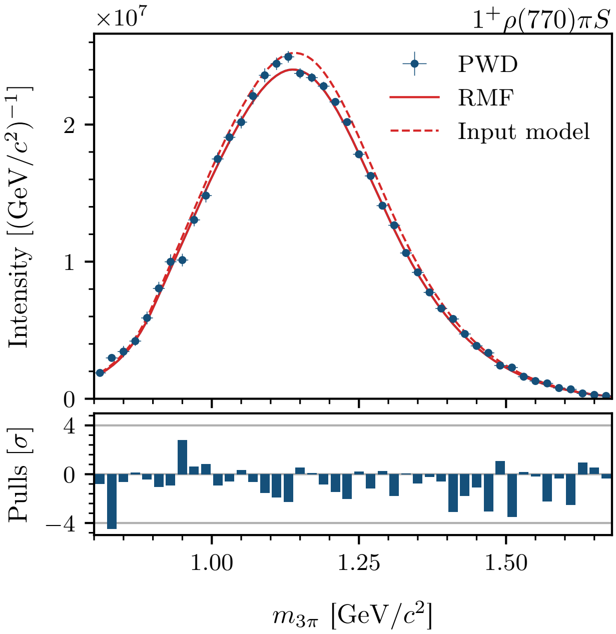

Figure 8.4: Same as fig. 7.1, but showing the intensity spectrum of the $1^+\rho(770)\pi S$ wave of the input-output study on the reconstructed pseudo-data sample.

Comparing these values to the signal-only pseudo-data sample, we observe similar features. Resonance components and yields of partial waves with higher intensities have smaller percentage deviations, but larger pulls. As the intensity of a partial wave decreases, the percentage deviations increase, but the pulls tend to decrease. Overall, the deviations in the reconstructed pseudo-data sample are larger than those in the signal-only sample.

Figure 8.4 shows the intensity spectrum for the $1^+\rho(770)\pi S$ wave. We observe the same features as indicated by the table. As the resonance parameters deviate by less

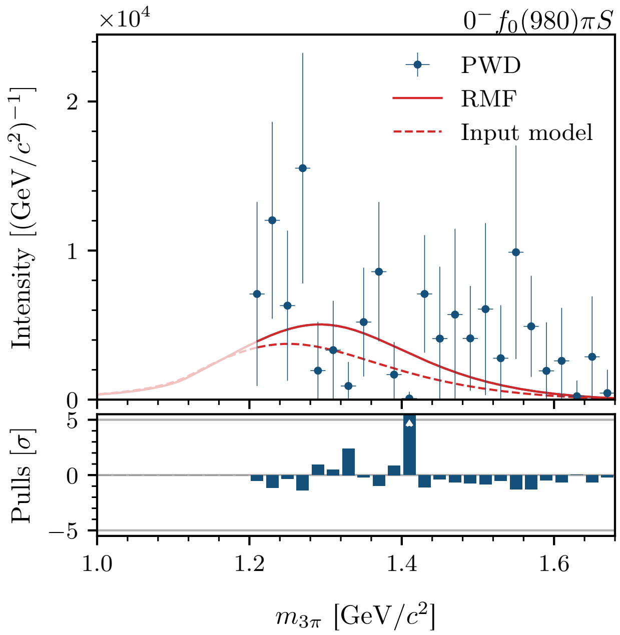

Figure 8.5: Same as fig. 7.1, but showing the intensity spectrum of the $0^- f_0(980)\pi S$ wave of the input-output study on the reconstructed pseudo-data sample.

than $3\,\mathrm{MeV}/c^2$, the input model and RMF curve exhibit the same overall structure. We also observe the significant deviation of the partial-wave yield: the input model and RMF curve have different intensities. The blue PWD fit results show a drop in intensity at about $1.15\,\mathrm{GeV}/c^2$, which is modeled neither in the input model nor in the RMF. The RMF curve passes well through the data points, with pulls that systematically undershoot but stay below $4\,\sigma$ except for one $m_{3\pi}$ bin.

The intensity spectrum of the $0^- f_0(980)\pi S$ wave is shown in fig. 8.5. The PWD fit results do not exhibit a clear peak. As seen in table 8.4, the resonance parameters of the $\pi(1300)$, the only resonance contributing to this partial wave, deviate by $43\,\mathrm{MeV}/c^2$ and $-30\,\mathrm{MeV}/c^2$ from their input values. This can be observed in the plot, as the peak position of the RMF curve is clearly shifted compared to the input model curve. The widths the two curves exhibit also clearly deviate. Overall, the pulls of the RMF compared to the PWD fit results show values below $3\,\sigma$, except for one $m_{3\pi}$ bin.

Across both input-output studies we observe statistically significant deviations of the extracted resonance parameters and yields from their injected input values. We refer to such deviations as the intrinsic analysis bias. For a more thorough discussion of the intrinsic analysis bias, we refer the reader to chapter 11.

9 Studies on $a_1(1420)$ Resonance

In order to understand the possible origins of the $a_1(1420)$, we first review its experimental observation. The COMPASS collaboration reported a resonance-like signal in the $1^{++}0^{+} f_0\pi P$ wave of their $\pi^- p \to \pi^+\pi^-\pi^- p$ data (black points in fig. 9.1), collected with a 190 GeV/c π^- beam impinging on a fixed hydrogen target [13]. Their partial-wave

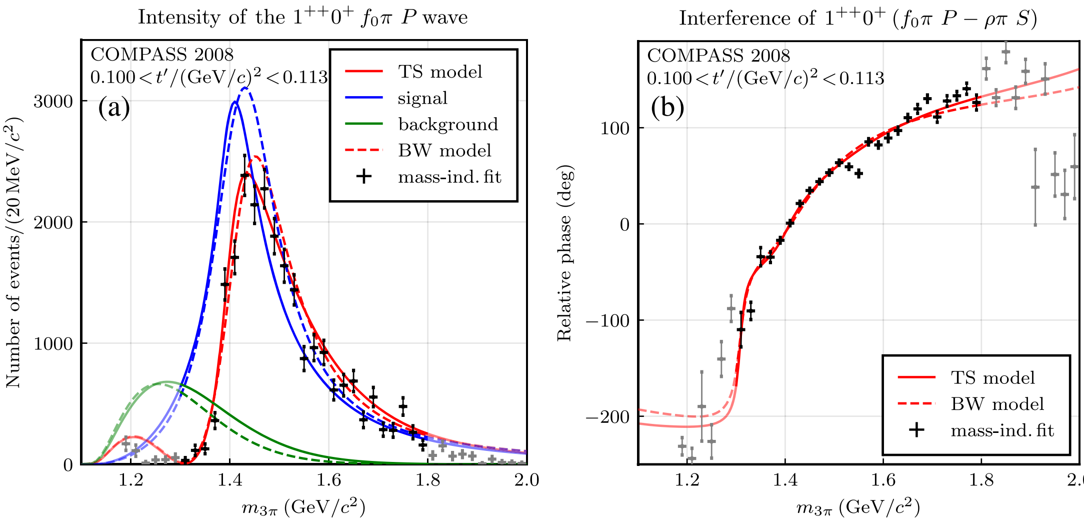

Figure 9.1: Intensity spectrum in (a) of $J^{PC}M^{\epsilon}\xi\pi L = 1^{++}0^{+}f_0\pi P$ wave of $\pi^- p \to \pi^+\pi^-\pi^- p$ scattering data from COMPASS. The plot is shown for one t' bin labeled at the top of the plot, where t' corresponds to the reduced 4-momentum transfer squared. The black points are the PWD intensity in 20 MeV/c^2 bins. The red dashed curve corresponds to the RMF model curve. The blue dashed line corresponds to the Breit–Wigner intensity fitted into the data. The green dashed line corresponds to the non-resonant term. The solid lines correspond to the RMF, where instead of a Breit–Wigner a triangle singularity amplitude was used. (b) shows the relative phase between the $1^{++}0^{+}f_0\pi P$ and $1^{++}0^{+}\rho\pi S$, with the same convention for the (dashed) curves. Figure adapted from ref. [70].

label $a = J^{PC}M^{\epsilon}\xi\pi L$[1] is similar to ours in eq. (4.1). In several cross-checks the validity of the signal was studied. These extensive studies, including the use of a "freed-isobar" approach [72, 73], confirmed the existence of the $a_1(1420)$ signal unambiguously. The resonance was named $a_1(1420)$, since its quantum numbers are $I^G(J^{PC}) = 1^-(1^{++})$, following the PDG convention [10]. An RMF performed on this signal yielded a Breit–Wigner mass of $m = (1414^{+15}_{-13})\,\mathrm{MeV}/c^2$ and width of $\Gamma = (153^{+8}_{-23})\,\mathrm{MeV}/c^2$ [20]. There are three properties of this signal that suggest it does not correspond to a resonance of the constituent quark model:

1. The Breit–Wigner width of about $150\,\mathrm{MeV}/c^2$ is much smaller than that of the $a_1(1260)$ ($\Gamma_{a_1(1260)} \approx 400\,\mathrm{MeV}/c^2$), which is the axial-vector ground state.

2. In the framework of Regge theory, the squared masses of light-meson resonances rise linearly with their radial excitation number [74, 75]. Successive radial excitations of the a_1 therefore lie at roughly equal spacings in m^2, placing the first radial excitation near $1655\,\mathrm{MeV}/c^2$, i.e., the mass of the $a_1(1640)$, whereas the $a_1(1420)$ sits only at about $1414\,\mathrm{MeV}/c^2$.

3. The $a_1(1420)$ has so far been observed only in the $f_0(980)\pi$ decay channel. If it were a genuine radial excitation of the $a_1(1260)$, one would expect it to contribute to further decay channels as well.

As the $a_1(1420)$ signal is not expected to be a genuine resonance, we cannot describe it by a Breit–Wigner amplitude, which approximates narrow and isolated resonance. Several explanations have been proposed for the origin of the $a_1(1420)$, such as modelling it as an axial-vector tetraquark state [76], as well as other exotic configurations [77, 78]. We will, concentrate on the triangle singularity model [70] shown in fig. 9.2. This model assumes that the high-mass tail of the $a_1(1260)$, above the $K^*\bar{K}$ threshold, decays into the $K^*\bar{K}$ system. The K^* then decays into a $K\pi$ system. The K, and the $\bar{K}$ rescatter into the $f_0(980)$ isobar, which then decays into the final 2π system. Therefore, the signal is modeled as a kinematic rescattering effect and not as a genuine resonance. This triangle singularity model generates a resonance-like signal in the intensity spectrum with a corresponding relative phase (see solid lines in fig. 9.1). This model can explain several of the issues of this resonance-like signal discussed above. This explains why this signal only appears in the $1^{++}0^{+}f_0\pi P$ wave, as the $K\bar{K}$ system only rescatters into the $f_0(980)$. It would also explain why this signal sits right above the $K^*\bar{K}$ mass threshold, where we would not expect a radial excitation of the ground state.

[1]Compared to our decay notation, there are additional quantum numbers. C is the charge conjugation parity. M^{ϵ} are specific to the scattering context and denote the projection of spin J onto the beam direction in the reflectivity basis [71].

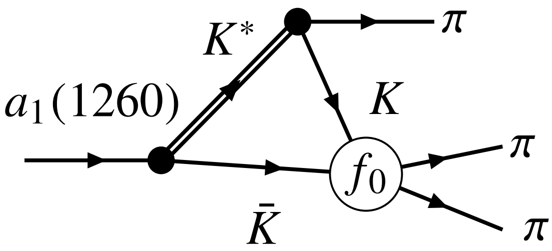

Figure 9.2: Representative graph of the triangle amplitude. Graph taken from [79].

The COMPASS collaboration tested both the triangle-singularity and Breit–Wigner amplitude models in an RMF. In a detailed study, they found that the triangle-singularity amplitude consistently describes the measured partial-wave amplitude slightly better than the Breit–Wigner amplitude. Because the intensity and phase spectra of the two models are very similar and the improvement is only marginal, no definitive conclusion could be reached on whether the triangle-singularity model fully accounts for the observed signal. The diffractive process $\pi^- p \to \pi^+\pi^-\pi^- p$ studied by COMPASS contains a large non-resonant contribution (green curves in fig. 9.1(a)), describing production of the 3π system without an intermediate resonance. In the $\tau^- \to \pi^+\pi^-\pi^-\nu_\tau$ decay studied at Belle II, the 3π system is instead produced through the weak charged current with well-defined J^P, and no analogous diffractive production mechanism is present. Our data sample is therefore not expected to contain such a non-resonant contribution. Since this contribution can absorb a substantial fraction of the observed intensity, a data set without it may allow a more decisive test of whether the triangle-singularity mechanism accounts for the observed signal. Section 9.1 discusses how the triangle-singularity model alters the intensity and phase spectra of the $1^{++}0^+ f_0(980)\pi P$ wave compared to parametrizing the $a_1(1420)$ with a Breit–Wigner amplitude. Section 9.2 investigates the sensitivity for distinguishing between the two amplitudes.

9.1 Comparison of Breit–Wigner vs. Triangle Singularity Amplitude

We were provided a lookup table with the real and imaginary parts of the bare triangle singularity amplitude evaluated at discrete mass values on a regular grid between $1.0\,\mathrm{GeV}/c^2$ and $2.1\,\mathrm{GeV}/c^2$ by the authors of ref. [79]. When evaluating the amplitude at an arbitrary $m_{3\pi}$ value, the real and imaginary parts are interpolated separately using linear interpolation. As the lookup table only provides the bare triangle singularity amplitude we need to multiply it with the $a_1(1260)$ amplitude[2] to obtain the physical

[2]The same $a_1(1260)$ amplitude, with identical parameters, enters both as the $a_1(1260)$ contribution in the fit and as the factor multiplying the bare triangle singularity amplitude.

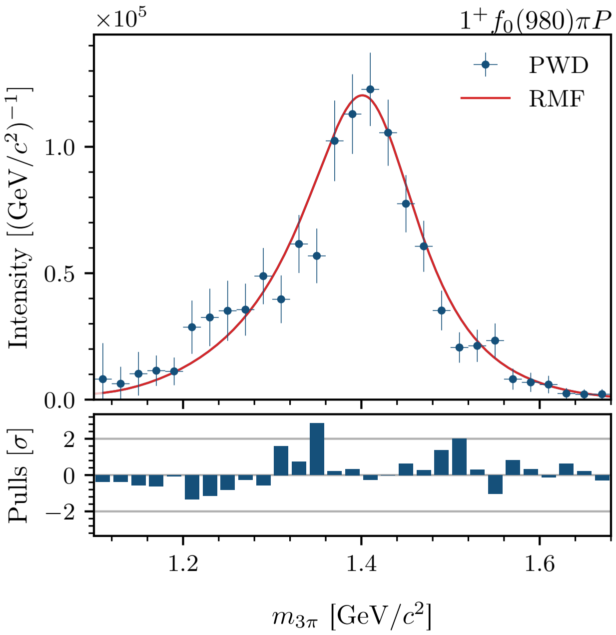

Figure 9.3: Similar to fig. 7.1. The PWD was performed on a data sample where the $1^+ f_0(980)\pi P$ wave was modeled with the triangle singularity. All other waves are modeled as described in chapter 7. In the RMF the same model as described in section 7.4 was used.

triangle singularity amplitude, which we will refer to as the triangle singularity in the following. In order to quantify the sensitivity to the difference between the triangle singularity and a Breit–Wigner resonance, we first investigated the shapes of both a Breit–Wigner and triangle singularity amplitude in our decays. To this end, we generated data with the process described in chapter 7, replacing the Breit–Wigner amplitude for the $a_1(1420)$ with the triangle singularity amplitude. The couplings listed in table 7.1 and the Breit–Wigner parameters for the resonances listed in table 7.2 were left unchanged. We applied the standard PWD to these data and subsequently performed an RMF using the PWD fit results (see fig. 9.3). In this RMF the same RMF model as in section 7.4 was used, i.e., a Breit–Wigner amplitude also for the $a_1(1420)$ signal. The parameters extracted for the $a_1(1420)$ Breit–Wigner component, modeling the triangle singularity in the input model, yielded a mass of $m_{a_1(1420)} = (1425.8 \pm 2.3)\,\mathrm{MeV}/c^2$ and a width of $\Gamma_{a_1(1420)} = (169 \pm 6)\,\mathrm{MeV}/c^2$. These parameters were then used to formulate an input model using a Breit–Wigner amplitude for the $a_1(1420)$ with parameters matching those extracted from the triangle singularity generated data. This Breit–Wigner amplitude will be called the $\mathrm{BW_{TS}}$.

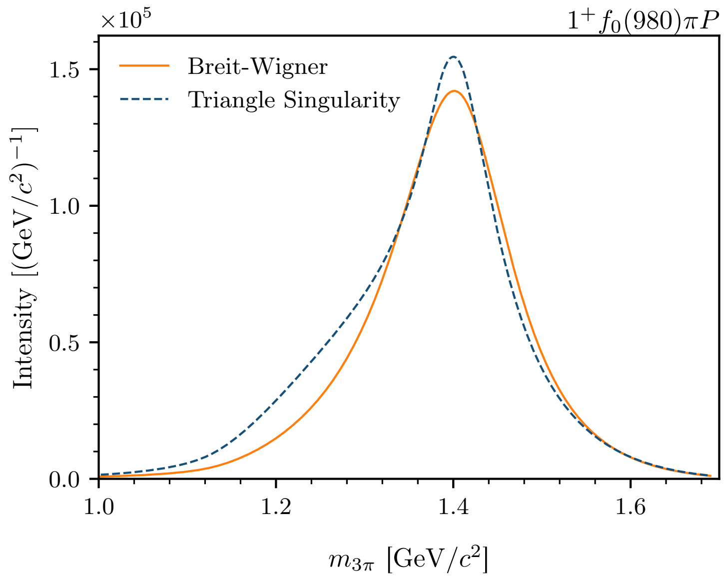

Figure 9.4: Intensity spectrum for Breit–Wigner (solid orange) and triangle singularity (dashed blue) model curves. Both model curves were normalized to account for the same amount of signal events.

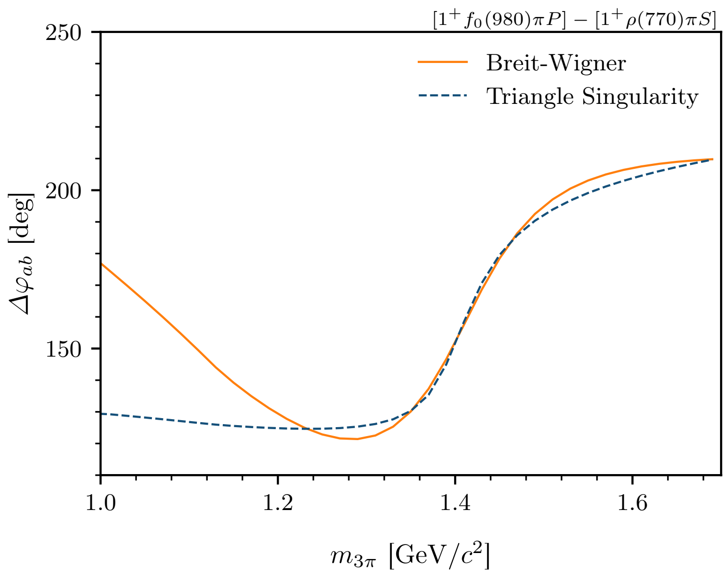

Figure 9.5: Phase spectrum for Breit–Wigner (solid orange) and triangle singularity (dashed blue) model curves. As the triangle singularity and Breit–Wigner amplitudes have different phases, the phase of the triangle singularity amplitude was shifted up by about 70°.

Figure 9.4 compares the intensities of the triangle singularity amplitude (blue dashed line) and the $\mathrm{BW_{TS}}$ amplitude (solid orange line). Both curves exhibit a peak at the same $m_{3\pi}$ position, as expected, since the Breit–Wigner parameters were obtained by fitting to the triangle singularity spectrum. The intensity of the triangle singularity exhibits a larger tail towards lower $m_{3\pi}$ values. Above about $1.4\,\mathrm{GeV}/c^2$, the intensity of both curves exhibits very similar shape and magnitude. The triangle singularity and Breit–Wigner amplitudes exhibit similar phase motions for $m_{3\pi} \gtrapprox 1.2\,\mathrm{GeV}/c^2$ (see fig. 9.5). However, the total phase motion for $1.2\,\mathrm{GeV}/c^2 < m_{3\pi} < 1.7\,\mathrm{GeV}/c^2$ of the triangle singularity is about $10\,°$ smaller than that of the Breit–Wigner amplitude. Towards lower $m_{3\pi}$ values, the phase of the triangle singularity stays approximately constant with respect to $m_{3\pi}$, while the phase of the Breit–Wigner amplitude rises with respect to $m_{3\pi}$. However, the difference in phase behavior at low $m_{3\pi}$ will probably not allow us to significantly distinguish between the two models, as different partial waves are indistinguishable in the low $m_{3\pi}$ region. This is the reason that we set up the thresholds described in table 7.3, which result from a study performed in ref. [25].

Overall, both amplitudes yield similar $m_{3\pi}$ dependence for the $1^+ f_0(980)\pi P$ wave. This indicates that distinguishing between the two models is challenging. The most reliable approach to distinguishing between the two models will therefore be to perform several RMFs on the resulting spectra and compare χ^2-values, in order to draw a definitive conclusion on the origin of the observed signal.

9.2 Sensitivity Studies on Triangle Singularity

As discussed in the previous section, the triangle singularity and Breit–Wigner amplitudes yield similar intensity and phase spectra, differing mainly in the low-$m_{3\pi}$ tail and the total phase motion. To investigate how well we expect to distinguish a genuine resonance from a triangle singularity as the origin of the $a_1(1420)$ signal, we perform several sensitivity studies. To this end, we generate several data samples with varying parametrizations of the $1^+ f_0(980)\pi P$ wave. For each sample, we perform a PWD fit followed by two RMFs: one parametrizing the $1^+ f_0(980)\pi P$ wave with a triangle singularity amplitude, the other with a Breit–Wigner amplitude. We then compare the two fits by their χ^2-values (see eq. (6.7)). The two RMFs differ by two free parameters, so their χ^2-values are not defined on exactly the same number of degrees of freedom. Since this difference is negligible compared to the roughly 500 degrees of freedom, we compare the two χ^2-values values directly. We use the χ^2-values as a qualitative measure of goodness-of-fit, taking a large difference between the two RMFs as an indication that the models can be distinguished and a small difference as an indication that they cannot. Section 9.2.1 investigates three baseline samples:

1. We assume a genuine resonance, i.e. a Breit–Wigner amplitude, with the $a_1(1420)$ resonance parameters obtained by COMPASS [20].

2. We assume a triangle singularity as the origin of the signal.

3. We assume a genuine resonance as the origin of the signal, with the parameters of the matched Breit–Wigner amplitude ($\mathrm{BW_{TS}}$).

Section 9.2.2 investigates how well the two amplitudes can be distinguished if the signal is generated by a Breit–Wigner amplitude whose mass is offset from the value expected for a triangle singularity. Section 9.2.3 investigates the analogous case in which the mass is fixed at the value expected for a triangle singularity but the width is shifted. Lastly, section 9.2.4 investigates how well a triangle singularity can be distinguished from a Breit–Wigner amplitude if the signal is generated by a triangle singularity in which the width of the $a_1(1260)$ is varied. Since the high-$m_{3\pi}$ tail of the $a_1(1260)$ generates the triangle singularity, this may also affect the discriminating power. Because the data samples used for these studies contain fewer events than we expect in $1\,\mathrm{ab}^{-1}$ of real data, by about a factor of 17, we repeat all studies with the intensity of the $1^+ f_0(980)\pi P$ wave scaled up by a factor of ten[3], to assess the impact of an increased signal yield on the discriminating power of the RMF. In the following we will show only selected results, the full RMF results can be found in appendix B.

9.2.1 Sensitivity in Base Models

As mentioned in section 9.2, this section concentrates on three baseline parametrizations of the $1^+ f_0(980)\pi P$ wave, each studied at the nominal and ten-fold signal intensity, as summarized in table 9.1. Figure 9.6 shows the intensity spectrum obtained for the *BW of TS 10x* sample, i.e. the sample where the $\mathrm{BW_{TS}}$ was used to parametrize the $a_1(1420)$ and the $1^+ f_0(980)\pi P$ wave was artificially increased to its ten-fold intensity. Both the solid and dashed red curves correspond to Breit–Wigner amplitudes and are therefore expected to exhibit similar shapes, with any deviation reflecting the intrinsic analysis bias of the RMF discussed in chapter 8. We observe that the Breit–Wigner RMF curve is shifted towards higher $m_{3\pi}$ values relative to the input model, consistent with this intrinsic analysis bias. The green triangle singularity curve shows a very similar shape to that of the Breit–Wigner input model, with a slightly larger tail towards lower $m_{3\pi}$ values. The χ^2 values of both RMF models are very similar, as both parametrizations yield

[3]We cannot generate a sample 17 times larger, so instead of increasing the full data set we scale the intensity of the $1^+ f_0(980)\pi P$ wave. This does not reproduce the reduced statistical uncertainties of a larger data set in all waves. It emulates only an increased signal yield in the wave of interest, which is the quantity that drives the discriminating power between the triangle singularity and Breit–Wigner amplitudes. We choose a round factor of ten.

Table 9.1: χ^2-values for RMF studies of the $1^+ f_0(980)\pi P$ wave with varying input-model and RMF parametrizations. The *Data Sample* column identifies the parametrization used to generate the input data: *BW COMPASS* uses a Breit–Wigner amplitude with the resonance parameters from COMPASS [20]; *TS* uses the triangle singularity amplitude; *BW of TS* uses the $\mathrm{BW_{TS}}$ amplitude. The suffix *10x* denotes samples in which the $1^+ f_0(980)\pi P$ wave intensity is scaled up by a factor of ten. The *RMF Model* column identifies the amplitude used in the RMF: *BW* for a Breit–Wigner amplitude and *TS* for the triangle singularity.

Data Sample	RMF Model	χ^2
BW COMPASS	BW	2324
BW COMPASS	TS	2568
BW COMPASS 10x	BW	2829
BW COMPASS 10x	TS	3700
TS	BW	2561
TS	TS	2468
TS 10x	BW	2850
TS 10x	TS	2665
BW of TS	BW	2370
BW of TS	TS	2404
BW of TS 10x	BW	2355
BW of TS 10x	TS	2686

comparable shapes for this wave. As expected, the RMF whose parametrization matches the input model yields smaller χ^2 values than the RMF using the triangle singularity. The Breit–Wigner resonance parameters of the remaining waves agree between the two RMF models within their statistical uncertainties, indicating that the differences in χ^2 originate from the shape difference of the $1^+ f_0(980)\pi P$ wave parametrization. Due to the lower intensity in the $1^+ f_0(980)\pi P$ wave in the *BW of TS* sample and consequently the lower statistical precision of the PWD fit results, the RMFs in this sample show slightly smaller discriminating power. The *TS* and *TS 10x* samples exhibit similar discriminating power to the *BW of TS* samples, owing to the similar shapes of the Breit–Wigner and triangle singularity amplitudes.

The intensity spectrum of the *BW COMPASS 10x* sample is shown in fig. 9.7. The shapes of the input model and the RMF using the Breit–Wigner amplitude are very similar, apart from the intrinsic analysis bias discussed in chapter 8. The RMF yielded a Breit–Wigner mass of $m_{a_1(1420)} = (1412.2 \pm 1.0)\,\mathrm{MeV}/c^2$ and a width of $\Gamma_{a_1(1420)} = (162 \pm 2)\,\mathrm{MeV}/c^2$, which are close to the input values shown in table 7.2. These small deviations ($\mathcal{O}(10\,\mathrm{MeV}/c^2)$) are not distinguishable in the intensity spectrum.

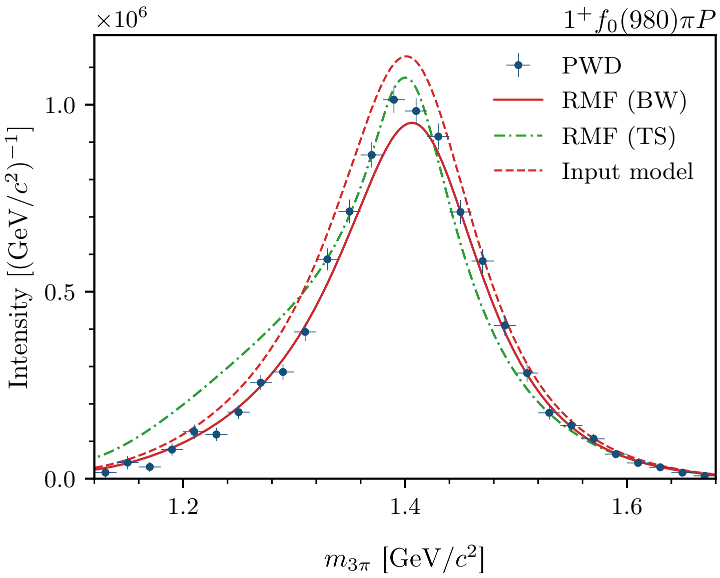

Figure 9.6: Intensity spectrum of the $1^+ f_0(980)\pi P$ wave as a function of the invariant mass of the 3π system. The blue data points correspond to the intensities obtained from the PWD. The solid red curve corresponds to the RMF result in which a Breit–Wigner amplitude was used to model the wave. The dash-dotted green curve corresponds to the RMF result in which the triangle singularity amplitude was used. The dashed red curve shows the intensity of the input model, for the *BW of TS 10x* sample.

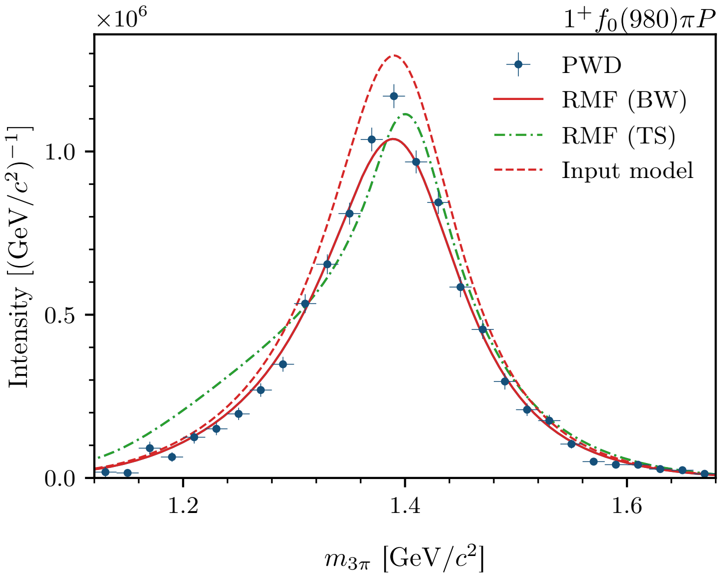

Figure 9.7: Same as fig. 9.6, but using the *BW COMPASS 10x* sample.

The dash-dotted green curve of the triangle singularity fit, however, shows a peak position deviating from both the input model and the PWD fit results. Towards lower $m_{3\pi}$, the larger tail of the triangle singularity creates a higher intensity than that of the input model. In this region, the shape clearly deviates from the input. The shape of the triangle singularity is fixed by construction, and its overall normalization is controlled only by the coupling parameter in the RMF. Only the $a_1(1260)$ lineshape can alter the shape of the triangle singularity amplitude. This amplitude therefore has limited flexibility and cannot adapt to the shape of the input model. This is reflected in the χ^2-values: the RMF using the triangle singularity yields a χ^2-value 25 % higher than the RMF using a Breit–Wigner amplitude. This larger mismatch compared to the *BW of TS* samples arises because the COMPASS Breit–Wigner parameters place the peak position by about 10 MeV/c^2 away from that of the triangle singularity, whereas the *BW of TS* parametrization was constructed to match it. If the signal were generated by a genuine resonance with parameters close to those as COMPASS extracted for the $a_1(1420)$ signal, we would potentially be able to conclude that the triangle singularity contributes only lightly to the signal.

9.2.2 Sensitivity to a Mass Offset of the $a_1(1420)$

In section 9.2.1 we have observed, that if a genuine resonance with its mass shifted away from the $\mathrm{BW_{TS}}$ resonance parameters were to generate the observed signal, then we might be able to distinguish between the generation models for the signal. To investigate this further, we generated two data samples by shifting the Breit–Wigner mass of the $a_1(1420)$ up and down by 40 MeV/c^2 from the baseline value $m_{a_1(1420)} = (1425.8 \pm 2.3)$ MeV/c^2 of the $\mathrm{BW_{TS}}$ amplitude. The corresponding χ^2-values are listed in table 9.2.

The intensity spectrum of the *Mass Up* sample is shown in fig. 9.8, which is representative of all four studied cases. The Breit–Wigner RMF provides a good description of the PWD fit results. The fitted Breit–Wigner parameters exhibit slightly higher mass and width than the input model values, consistent with the intrinsic analysis bias discussed in chapter 8. The dash-dotted green curve of the triangle singularity RMF, however, shows clear deviations from the input model and PWD fit results, with the peak position shifted by approximately 20 MeV/c^2 relative to the input model. As discussed in section 9.2.1, the peak position of the triangle singularity is fixed by construction and cannot adapt to the shifted input. This is reflected in the goodness-of-fit characteristics: the χ^2 is smaller for the Breit–Wigner RMF than for the triangle singularity RMF in all four cases (see table 9.2). The ten-fold intensity samples yields considerably larger differences in χ^2 between the two RMF models than the nominal samples, demonstrating that the discriminating power improves substantially with increased signal yield. Therefore, if

Table 9.2: Same columns as in table 9.1. The *Data Sample* labels refer to the Breit–Wigner mass of the $a_1(1420)$ used to generate the input data: *Mass Up* and *Mass Down* denote samples in which the baseline Breit–Wigner mass is shifted up and down by $40\,\mathrm{MeV}/c^2$, respectively. The suffix *10x* is as defined in table 9.1.

Data Sample	RMF Model	χ^2
Mass Up	BW	2910
Mass Up	TS	3270
Mass Up 10x	BW	2827
Mass Up 10x	TS	4424
Mass Down	BW	2839
Mass Down	TS	2964
Mass Down 10x	BW	2943
Mass Down 10x	TS	5079

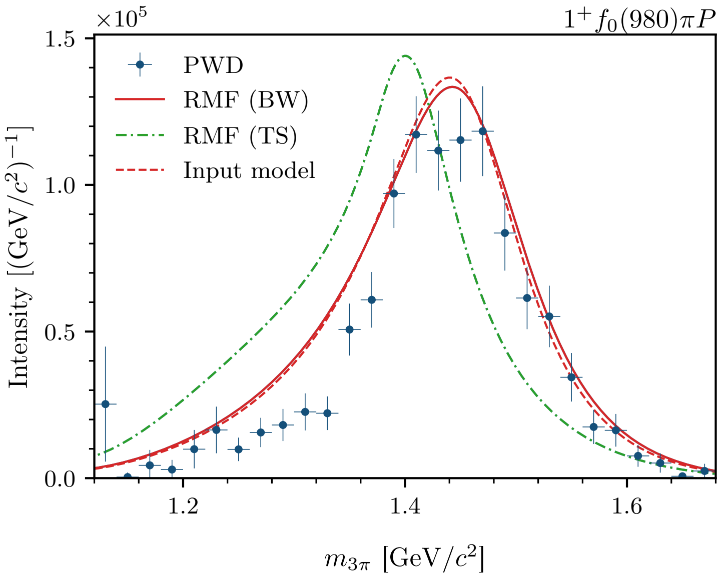

Figure 9.8: Same as fig. 9.6, but using the *Mass Up* sample.

the $a_1(1420)$ signal were to be produced by a genuine resonance whose mass deviates from that of the triangle singularity, then we will probably be able to conclude a small contribution of the triangle singularity to the signal.

Table 9.3: Same columns as in table 9.1. The *Data Sample* labels refer to the Breit–Wigner width of the $a_1(1420)$ used to generate the input data: *Width Up* and *Width Down* denote samples in which the baseline Breit–Wigner width is shifted up and down by $40\,\mathrm{MeV}/c^2$, respectively. The suffix *10x* is as defined in table 9.1.

Data Sample	RMF Model	χ^2
Width Up	BW	2561
Width Up	TS	2612
Width Up 10x	BW	2540
Width Up 10x	TS	3545
Width Down	BW	2622
Width Down	TS	2891
Width Down 10x	BW	3561
Width Down 10x	TS	4559

9.2.3 Sensitivity to a Width Offset of the $a_1(1420)$

In this section we investigate the consequences if the $a_1(1420)$ signal were generated by a genuine resonance, whose width deviates from that expected from the triangle singularity. We shifted the Breit–Wigner width of the $a_1(1420)$ up and down by $40\,\mathrm{MeV}/c^2$ from the baseline value $\Gamma_{a_1(1420)} = (169 \pm 6)\,\mathrm{MeV}/c^2$ of the $\mathrm{BW_{TS}}$ amplitude. The corresponding χ^2-values are listed in table 9.3.

The intensity spectrum of the *Width Up* sample is shown in fig. 9.9. The intrinsic analysis bias discussed in chapter 8 is again observed. The Breit–Wigner RMF provides a good description of the PWD fit results, consistent with previous results. Due to the larger width of the generating Breit–Wigner amplitude, the low-$m_{3\pi}$ tail of the triangle singularity no longer stands out relative to the input model, as the wider Breit–Wigner amplitude also exhibits a more pronounced low-mass tail. Therefore, the two amplitudes are more similar in shape. As a result, the differences in χ^2 between the two RMF models are small, since the triangle singularity now provides a comparable description of the wave. At the one-fold intensity, discrimination between the two models would therefore be challenging, as the χ^2-values are too close. The ten-fold intensity sample, however, shows larger differences in χ^2-values due to the higher statistical precision of the PWD fit results, allowing the two models to be discriminated.

The *Width Down 10x* sample is shown in fig. 9.10. The Breit–Wigner RMF describes the wave well within the intrinsic analysis biases discussed in chapter 8. The triangle singularity curve, however, appears to exhibit a significant tail towards low $m_{3\pi}$. This is not a change in the triangle singularity shape itself, which is fixed by construction. It is

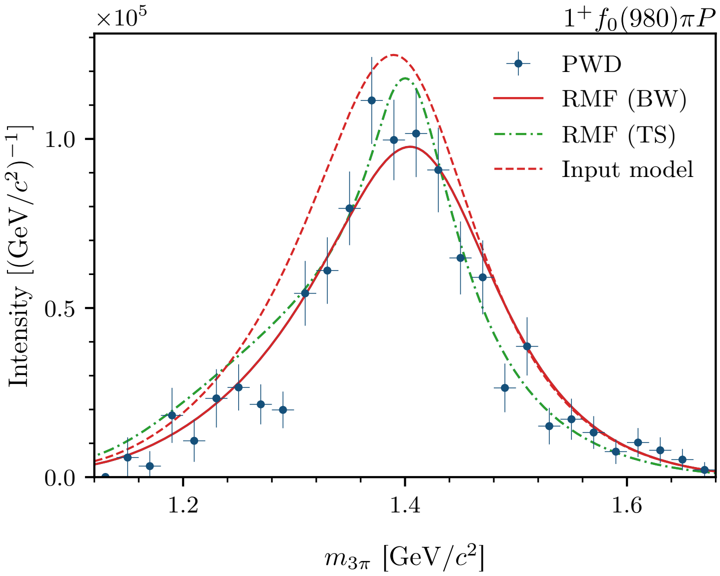

Figure 9.9: Same as fig. 9.6, but using the *Width Up* sample.

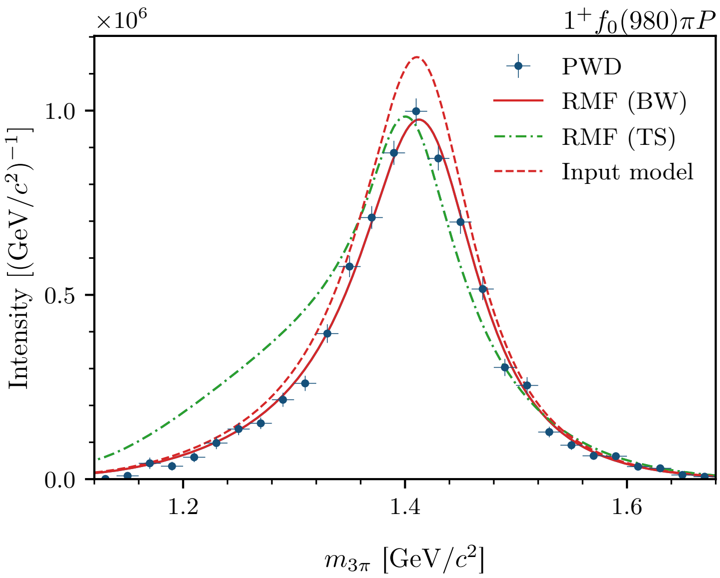

Figure 9.10: Same as fig. 9.6, but using the *Width Down 10x* sample.

Table 9.4: Same columns as in table 9.1. The *Data Sample* labels refer to the Breit–Wigner width of the $a_1(1260)$ used to generate the input data: *a_1(1260) Width Up* and *a_1(1260) Width Down* denote samples in which the baseline Breit–Wigner width is shifted up to 600 MeV/c^2 and down to 250 MeV/c^2, respectively. The suffix *10x* is as defined in table 9.1.

Data Sample	RMF Model	χ^2
a_1(1260) Width Up	BW	2321
a_1(1260) Width Up	TS	2273
a_1(1260) Width Up 10x	BW	2218
a_1(1260) Width Up 10x	TS	2176
a_1(1260) Width Down	BW	2919
a_1(1260) Width Down	TS	2858
a_1(1260) Width Down 10x	BW	3492
a_1(1260) Width Down 10x	TS	3232

rather a consequence of the narrower generating Breit–Wigner amplitude reducing the intensity of the PWD fit results at low $m_{3\pi}$, making the fixed triangle singularity tail appear relatively larger by comparison. This results in a larger discrepancy between the PWD fit results and the triangle singularity curve. Interestingly, this discrepancy is not strongly reflected in the χ^2-values: the difference in χ^2 between the two RMF models is nearly identical to that observed in the *Width Up 10x* sample. As the χ^2 values also show statistical fluctuations, we attribute this effect to statistical fluctuations in the data generation process. The *Width Down* sample behaves as expected, with the difference in χ^2-values is slightly larger than that of the *Width Up* sample. Overall, if the signal were generated by a genuine resonance with a larger width than that of the triangle singularity, we might be able to conclude a small contribution of the triangle singularity only at the higher signal intensities expected in the full 1 ab^{-1} data sample.

9.2.4 Sensitivity Based on $a_1(1260)$ Width

In this last section we assume that the signal were generated by a triangle singularity process. As the amplitude of the triangle singularity process is based on the high-mass tail of the $a_1(1260)$, we investigate the effect of different widths on the differentiation power between a genuine resonance and a triangle singularity. This is motivated by the large range the PDG quotes for the width of the $a_1(1260)$ of 250 to 600 MeV/c^2 [10], which shows that the resonance parameters of this resonance are not well known. Therefore, we perform studies where the $a_1(1260)$ is generated with a width of 250 MeV/c^2 and 600 MeV/c^2. All performed RMFs and their χ^2-values are

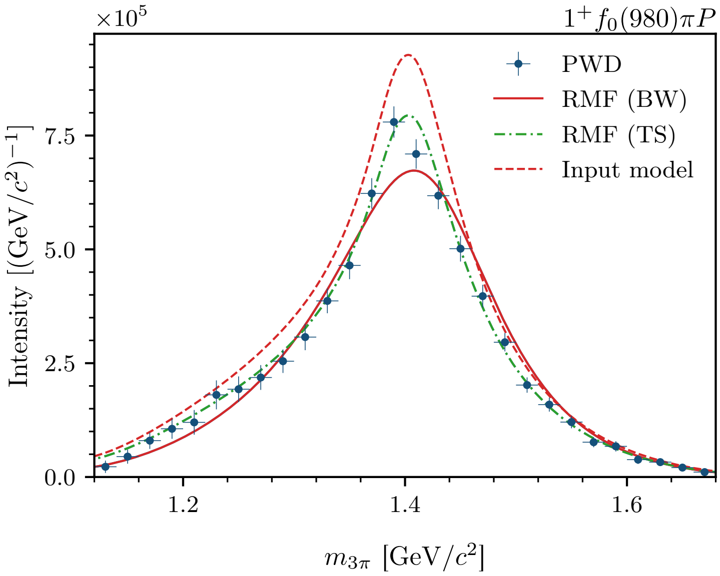

Figure 9.11: Same as fig. 9.6, but using the $a_1(1260)$ *Width Up 10x* sample.

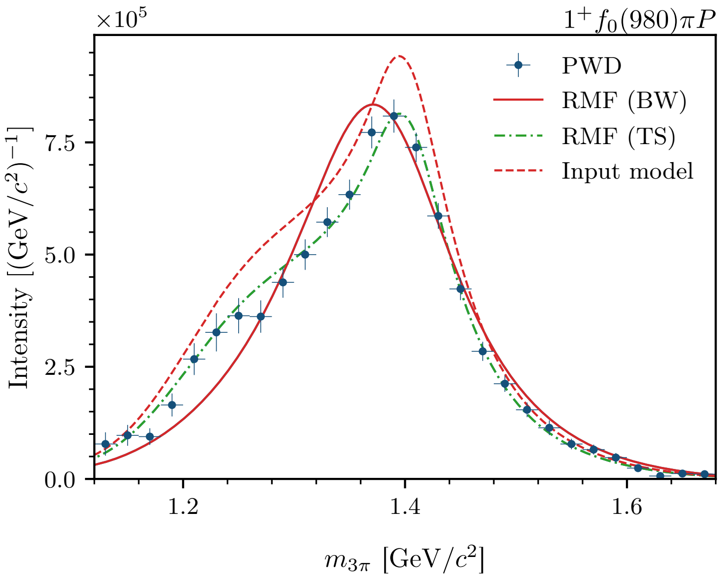

Figure 9.12: Same as fig. 9.6, but using the $a_1(1260)$ *Width Down 10x* sample.

listed in table 9.4.

In figs. 9.11 and 9.12, a difference between the dashed red input model curves of the $a_1(1260)$ *Width Up 10x* and $a_1(1260)$ *Width Down 10x* studies is apparent. The

a_1(1260) Width Down 10x study exhibits a shoulder around $m_{3\pi} = 1.3\,\mathrm{GeV}/c^2$, while the other sample does not exhibit this structure. This is due to the mathematical construction of the triangle singularity amplitude: the amplitude of the bare triangle singularity is multiplied by the amplitude of the $a_1(1260)$. When a narrower $a_1(1260)$ is used, the resonance exhibits a more distinct peak at about $m_{3\pi} = 1.3\,\mathrm{GeV}/c^2$, resulting in the shoulder visible in fig. 9.12. The wider $a_1(1260)$ does not produce this additional shoulder and instead creates a larger tail towards low $m_{3\pi}$.

The Breit–Wigner RMF can adapt well to the resulting shape of the triangle singularity amplitude in the *a_1(1260) Width Up 10x* sample, as this amplitude closely resembles a Breit–Wigner lineshape. In the *a_1(1260) Width Down 10x* sample, the Breit–Wigner amplitude cannot adapt as well, since it cannot reproduce the shoulder visible in fig. 9.12. This effect is also reflected in the χ^2-values listed in table 9.4. The difference in χ^2 between the Breit–Wigner and triangle singularity RMFs is small in the cases where the wider $a_1(1260)$ is used. In the cases with a narrower $a_1(1260)$, the difference between the χ^2-values is larger, as can already be anticipated from the fit shapes shown in figs. 9.11 and 9.12. Overall, if the $a_1(1420)$ signal were to be generated by a triangle singularity, we might be able to differentiate between the two models only if the $a_1(1260)$ would have a width towards the lower end in the range listed by the PDG, as the flexibility of the Breit–Wigner amplitude does not allow a differentiation otherwise.

10 K-Matrix

The most common parameterization for resonances is the Breit–Wigner amplitude (see eq. (4.29)). This amplitude parametrizes well the peaks that appear in our intensity spectra, as well as the observed phase motion. The Breit–Wigner amplitude is an approximation that holds for narrow, isolated resonances whose mass lies well away from any coupled channel threshold. A prominent example of where this approximation breaks down is shown in fig. 10.1. The $M(\pi^+\pi^-)$ spectrum exhibits a large and distinct peak at about 1 GeV. In the $M(K^+K^-)$ spectrum a peak at the same mass can be observed, but with much less intensity. Both peaks correspond to decays of the $f_0(980)$ resonance. The $M(\pi^+\pi^-)$ spectrum exhibits a sharp drop-off at the K^+K^- mass threshold, while the intensity in the $M(K^+K^-)$ spectrum has a sharp increase. This indicates that the $f_0(980)$ couples much more strongly to the K^+K^- decay channel than to that of the $\pi^+\pi^-$ channel. As the peaks in both spectra originate from the same resonance, both should be described by one set of resonance parameters. When these intensity spectra

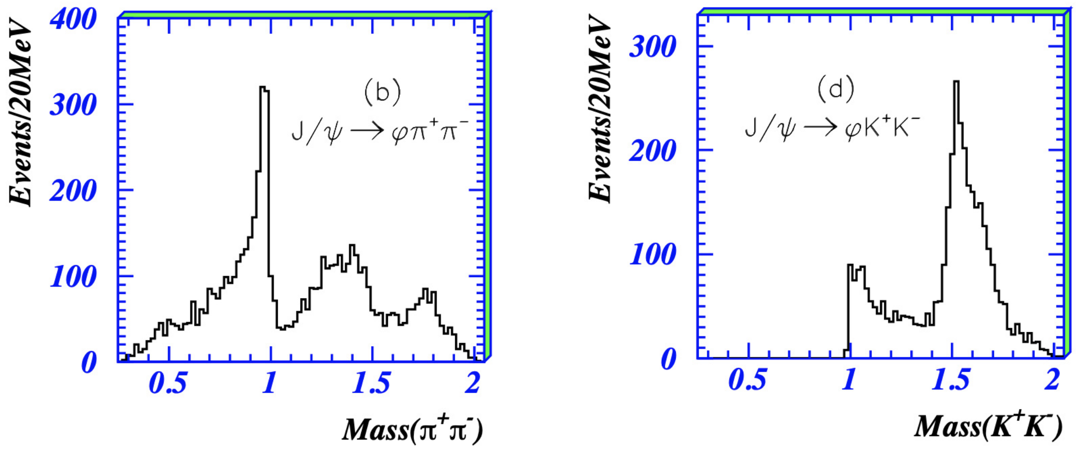

Figure 10.1: Invariant mass spectra of the system recoiling against a Φ (labeled φ) candidate in J/ψ decays. (b) $\pi^+\pi^-$ invariant mass in $J/\psi \to K^+K^-\pi^+\pi^-$ events with $M(K^+K^-)$ within $\pm 15\,\mathrm{MeV/c^2}$ of the Φ mass. (d) K^+K^- invariant mass of the second K^+K^- pair in $J/\psi \to K^+K^-K^+K^-$ events with $M(K^+K^-)$ of the first K^+K^- pair within $\pm 15\,\mathrm{MeV/c^2}$ of the Φ mass. Figure adapted from the BES Collaboration [80].

were to be fitted with a Breit–Wigner resonance, the extracted Breit–Wigner width parameters would yield different values for the different decay channels, indicating a wrong description of the $f_0(980)$ resonance. Therefore, we need to extract resonance parameters independent of the chosen parameterization.

One possible set of such resonance parameters is the pole position of the resonance. Our observables are all measured on the real $m_{3\pi}$ invariant mass axis. This real invariant mass axis can be extended into the complex squared energy plane s, where $\mathrm{Re}\, s = m_{3\pi}^2$. Resonances appear as poles s_R of the scattering matrix S, that relates the initial and final states of a scattering process, in the s-plane [10]. The pole mass M_R and pole width Γ_R can be extracted from the pole position as follows:

$$\sqrt{s_R} = M_R - i\frac{\Gamma_R}{2}. \tag{10.1}$$

Extracting the pole from a Breit–Wigner amplitude is possible in principle. However, for multichannel resonances the extracted pole position depends on which decay channel is fitted, as the $f_0(980)$ example demonstrates. A formalism that correctly accounts for the coupled channel effects and is capable of extracting the correct pole positions of the resonances is the K-matrix formalism.

In the $\tau^- \to \pi^+\pi^-\pi^-\nu_\tau$ decays, the resonances contributing to these decays couple to multiple isobar channels. So far we have parametrized these resonances by a sum-of-Breit–Wigner amplitudes, which is a good approximation of the resonant structure. However, a naive sum of Breit–Wigner amplitudes does not, in general, yield a unitary amplitude. As we want to perform high precision measurements of the resonant structure of our decays, we want to explore the possibility of using a K-matrix Ansatz to describe our partial waves. This would allow us to model the coupled channel effects, as well as non-narrow and non-isolated resonances correctly, while guaranteeing unitarity of the amplitude by construction. In section 10.1 an educational introduction to the K-matrix formalism is provided. This section closely follows ref. [19]. Section 10.2 discusses simple examples of the K-matrix formalism and validates our approach. Lastly in section 10.3 we discuss RMFs performed with the K-matrix formalism.

10.1 K-Matrix Formalism

In order to obtain a unitary expression for the scattering amplitudes we start with the scattering matrix S[1], that can be expressed by two parts:

$$S = I + 2iT, \tag{10.2}$$

[1] Note that S and all subsequently defined operators are functions of the squared invariant mass s. This dependence is suppressed in the notation for brevity.

where I is the identity operator and describes that the initial and final state do not interact at all. The transition operator T entails all information about the scattering process. The factors 2 and i have been introduced for convenience. Using the unitarity of the S matrix, i.e.,

$$SS^\dagger = S^\dagger S = I, \tag{10.3}$$

yields the following constraint on T:

$$(T^{-1} + iI)^\dagger = T^{-1} + iI. \tag{10.4}$$

The K operator is then defined as:

$$K^{-1} = T^{-1} + iI. \tag{10.5}$$

Note that from eq. (10.4) it follows that the K operator must be hermitian. Considering that the S matrix is only unitary in the open channels, the K operator is hermitian on the real axis.

10.1.1 K-Matrix in P-Vector Approach

The K-matrix approach considers only s-channel resonances that are observed in two-body scattering events. The formalism can be generalized to also describe the formation of resonances in more complex reactions, like the decays studied in this work. Therefore, we implemented Aitchisons P-vector approach from ref. [81]. This approach also models the production of resonances and is thus ideal for uses in isobar model amplitude analyses. Note that we will only introduce the Lorentz invariant form of the formalism (see ref. [19] for details). We need several components to parametrize the invariant amplitudes for resonances α to decay into channels i, as defined in the following.

First, we need the invariant $\hat{K}$ matrix. That is defined by a sum over poles α:

$$\hat{K}_{ij}(s) = \sum_\alpha \frac{g_{\alpha i}(s) g_{\alpha j}(s)}{(m_\alpha^2 - s)\sqrt{\rho_i(s)\rho_j(s)}} + P_{ij}(s). \tag{10.6}$$

The two factors ρ_i, ρ_j correspond to the two body phase space in decay channel i and is defined by:

$$\rho_i(s) = 2\sqrt{\frac{q^2}{s}} = \frac{\sqrt{(s - (m_1 + m_2)^2)(s - (m_1 - m_2)^2)}}{s}, \tag{10.7}$$

where m_1 and m_2 are the masses of the final-state particles of channel i. q^2 is the two body breakup momentum (see eq. (4.2)). The $g_{\alpha i}(s)$ factors are given by:

$$g_{\alpha i}(s) = g^0_{\alpha i} B^L_{\alpha i}(q^2(s), q^2(m_\alpha^2))\sqrt{\rho_i}. \tag{10.8}$$

$g^0_{\alpha i}$ corresponds to a real valued constant decay coupling, while $B^L_{\alpha i}(q^2(s), q^2(m^2_\alpha))$ denotes a ratio of barrier factors $b^L(q^2_i(s))$ (see eq. (4.3)):

$$B^L_{\alpha i}(q^2(s), q^2(m^2_\alpha)) = \frac{b^L(q^2_i(s))}{b^L(q^2_i(m^2_\alpha))}. \tag{10.9}$$

In the RMF, the decay couplings $g^0_{\alpha i}$ are fit parameters. A polynomial $P_{ij}(s)$ may be added to each K_{ij}-matrix element without destroying unitarity, provided its coefficients are real. This accounts for slowly varying contributions to the scattering amplitude not captured by the pole terms. For simplicity, we set the polynomials to have the same coefficients for all i, j.

Second, we need the invariant production vector. That is also given by a sum over the same poles α:

$$\hat{P}_i = \sum_\alpha \frac{\beta^0_\alpha g_{\alpha i}(s)}{(m^2_\alpha - s)\sqrt{\rho_i(s)}} + d_i(s). \tag{10.10}$$

The complex valued production couplings β^0_α of $\hat{P}_i$ are independent of the decay couplings in the $\hat{K}$-matrix. In the RMF the β^0_α factors are free fit parameters. Like for the $\hat{K}$-matrix, a polynomial $d_i(s)$ can also be added to each element of the production vector. They model direct 3π production or Deck-like reactions [82–84]. In general the d_i factors are complex valued. For simplicity, we have chosen to add the same polynomial to every $\hat{P}$-vector element, and we constrain the d_i factors to be real valued.

With these two ingredients we can now write down the $\hat{F}$-vector, where the i-th element of the vector corresponds to the invariant amplitude in channel i.

$$\hat{F}(s) = (\underbrace{I - i\hat{K}\hat{\rho}}_{\equiv \hat{A}})^{-1}\hat{P} = \hat{A}^{-1}\hat{P} \tag{10.11}$$

Here, $\hat{\rho}$ corresponds to the diagonal phase-space matrix, where $\hat{\rho}_{ii} = \rho_i(s)$. Together eqs. (10.6) to (10.11) define the K-matrix parameterization used in this work. For brevity, we will henceforth refer to this framework as the **K-matrix parametrization**, even when discussion specifically concerns the production vector $\hat{P}$ or the amplitude $\hat{F}$.

10.1.2 K-Matrix in RMF

In section 4.7 we have introduced several dynamic amplitudes that we use in the RMF. In the current form the $\hat{F}$ vector does not match our formalism of dynamic amplitudes, and we therefore have to undertake two steps to derive the dynamic amplitude $\mathcal{D}_i(s)$, that matches our convention for dynamic amplitudes, from $\hat{F}_i$. The first is related to the barrier factor $b^L(q^2_i(s))$ defined in section 4.2. In the RMF formalism we model the

Table 10.1: Number of free fit parameters for a sum-of-Breit–Wigner dynamic amplitudes and a K-matrix dynamic amplitude, for varying numbers of channels and poles. The first column shows the number of channels and the second column the number of poles, i.e., resonances. The next four columns show the free parameters of a sum-of-Breit–Wigner dynamic amplitudes: the number of complex coupling parameters $\mathcal{C}$, where each complex-valued coupling contributes two free parameters; the number of free Breit–Wigner mass m_0 parameters; the number of free Breit–Wigner width Γ_0 parameters; and their sum Σ. The last four columns show the free parameters of a K-matrix dynamic amplitude: the number of complex production coupling parameters β_α contributing two free parameters each; the number of free decay couplings $g_{\alpha i}$; the number of free bare mass parameters m_0; and their sum Σ.

# Channels	# Poles	Breit–Wigner				K-matrix			
		# $\mathcal{C}$	# m_0	# Γ_0	Σ	# β_α	# $g_{\alpha i}$	# m_0	Σ
1	1	2	1	1	4	2	1	1	4
1	2	4	2	2	8	4	2	2	8
2	1	4	1	1	6	2	2	1	5
2	2	8	2	2	12	4	4	2	10

partial wave amplitudes as a product of several factors (see eq. (6.1)). One of them, the wave-normalization integral $\mathcal{R}_a(m_{3\pi})$ (see eq. (4.18)) contains the barrier factor $b^L\left(q^2(m_{3\pi}^2; m_{\pi^+\pi^-}, m_{\pi^-})\right)$. The $\hat{F}$ vector already contains this same factor entering the production vector in eq. (10.10) via $g_{\alpha,i}$ in eq. (10.8). Therefore, we define the reduced invariant amplitude vector

$$\mathcal{D}_i(s) = \frac{\hat{F}_i(s)}{b^L(q_i^2(s))}. \tag{10.12}$$

This factorizes b^L from the $\hat{F}_i$ vector. In section 10.3.1 this approach will be validated.

The second step concerns the RMF couplings amplitude ${}^k\mathcal{C}(m_{3\pi})$ in eq. (6.1), that encode the coupling of a resonance to a partial wave. Since the production couplings β_α^0 have the same functionality, multiplying by an additional RMF coupling amplitude ${}^k\mathcal{C}$ leads to an overparameterization. The RMF can arbitrarily change the real and imaginary parts of one coupling when it changes β_α^0 accordingly, leading to unstable minima in the χ^2 minimization and prolonged fit times. To resolve this, the RMF couplings amplitudes ${}^k\mathcal{C}$ are not multiplied to $\mathcal{D}_i$. Furthermore, as discussed in chapter 4, the global phase of the total amplitude is not measurable. If $\mathcal{D}_i$ is chosen as the reference component, we fix the production coupling β_α^0 of one pole α to be real and positive, following the same convention as in chapter 6.

Table 10.1 shows the number of free fit parameters for a sum-of-Breit–Wigner dynamic amplitudes compared to a K-matrix dynamic amplitude. For the single-channel case the parameter counts are identical between the two parameterizations, since in a single channel the production coupling β_α and the RMF coupling $\mathcal{C}$ play equivalent roles. As soon as a second channel is added, the counts no longer match. The reduced parameters in the K-matrix parametrization correspond to the relative phases between the same resonance α appearing in different decay channels. Since the K-matrix provides only a single complex-valued production coupling β_α per pole α, the amplitude $\mathcal{D}$ has the same phase for the production of pole α in all channels. This deviates from a sum-of-Breit–Wigner parametrization, where all resonances have a separate production coupling.

10.1.3 Extraction of Resonance Pole Parameters

In order to obtain a model independent set of parameters describing the resonance parameters, the pole positions of the resonances have to be extracted. The mass and width parameters of a Breit–Wigner amplitude depend on their parameterization, as shown in ref. [85]. The poles of the resonances are encoded within the $\hat{A}^{-1}$ matrix. Wherever $\hat{A}$ is not invertible, i.e., $\det \hat{A} = 0$, the inverse $\hat{A}^{-1}$, and hence the amplitude, diverges, signalling a pole. The poles of the $\hat{A}^{-1}$ matrix directly correspond to the poles of the S matrix, and thus describe the pole positions of the resonances. In order to extract the pole positions one has to consider the complex structure of the $\hat{A}$ matrix, especially that of the two body phase space matrix $\hat{\rho}$. Every mass threshold $s_{i,\mathrm{thr}} = (m_{1,i} + m_{2,i})^2$ creates a branch point in the two body phase space. In the case of $m_1 = m_2$ this can be seen in the two body phase space as:

$$\rho_i = \sqrt{\frac{s - s_{i,\mathrm{thr}}}{s}}. \tag{10.13}$$

The square root in the two body phase space creates two possible solutions, i.e., two possible Riemann sheets. The measured physical amplitudes are always evaluated on the physical sheet, i.e. $\mathrm{Im}\,\rho_i \geq 0$. In order to access one of the unphysical sheets, one or more of the branch cuts have to be crossed. This is achieved by multiplying the corresponding ρ_i with -1. For a single channel K-matrix it is straightforward: the physical sheet I has $\mathrm{Im}\,\rho_1 \geq 0$ and sheet II has $\mathrm{Im}\,\rho_1 < 0$. A pole appears on the unphysical sheet that connects analytically to the physical sheet in the energy region of the resonance. This is the sheet reached by flipping $\mathrm{Im}\,\rho_i$ for every channel whose threshold lies below the resonance mass. One should note here that every pole s_R is accompanied by its complex conjugate s_R^*.This description does not constitute a full classification of poles on all possible Riemann sheets, for that we refer the reader to ref. [86].

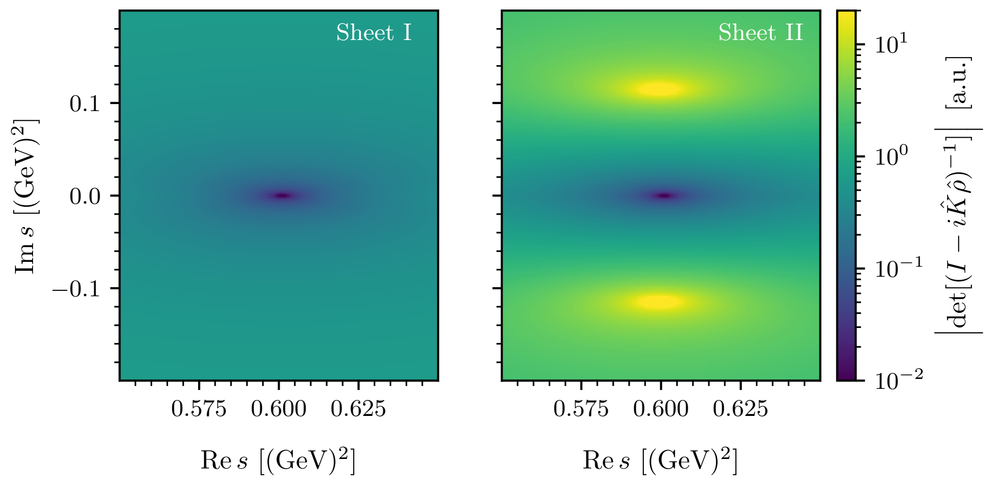

Figure 10.2: $|\det \hat{A}^{-1}|$ for a single channel K-matrix parameterization of the $\rho(770)$ decaying into $\pi^+\pi^-$ evaluated in complex s-plane. The colorbar is logarithmic and has an upper limit of 20, for better visualization of the pole structure. In the upper right corner the label of the Riemann sheet that the plot was created for is shown.

After locating the correct sheet for the corresponding poles, we perform a fit to extract the pole position. In the fit we minimize $|\det \hat{A}|$ with respect to s. The value of s for which $|\det \hat{A}|$ vanished is the pole position in the complex s-plane. We then run 100 fits with starting values drawn randomly from a range of about $\pm 0.05\,(\mathrm{GeV})^2$ around the visually determined pole position. Running many randomized starts guards against convergence to local minima. We accept a pole only if the same fit result, i.e., same function value and real and imaginary parts of s, is reproduced at least twice within a tolerance of 10^{-5}.

Figure 10.2 shows $|\det \hat{A}^{-1}|$ and fig. 10.3 shows $|\mathcal{D}(s)|$ for a single channel K-matrix parameterization of the $\rho(770)$ decaying into 2π. We first discuss the determinant in fig. 10.2. Sheet I shows a uniform value across the displayed range and exhibits only a single dark spot at about $\mathrm{Re}\, s = 0.6\,(\mathrm{GeV})^2$. Sheet II shows a dark blue spot at a similar $\mathrm{Re}\, s$ value, and in addition a yellow spot directly above and below it. The blue spots correspond to values of $|\det \hat{A}^{-1}|$ close to zero. There, $\det \hat{A} \to \infty$ holds true. This is a direct consequence of the $\hat{K}$-matrix pole at the bare mass m_α (see eq. (10.6)), so that $\hat{A} = I - i\hat{K}\hat{\rho}$ diverges there as well. The blue spot therefore marks the bare mass of the $\hat{K}$-matrix pole, and not a resonance pole. This is consistent with our expectation that it is located at the bare mass, which for the $\rho(770)$ is $m_\alpha = m_\rho$, i.e. $\mathrm{Re}\, s = m_\alpha^2 = (m_\rho)^2 = (0.77\,\mathrm{GeV})^2 = 0.61\,(\mathrm{GeV})^2$. The actual resonance poles correspond to the opposite case, $|\det \hat{A}| \to 0$, i.e., to divergences of $|\det \hat{A}^{-1}|$. These

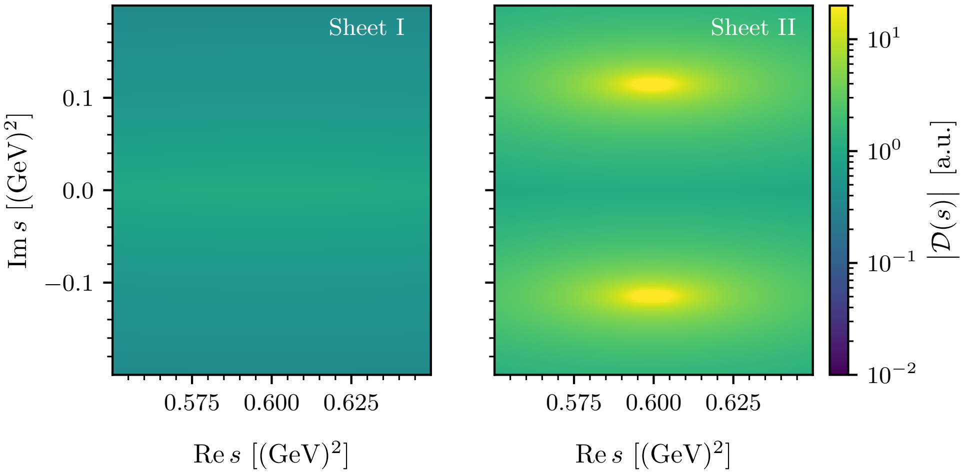

Figure 10.3: $|\mathcal{D}(s)|$ for a single channel K-matrix parameterization of the $\rho(770)$ decaying into $\pi^+\pi^-$ evaluated in complex s-plane. The colorbar is logarithmic and has an upper limit of 20, for better visualization of the pole structure. In the upper right corner the label of the Riemann sheet that the plot was created for is shown.

are the two yellow spots on sheet II. Since sheet II is the only unphysical sheet in the single channel case, and resonance poles are only expected on the unphysical sheet, we conclude that the two yellow spots correspond to the pole of the $\rho(770)$ resonance and its complex conjugate.

The same poles are visible in the amplitude $|\mathcal{D}(s)|$ in fig. 10.3. Here, however, the blue spot at the bare mass is absent. The reason is that the production vector $\hat{P}$ also contains the $\hat{K}$-matrix pole at m_α (see eq. (10.10)). When forming the amplitude $\hat{F} = \hat{A}^{-1}\hat{P}$, the zero of $\hat{A}^{-1}$ at the bare mass is multiplied by the divergence of $\hat{P}$ at the same point, so that the two cancel and the amplitude remains finite there. The amplitude thus displays only the physical resonance poles, without the parameterization artifact at the bare mass, which makes it the cleaner object for visualizing the pole structure.

10.2 Simple Examples of the K-Matrix Formalism

This section concentrates on three analytically solvable cases of the K-matrix formalism. Since the formalism is complex and non-trivial to implement, we validate our implementation by comparing the amplitudes obtained from our K-matrix code against the known analytic results for each case. In order to perform the comparison we parametrize the decay couplings as:

$$g^0_{\alpha i} = \gamma_{\alpha i}\sqrt{m_\alpha \Gamma^0_\alpha} \tag{10.14}$$

$\gamma_{\alpha i}$ corresponds to a real-valued decay coupling. m_α and Γ^0_α correspond to the bare mass and width of pole α. The bare width is defined as the sum over channel i of the K-matrix partial widths $\bar{\Gamma}_{\alpha i}$ divided by the two body phase space

$$\Gamma^0_\alpha = \sum_i \frac{\bar{\Gamma}_{\alpha i}}{\rho_i(m^2_\alpha)}. \tag{10.15}$$

The production couplings β^0 are rescaled as

$$\beta^0_\alpha = \beta_\alpha \sqrt{m_\alpha \Gamma^0_\alpha}. \tag{10.16}$$

to be dimensionless. These parameterizations express the decay and production couplings in terms of the bare mass m_α and width Γ^0_α, which makes the connection to the Breit–Wigner and Flatté parameterizations transparent.

It will be shown in section 10.2.1 that this approach yields in a specific example the dynamic widths Breit–Wigner introduced in eq. (4.29). Then in section 10.2.2, we show the limitations of a sum of two Breit–Wigner amplitudes compared to the K-matrix amplitude. Lastly, in section 10.2.3 it will be shown how the P-vector approach yields the Flatté parameterization.

10.2.1 Example: Single Pole Single Channel

When the P-vector approach represents a scattering process, where only one pole in a single channel appears, the $\hat{K}$, $\hat{\rho}$, $\hat{P}$ and, $\mathcal{D}$ correspond to scalar values, not matrices or vectors. Both parameterizations for $g^0_{\alpha i}$ (see eq. (10.14)) and β^0_α (see eq. (10.16)) have been used. Since we only have one channel and pole, we drop both indices.

$$\hat{K} = \frac{\gamma^2 \left[B^L(q^2, q^2_0)\right]^2 m_0 \frac{\bar{\Gamma}}{\rho(m_0)}}{m^2_0 - s} \tag{10.17}$$

$$\hat{P} = \frac{\beta\gamma B^L(q^2, q^2_0) m_0 \frac{\bar{\Gamma}}{\rho(m_0)}}{m^2_0 - s} \tag{10.18}$$

$$\hat{F} = \frac{\beta\gamma B^L(q^2, q^2_0) m_0 \frac{\bar{\Gamma}}{\rho(m_0)}}{m^2_0 - s - i\gamma^2 \left[B^L(q^2, q^2_0)\right]^2 m_0 \frac{\bar{\Gamma}}{\rho(m_0)} \rho(s)} \tag{10.19}$$

For simplicity we set $\gamma = \beta = 1$. Additionally, we use the two body phase space defined in eq. (10.7), which then yields an amplitude of

$$\mathcal{D}(s) = \frac{\frac{m_0 \bar{\Gamma}}{b^L(q^2)\rho(m^2_0)}}{m^2_0 - s - i m_0 \bar{\Gamma}\left[B^L(q^2, q^2_0)\right]^2 \frac{q}{q_0}\frac{m_0}{\sqrt{s}}} \tag{10.20}$$

This equation corresponds to that of the dynamic width Breit–Wigner, that was defined in eq. (4.29), with the only difference being a different normalization.

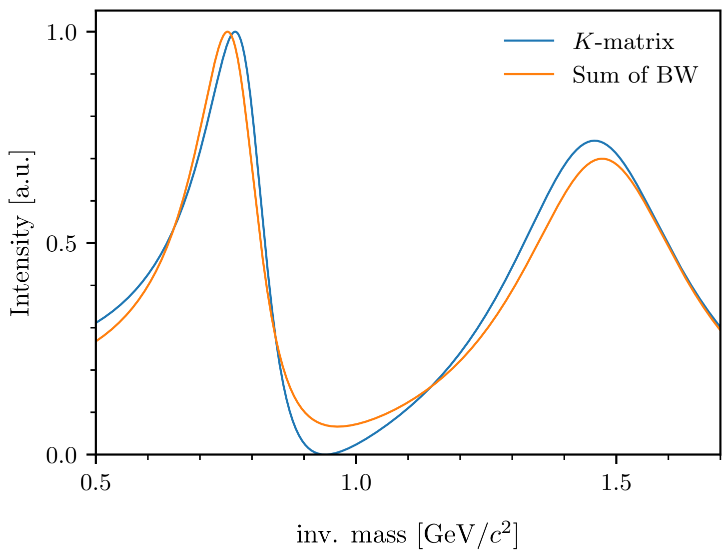

Figure 10.4: Intensity spectra of the $\rho(770)$ and $\rho(1450)$ decaying into 2π in a P-wave constellation. Both intensities were normalized such that the highest peak has an intensity of one. The blue curve corresponds to the intensity obtained in the P-vector approach. The orange curve corresponds to the intensity obtained by a sum of two Breit–Wigner amplitudes.

10.2.2 Example: Double Pole Single Channel

It is very instructive to study the case of a single channel with two poles. Since we only have one channel the channel index i is dropped. For simplicity reasons we set $\gamma_\alpha = \beta_\alpha = 1\,\forall\alpha$. The amplitude is then given by:

$$\begin{aligned}\mathcal{D}(s) =& \frac{\frac{m_0\bar{\Gamma}_0}{b_0^L(q_0^2)\rho(m_0^2)}}{m_0^2 - s - i\rho(s)\left[B^L(q^2,q_0^2)\right]^2 m_0 \frac{\bar{\Gamma}_0}{\rho(m_0^2)} - i\rho(s)\left[B^L(q^2,q_1^2)\right]^2 m_1 \frac{\bar{\Gamma}_1}{\rho(m_1^2)}\frac{m_0^2-s}{m_1^2-s}} \\ &+ \frac{\frac{m_1\bar{\Gamma}_1}{b_0^L(q_1^2)\rho(m_1^2)}}{m_1^2 - s - i\rho(s)\left[B^L(q^2,q_1^2)\right]^2 m_1 \frac{\bar{\Gamma}_1}{\rho(m_1^2)} - i\rho(s)\left[B^L(q^2,q_0^2)\right]^2 m_0 \frac{\bar{\Gamma}_0}{\rho(m_0^2)}\frac{m_1^2-s}{m_0^2-s}}.\end{aligned} \tag{10.21}$$

Here, it is directly apparent that this representation does not correspond to a sum of two Breit–Wigner amplitudes. This discrepancy is also visible in fig. 10.4, which shows the intensity spectra for the $\rho(770)$ and $\rho(1450)$ decaying into 2π in a P-wave configuration. While both spectra exhibit a similar overall shape, clear differences are visible. The peak positions are shifted and the dip at about $0.8\,\mathrm{GeV/c^2}$ reaches zero only in the intensity of the K-matrix formalism. This demonstrates that a sum of Breit–Wigner amplitudes does not correctly describe a system of two overlapping resonances.

It is also interesting to study two limiting cases. First, when we let $m_0 = m_1$ and $\bar{\Gamma}_0 = \bar{\Gamma}_1$, then the amplitude in eq. (10.21) reduces to that of a single Breit–Wigner amplitude. Second, we can also consider two isolated resonances, i.e., $|m_0 - m_1| \to \infty$. In this limit, near the pole at m_0 the denominator $m_1^2 - s \approx m_1^2 - m_0^2 \to \infty$, so the cross term $\frac{m_0^2 - s}{m_1^2 - s} \to 0$ and the interference between the two poles vanishes. The same argument applied near m_1. The amplitude then reduces to:

$$
\begin{aligned}
\mathcal{D}(s) =& \frac{\frac{m_0 \bar{\Gamma}_0}{b_0^L(q_0^2)\rho(m_0^2)}}{m_0^2 - s - i\rho(s)\left[B^L(q^2, q_0^2)\right]^2 m_0 \frac{\bar{\Gamma}_0}{\rho(m_0^2)}} \\
&+ \frac{\frac{m_1 \bar{\Gamma}_1}{b_0^L(q_1^2)\rho(m_1^2)}}{m_1^2 - s - i\rho(s)\left[B^L(q^2, q_1^2)\right]^2 m_1 \frac{\bar{\Gamma}_1}{\rho(m_1^2)}},
\end{aligned}
\tag{10.22}
$$

i.e., a sum of two Breit–Wigner amplitudes. This shows, that the Breit–Wigner approximation only holds true for isolated resonances, as mentioned at the beginning of this chapter.

10.2.3 Example: Single Pole Double Channel

As the last example we consider a single pole in two coupled channels, as introduced at the beginning of this chapter. As there are two channels, the $\hat{K}$, $\hat{\rho}$, $\hat{P}$ and $\mathcal{D}$ are represented by matrices or vectors. Since in this example we only have one resonance the index α for the poles will be dropped. The coupling factors β and γ_i are set to one. This yields

$$
\mathcal{D}(s) = \begin{pmatrix}
\frac{\frac{m_0 \bar{\Gamma}_0}{b_0^L(q_0^2)\rho(m_0^2)}}{m_0^2 - s - i\frac{\bar{\Gamma}_0}{\rho(m_0^2)}\left(\left[B_0^L(q^2,q_0^2)\right]^2\rho_0 + \left[B_1^L(q^2,q_0^2)\right]^2\rho_1\right)} \\
\frac{\frac{m_0 \bar{\Gamma}_0}{b_1^L(q_0^2)\rho(m_0^2)}}{m_0^2 - s - i\frac{\bar{\Gamma}_0}{\rho(m_0^2)}\left(\left[B_0^L(q^2,q_0^2)\right]^2\rho_0 + \left[B_1^L(q^2,q_0^2)\right]^2\rho_1\right)}
\end{pmatrix}
\tag{10.23}
$$

for the invariant amplitudes for each channel. Both channels have essentially the same amplitude, but different normalizations.

This is a prime example of the K-matrix formalism. This well-known amplitude was already introduced eq. (4.34) as the Flatté amplitude. By comparison of coefficients we can deduce that setting $\gamma_1 = m_0 \frac{\bar{\Gamma}_0}{\rho(m_0)}$ and $\gamma_{21} = 1$ in eq. (4.34) yields the same amplitude as that obtained from the K-matrix in eq. (10.23).

10.2.4 Cross-check of Correct Implementation

So far we have shown for three examples the invariant amplitudes in the K-matrix formalism. Since the implementation of the formalism introduced in section 10.1.1 is not

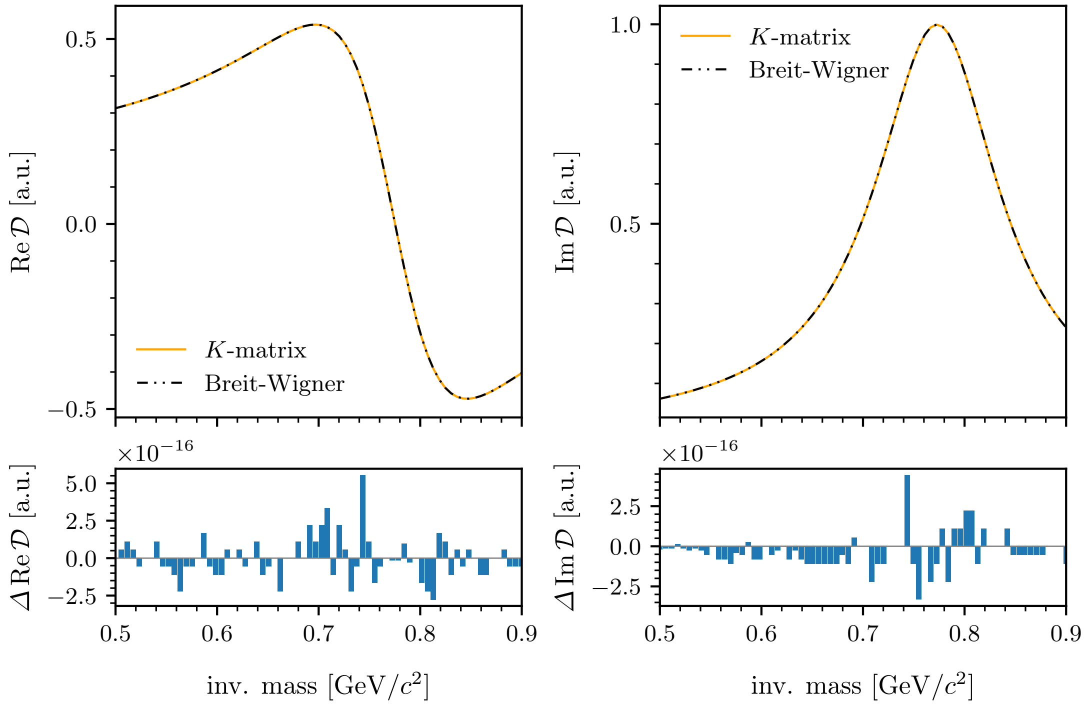

Figure 10.5: Cross check for a single pole in a single channel K-matrix. The real (left side) and imaginary (right side) parts of the amplitude of a $\rho(770)$ decaying to 2π were plotted in the upper two plots. The orange curves correspond to the amplitude obtained from the K-matrix formalism. The black curves correspond to the dynamic width Breit–Wigner parameterization. Both amplitudes were normalized such, that the peak has an intensity of one. The deviation of the two parameterizations is shown in the lower panels.

trivial, it is good practice to cross-check the implementation against well known cases. We have cross-checked the implementation against all three examples mentioned in section 10.2. We will discuss the case with a single pole in a single channel in this section. The other cross-checks can be found in appendix C.

In order to cross-check the single pole single channel case described in section 10.2.1, we have chosen the $\rho(770)$ decaying to 2π. We have specifically chosen a decay of a particle with spin larger than 0, to also test the correct implementation of the barrier factors, since the barrier factors for a spin 0 decay are simply one. Both the real and imaginary parts of the amplitudes obtained from $\mathcal{D}$ in the K-matrix formalism (see eq. (10.12)) and from the Breit–Wigner (see eq. (4.29)) have been plotted in fig. 10.5. Note that both amplitudes were normalized such that the intensity at the maximum is one. Both curves overlap by eye, demonstrating that both implementations yield the same amplitudes. The deviations are in the order of $\mathcal{O}(10^{-16})$. We have used a

64-bit double number for our test. A 64-bit double-precision floating-point float has a precision of 53-bits [87], i.e., a precision of $2^{-53} \approx 1.11 \times 10^{-16}$. Our deviations are in the same order as the expected precision of a 64-bit double-precision floating-point number. Thus, our K-matrix formalism yields the same result as the correct analytic formula for a single pole in a single channel.

10.3 Test Validity of K-Matrix Approach in RMFs

With the formalism established, RMFs using the K-matrix parametrization can now be performed. These fits serve as a consistency check on the correct implementation of the K-matrix method. We use the reconstructed pseudo-data sample introduced in chapter 8. This means that the input model contains a sum-of-Breit–Wigner parametrization, while our fit model now contains the K-matrix parametrization. As long as we use a single-channel single-pole K-matrix parametrization, both amplitudes are identical above the $s_{\text{thr}} = (m_\xi + m_\pi)^2$ threshold. Below the threshold, the Breit–Wigner and K-matrix use different conventions for the phase-space factor, as the K-matrix parametrization needs to support continuation into the complex energy plane. The amplitudes therefore differ below the threshold. As soon as a second channel or pole is added, the parametrizations differ by construction.

We discuss three examples that validate different aspects of the K-matrix parametrization fits. In section 10.3.1 only the $1^+ f_0(980)\pi P$ wave with a single-pole, single-channel K-matrix is fitted. All parameters are fixed except for the production coupling β_α. As only a single channel with a single pole is fitted, this validates the correct implementation of the dynamic amplitude of the K-matrix parametrization. In section 10.3.2 the $1^+ f_0(980)\pi P$ wave is again fitted with a single pole in a single channel. This time all parameters are left floating, and as an additional test a polynomial of 0-th order is added, to check that the fit still converges and recovers the input parameters. This validates the technical functionality of the d_i polynomial in eq. (10.10). Lastly, in section 10.3.3 the $1^+\rho(770)\pi S$ and $1^+(\pi\pi)_S\pi P$ waves are fitted using a K-matrix with two poles in two channels. As the input and RMF models are no longer identical in this case, this only validates the technical functionality of more complex K-matrix parametrization fits.

10.3.1 Fit of $1^+ f_0(980)\pi P$ Wave with Fixed Parameters

We fit to only the intensity of the $1^+ f_0(980)\pi P$ wave with all parameters fixed to the input model values, except for the production coupling β_α, which are determined by the

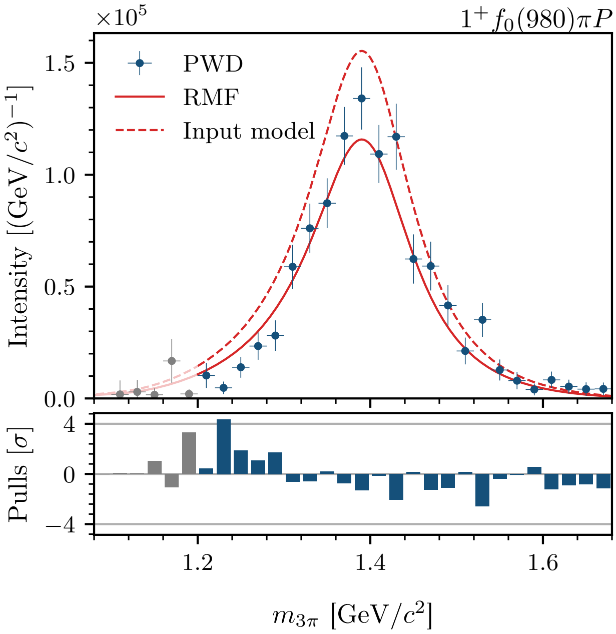

Figure 10.6: Same as fig. 7.1. The gray points are intensities that were not included in the fit range. The light red curve indicates an extrapolation of the RMF model outside the fit range. The light red dashed curve is the input model outside the fit range. And the gray bars are the pulls of the extrapolated RMF model versus the intensity. The RMF was performed with a K-matrix for a single pole in a single channel. The parameters of the fit were fixed to those of the input model. Only the production coupling β_α was a fittable parameter.

fit. As only one wave was fitted, it was chosen as the reference wave, constraining the production coupling to be real and positive, so that it only scales the overall intensity. As the fit range we chose $1.2\,\text{GeV}/c^2 \leq m_{3\pi} < 1.7\,\text{GeV}/c^2$. As discussed in section 10.2.1, we expect the shapes of the K-matrix amplitude and Breit–Wigner input model to be similar. Therefore, this RMF provides an ideal cross-check to validate the removal of the barrier factor b^L, since the $1^+ f_0(980)\pi P$ wave has $L = 1$ and therefore non-trivial barrier factors. In fig. 10.6 we observe that both the input model curve and the RMF curve have identical shapes. The input model curve has higher intensity than that of the RMF. This discrepancy is consistent with the intrinsic analysis bias discussed in chapter 8. We conclude that the modification introduced in eq. (10.12) correctly accounts for the barrier factor already present in the RMF framework.

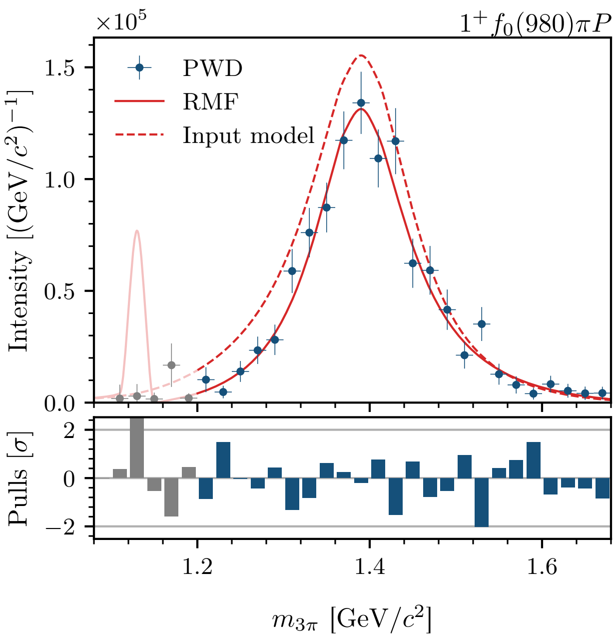

Figure 10.7: Similar to fig. 7.1. The fit was performed on the $1^+ f_0(980)\pi P$ wave with a K-matrix for a single pole in a single channel. An additional polynomial of 0-th order was added to the $\hat{P}$ vector.

10.3.2 Fit of $1^+ f_0(980)\pi P$ Wave with Production Vector Polynomial

In the second test, the $1^+ f_0(980)\pi P$ wave was fitted with the K-matrix parametrization, where all parameters were left floating, also including a polynomial of 0-th order that was added to the production vector, to cross-check that the fit formalism still performs well. The intensity spectrum of that fit is shown in fig. 10.7. The curve of the RMF fits well through the data points of the PWD, as the pulls have absolute values of only up to $2\,\sigma$.

Around $m_{3\pi} = 1.15\,\text{GeV}/c^2$ a second peak can be observed. As this $m_{3\pi}$ region was excluded from the fit, the model curve there is an extrapolation. This peak is at first surprising, since, as established in section 10.2.1, a single-pole, single-channel K-matrix should yield the same amplitude as the corresponding Breit–Wigner above threshold, which does not exhibit such a structure. The origin of this peak lies in a difference between the K-matrix formalism and the RMF framework in how the barrier factors are calculated. In the K-matrix formalism, the barrier factors for the decay $X^- \to \xi^0\pi^-$ are calculated from the nominal masses of the isobar resonances. This is in contrast to the PWD and RMF, where these quantities are calculated event by event from the invariant mass $m_{\pi^+\pi^-}$ of the $\pi^+\pi^-$ system in the decay $\xi^0 \to \pi^+\pi^-$.

Table 10.2: RMF parameters of single pole single channel K-matrix fit to $1^+ f_0(980)\pi P$ wave. As a comparison the last column lists the values of the input model. The obtained value for the production coupling is not shown, as we do not have an input model value to compare it to.

	RMF value	Input value
bare mass	$(1399 \pm 6)\,\mathrm{MeV}/c^2$	$1410\,\mathrm{MeV}/c^2$
decay coupling	$(-636 \pm 22)\,\mathrm{MeV}/c^2$	$666\,\mathrm{MeV}/c^2$
production polynomial	(21 ± 6)	0

As $m_{3\pi}$ approaches the mass threshold $s_{\mathrm{thr}} = (m_\xi + m_\pi)^2$, the barrier factor b^L in the K-matrix parametrization becomes very small. Since $\hat{F}_i$ is divided by this factor in eq. (10.12), it grows large around s_{thr}, creating a spurious peak in the intensity. Although b^L is multiplied onto $\mathcal{D}_i$ again in the RMF, it was calculated in the other way and therefore does not approach zero around s_{thr}, so it cannot compensate the spurious peak.

The obtained fit parameters are listed in table 10.2. The bare mass is close in value to the Breit–Wigner mass input value. This is expected as we have seen that a single pole single channel K-matrix parametrization yields the same curve as a general Breit–Wigner up to a normalization constant (see section 10.2.1). Since fitting only one partial wave corresponds to fitting only its intensity spectrum, the absolute square of eq. (10.17) is dependent on $|g^0_{\alpha i}|^2$ and $|g^0_{\alpha i}|^4$. Therefore, a negative $g^0_{\alpha i}$ yields the same intensity as the positive value. Thus, the decay coupling is consistent with the input value up to a sign. The production polynomial deviates from zero by about $3.5\,\sigma$, which is in the same order as the intrinsic analysis bias discussed in chapter 8. Therefore, we attribute the deviation to the intrinsic analysis bias.

Figure 10.8 shows the pole structure on sheet II obtained from the fit. We identify the yellow spot as the pole of the resonance. The fit of the pole position yields $\mathrm{Re}(\sqrt{s_{\mathrm{pole}}}) = (1189.63 \pm 0.21)\,\mathrm{MeV}/c^2$ and $\mathrm{Im}(\sqrt{s_{\mathrm{pole}}}) = (-94.5 \pm 2.7)\,\mathrm{MeV}/c^2$. The uncertainties were determined with a toy Monte Carlo simulation. Using the parameter estimates and their covariance matrix of the RMF, 1000 samples were generated from that multinormal distribution assuming that the parameter estimates are distributed normally. Then the pole position of each samples was fitted. The uncertainty is then given by the standard deviation of the pole-fit values.

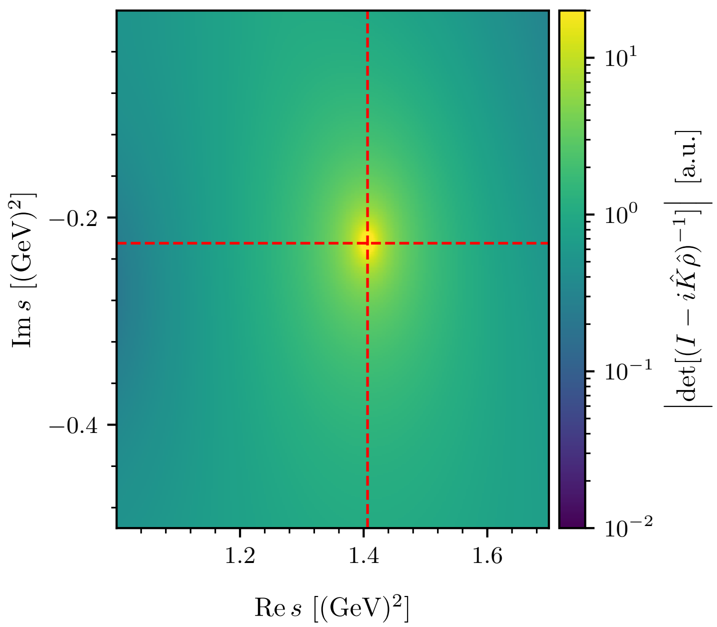

Figure 10.8: Pole structure of Sheet II in the complex s-plane of single pole, single channel RMF to $1^+ f_0(980)\pi P$ wave. The K-matrix contains an additional production polynomial of 0-th order. The colorbar is logarithmic and has an upper limit of 20, for better visualization of the pole structure. The red dashed line illustrates the fitted pole position.

10.3.3 Fit of $1^+\rho(770)\pi S$ and $1^+(\pi\pi)_S\pi P$ Waves

The K-matrix parametrization examples discussed above used only a single wave. This omitts any dependence on the relative phases between waves, since, in a single-wave RMF, only the intensity of that wave is fitted. Therefore, we performed a fit to two waves, where one partial wave corresponds to one channel in the K-matrix, including two resonances, i.e., two poles. We fit the $1^+\rho(770)\pi S$ wave with fit ranges $0.91\,\mathrm{GeV}/c^2 \leq m_{3\pi} < 1.65\,\mathrm{GeV}/c^2$ and the $1^+(\pi\pi)_S\pi P$ wave in the ranges $0.85\,\mathrm{GeV}/c^2 \leq m_{3\pi} < 1.65\,\mathrm{GeV}/c^2$. In this fit we have neither added the polynomial d_i nor the polynomial P_{ij}. All fit parameters were floating. However, we do not expect that the fit result and the input model agree, since our input model consists of a sum-of-Breit–Wigner amplitudes. As discussed in section 10.2.2, this parametrization does not show the same characteristics as a K-matrix parametrization. This makes the fit presented in this section merely a technical test whether the fitter is able to find a shape similar to the input model.

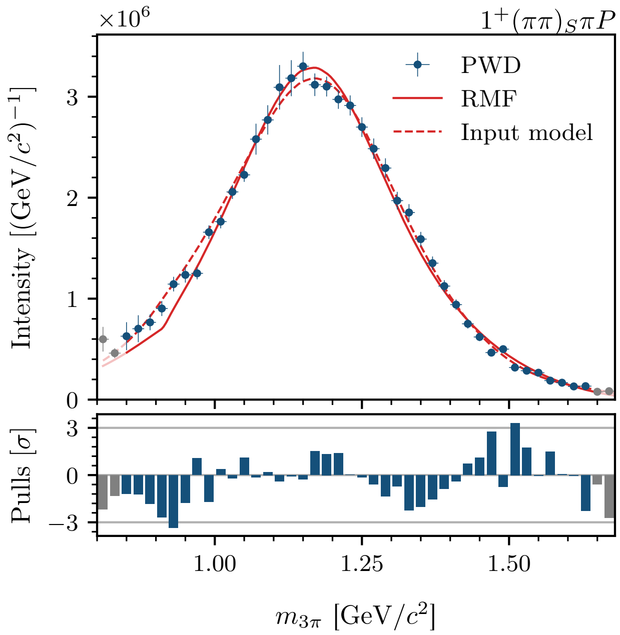

Figure 10.9: Similar to fig. 7.1. The fit was performed with a K-matrix parameterization in the P-vector approach for two poles decaying into two channels.

The intensity spectrum of the $1^{+}(\pi\pi)_S\pi P$ wave in fig. 10.9 exhibits a similar shape. The RMF and input model curves do not match exactly in their shape, as expected given the different parameterizations. The obtained values for the bare masses are: $m_1 = (1213 \pm 23)\,\mathrm{MeV}/c^2$ and $m_2 = (1293 \pm 19)\,\mathrm{MeV}/c^2$. These values deviate clearly from their input values of $m_1 = 1230\,\mathrm{MeV}/c^2$ and $m_2 = 1660\,\mathrm{MeV}/c^2$, particularly for the second bare mass. The relative phase between the $1^{+}(\pi\pi)_S\pi P$ and $1^{+}\rho(770)\pi S$ waves shown in fig. 10.10, exhibits only a slight phase motion of less than $40\,^\circ$ at $m_{3\pi} \approx 1.6\,\mathrm{GeV}/c^2$, which can be attributed to the $a_1(1640)$ resonance. The K-matrix does not reproduce the phase motion of the PWD fit results, as it only shows a slight phase motion at about $1\,\mathrm{GeV}/c^2$. As the two bare masses fitted by the K-matrix parameterization are far off their input values, it is not surprising that the phase spectrum is not well modeled in the RMF.

Overall, we have successfully demonstrated that our K-matrix formalism is capable of simultaneously fitting two poles in two channels. The observed deviations are understood and are expected given the known parameter constraints.

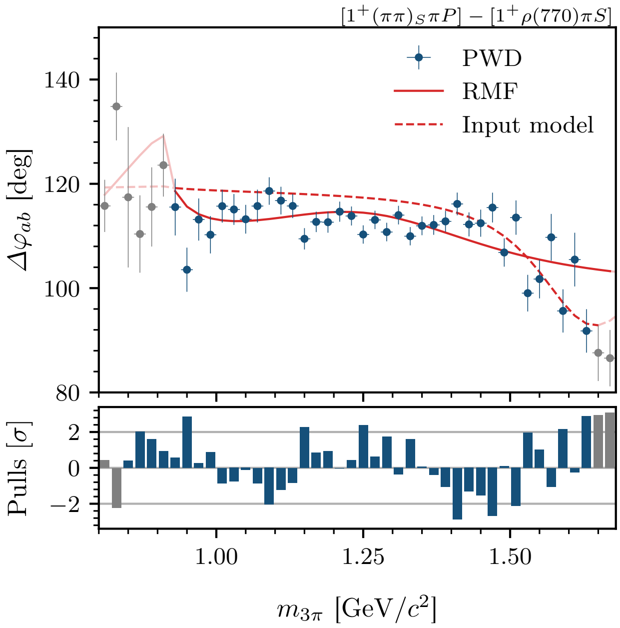

Figure 10.10: Similar to fig. 7.2. The fit was performed with a K-matrix parameterization in the P-vector approach for two poles decaying into two channels.

11 Conclusions and Outlook

This work substantially contributes to the development, implementation and validation of the partial-wave analysis (PWA) of the $\tau^- \to \pi^+\pi^-\pi^-\nu_\tau$ decays at Belle II. The main focus is the implementation and validation of the second PWA step, the resonance-model fit (RMF). To this end, we perform several input-output studies using simulated Belle II samples of this decay to estimate our sensitivity to certain signals and to estimate the bias obtained through the PWD and RMF. All studies are performed on simulated pseudo-data samples with a known input model, allowing us to validate the analysis by comparing the analysis results to the input values. Finally, we investigate models beyond the conventional sum-of-Breit–Wigner parametrization in the RMF, which the high statistical precision of the full data sample may require for an adequate description of the data.

In order to perform PWDs reliably, we have developed a `b2luigi` pipeline that streamlines the 454 individual analysis tasks into one single command pipeline. This reduces the time the analysis pipeline needs to complete from about two days to about four hours, by parallelizing analysis tasks and reusing cached analysis results where possible. The most important feature of this implementation is its reliability, removing human error from starting the correct jobs at the right time. Only this reliability enabled this work and the work in ref. [25] to be completed in the given timeframe.

Using this pipeline and the RMF, we first want to investigate the intrinsic analysis bias. To this end, we performed an input-output study on the reconstructed pseudo-data sample, which models the expected data sample from the experiment as closely as possible. In order to fully account for the intrinsic analysis bias, we would need to generate many pseudo-data samples and analyze all of them, obtaining the bias from the mean value of the deviations. As this is computationally not feasible, we approximate the bias from the deviations we observed in the RMF. As pulls of the order of one or below are consistent with a statistical fluctuation, only high pulls indicate an intrinsic analysis bias.

For the dominant $1^+\rho(770)\pi S$ wave, the yield deviates by -491×10^3 with a pull of about $29\,\sigma$. The only resonance contributing to this partial wave, the $a_1(1260)$, deviates in mass about $-3.0\,\mathrm{MeV}/c^2$ (pull of $7.5\,\sigma$), and shows no deviation in width from its input values. These deviations are highly significant statistically, yet small on the absolute scale: the yield deviation is only about 5 % of its intensity, and the mass deviation is negligible against the mass of $(1230 \pm 40)\,\mathrm{MeV}/c^2$ currently quoted by the PDG [10]. As the intensity decreases the pulls tend to decrease with the growing statistical uncertainties. For example the yield of the $0^- f_0(980)\pi S$ wave deviates by 0.3×10^3 (pull of $0.75\,\sigma$) from its input value. Overall, we observe throughout most of the extracted resonance parameters (see table 8.4) and yields (see table 8.5) significant deviations, which we interpret as indications of intrinsic analysis biases. They are generally below the uncertainties quoted by the PDG. These biases originate from both the PWD and RMF, as deviations are already present between the PWD and the input model and again between the RMF and both. These biases will enter the full systematic uncertainty of the measurement, but are of no large concern, as they are generally smaller than the uncertainties quoted by the PDG.

Comparing the RMF on the reconstructed pseudo-data sample to the signal only pseudo-data sample, which contains no background events and in which resolution effects play no role, we find the same trend with generally smaller deviations. We conclude that the background modelling works well, that neglecting resolution in the partial-wave analysis formalism does not strongly affect the description of data, and that our partial-wave analysis reproduces the input model well within in the observed biases. The small mass and width deviation on the $a_1(1260)$ against its large PDG uncertainties further suggest that our final measurement may contribute meaningfully to this state.

Following the input-output studies we investigated the sensitivity to distinguish between a triangle singularity and a genuine resonance as the origin of the $a_1(1420)$ signal. Generally, both the Breit–Wigner and triangle singularity parametrization show very similar properties if Breit–Wigner amplitude mimics the triangle singularity amplitude, with the triangle singularity showing a slightly larger tail towards higher $m_{3\pi}$. Due to the nature of the triangle singularity its shape and peak position are fixed. If we were to find the $a_1(1420)$ signal with a shape and/or peak position that deviates by about $40\,\mathrm{MeV}/c^2$ from the prediction of the triangle singularity amplitude, i.e., a shifted mass or width, we can conclude that the triangle singularity only contributes lightly to the observed signal. If we were to find the $a_1(1420)$ signal with shape and peak position close to those expected from the triangle singularity, we will likely not be able to provide a strong answer on its origin, as the similarity in shapes of the Breit–Wigner resonance and the triangle singularity does not allow us to rule out a Breit–Wigner-like resonance. One further aspect should be mentioned concerning the $a_1(1420)$ signal. As the triangle singularity is generated by the high-mass tail of the $a_1(1260)$ resonance, its intensity is linked to that of the $a_1(1260)$, i.e., the yields of both should exhibit a fixed ratio. Therefore, if the signal were to be produced by a triangle singularity we would expect that the ratio of the $a_1(1260)$ to $a_1(1420)$ yields would match between measurements independent of their production mechanism. This could be easily tested by determining the yields from the final measurement using eq. (6.15), and comparing the ratio to the one observed by the COMPASS collaboration. Overall, we can conclude that if the signal originated from a triangle singularity process, we could not rule out a general resonance as its origin. However, finding a resonance with properties that perfectly mimic the expected triangle singularity, would itself strongly favour the triangle singularity interpretation, as no conventional resonance is predicted at that position.

In the final part of this work we implemented and tested the K-matrix in the P-vector approach for parametrizing resonances. We have cross-checked in input-output studies that the Breit–Wigner input model is recreated by our single-channel single-pole K-matrix formalism, as expected. From this cross-check we validated the complicated technical implementation. We have additionally found one physics-based limitations of the K-matrix formalism we implemented. In the K-matrix parametrization we use a two-body approximation to calculate the phase-space and two-body breakup-momenta, i.e., we use a fixed mass for the isobar ξ. In the PWA this approximation is not used as the genuine invariant mass of the $\pi^+\pi^-$ system is used to calculate the quantities. This leads to artificial peaks close to the threshold $s_{\text{thr}} = (m_\xi + m_\pi)^2$ in the modeled intensity spectra. Additionally, we observed that RMFs modelling more than one decay channel exhibit unphysical results. It is the scope of an upcoming thesis, whose work has already begun, to further investigate and find solutions for these caveats. Overall, we have achieved our goal of implementing a functioning K-matrix formalism.

In summary, these results demonstrate that a working RMF has been implemented within the analysis framework. Together with the work described in ref. [25], this completes the analysis framework for the partial-wave analysis of $\tau^- \to \pi^+\pi^-\pi^-\nu_\tau$ decays at Belle II, validated on simulated pseudo-data. A natural next step is to apply the pipeline to the newer MC16rd sample provided by Belle II, allowing the framework to be tested under current detector conditions. The framework is now ready to be applied to the determination of the $a_1(1260)$ and other resonances. Owing to the clean τ^--decay final state and the reliable background modelling, it is well suited to contribute to the ongoing question of the origin of the $a_1(1420)$ signal. Once the full pipeline has been run on the new samples, and provided the input-output studies yield results comparable to those presented above, the unblinding process at Belle II can be initiated. The statistical precision observed in these studies suggests that the eventual measurement could improve upon the corresponding resonance parameters currently reported by the PDG.

A All Consistency Studies for the RMF

In this chapter we show the full fit results of the studies discussed in chapter 8. We show the real-valued spin-density matrix (see eq. (6.3)) for the RMF performed on both the MC-truth and the reconstructed signal pseudo-data samples.

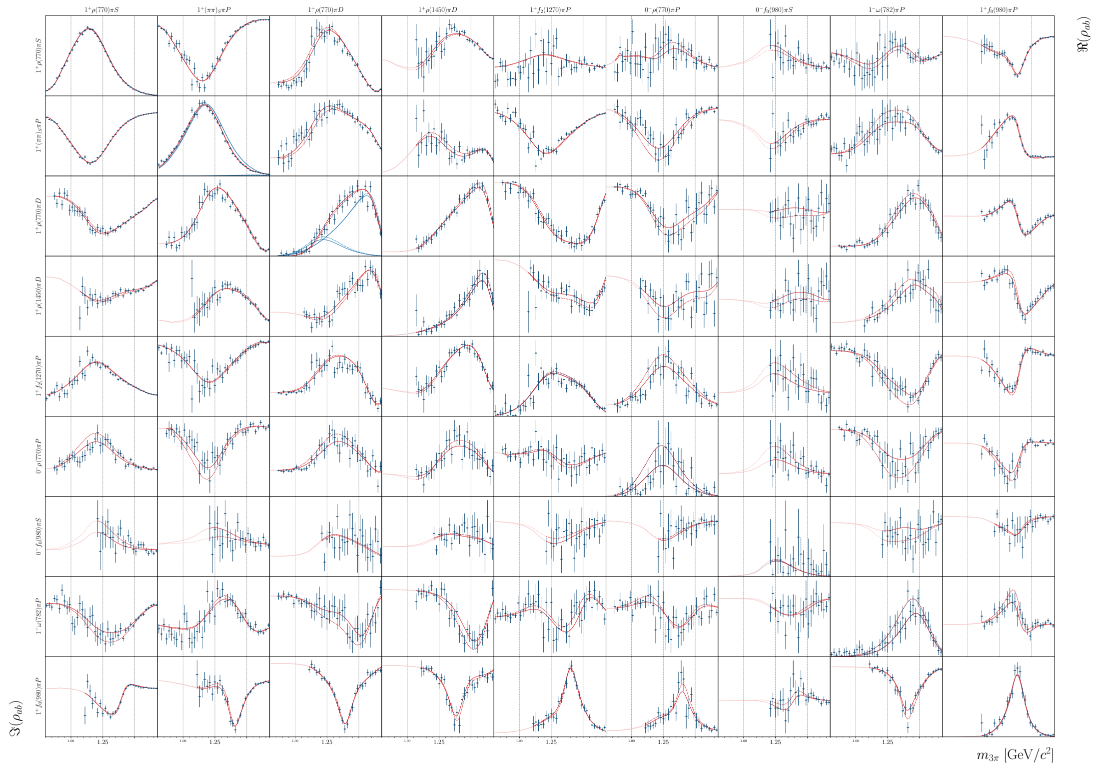

Figure A.1: Real and imaginary parts of the spin-density matrix elements $\Lambda_{ab}(m_{3\pi})$ in eq. (6.3), as a function of $m_{3\pi}$. The panels on the diagonal show the intensity spectra. The upper-right and lower-left off-diagonal panels show the real and imaginary parts of the off-diagonal spin-density matrix elements, respectively. The blue data points correspond to the spin-density matrix elements obtained from the PWD fit. The red curve corresponds to the RMF result curve, and the dashed red curve to the input model curve. In intensity spectra of partial waves that contain multiple resonant components, additionally blue curves show the intensities of the components in the partial wave as modeled by the RMF. Both are shown in lighter colors outside the fit range of the RMF, where the red RMF curve corresponds to an extrapolation of the fit. The vertical-axis ranges are adjusted individually for each panel, and tick marks are therefore omitted. This plot shows the result for the RMF performed on the MC-truth signal pseudo-data sample.

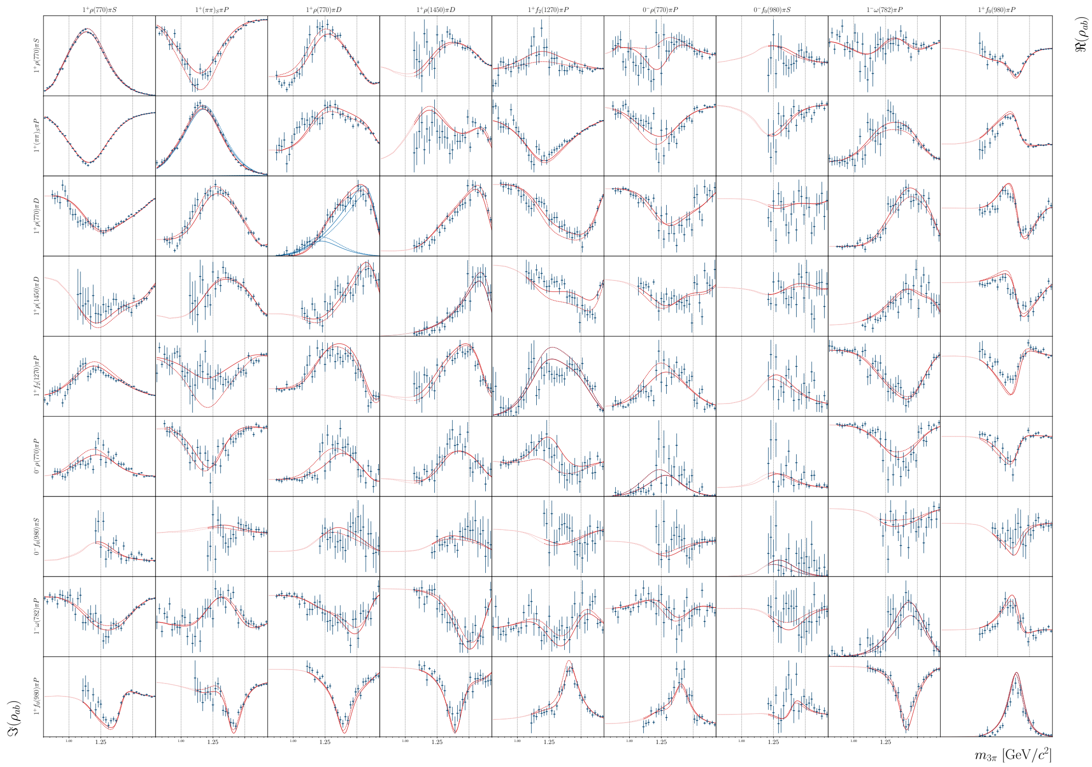

Figure A.2: Same as fig. A.1, but for the RMF performed on the reconstructed signal pseudo-data sample.

B All Studies on $a_1(1420)$ Resonance

In this chapter the results for all studies concerning the triangle singularity RMFs are summarized. We always show the fitted resonance parameters in a table followed by the real-valued spin-density matrix (see eq. (6.3)) plot.

B.1 Sensitivity in Base Models

Table B.1: Resonance parameters obtained in the *BW COMPASS* study, where the $1^{+} f_0(980)\pi P$ wave was modeled using a Breit–Wigner component.

resonance	m_0 [MeV/c^2]	Γ_0 [MeV/c^2]
$a_1(1260)$	1227.0 ± 0.4	425.0 ± 0.9
$a_1(1420)$	1418.0 ± 2.2	149 ± 4
$a_1(1640)$	1646.5 ± 2.9	268 ± 6
$\pi(1300)$	1343 ± 10	370 ± 21
$\rho(1450)$	1444 ± 11	390 ± 40

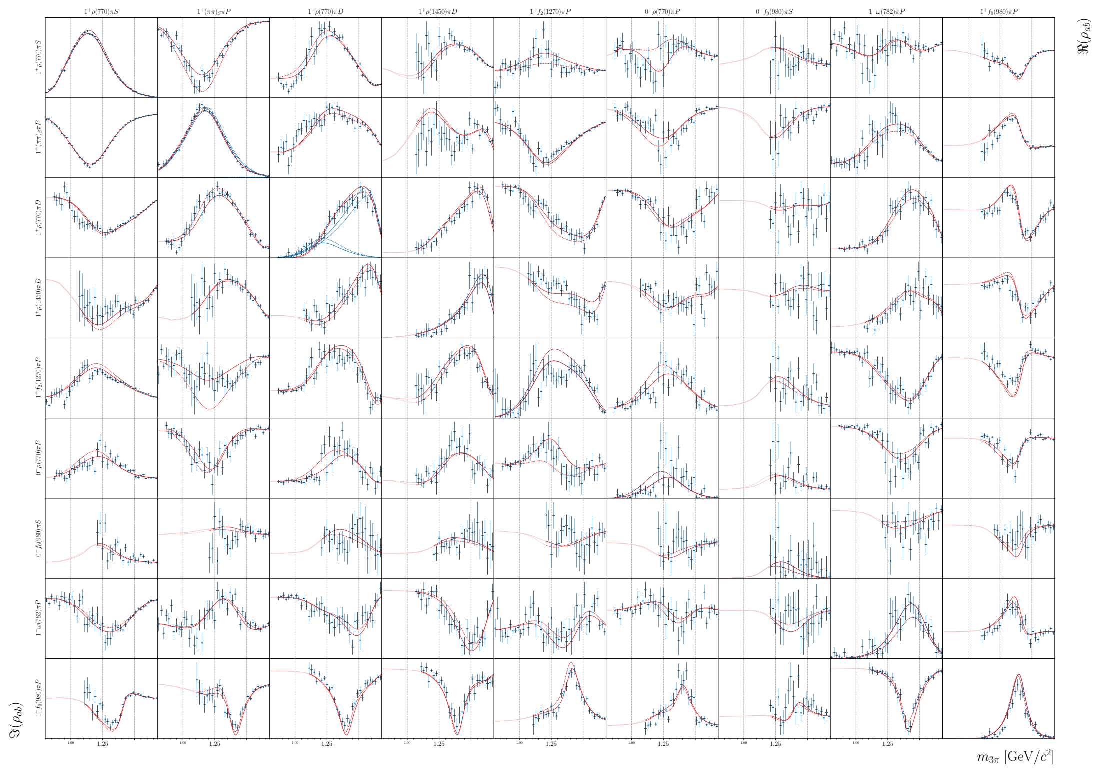

Figure B.1: Same as fig. A.1, but for the study *BW COMPASS* fitted with a Breit–Wigner component in the $1^+ f_0(980)\pi P$ wave.

Table B.2: Same as table B.1, but for the *BW COMPASS* study fitted with a triangle singularity component.

resonance	m_0 [MeV/c^2]	Γ_0 [MeV/c^2]
$a_1(1260)$	1227.1 ± 0.4	424.4 ± 0.9
$a_1(1640)$	1648.3 ± 3.0	281 ± 6
$\pi(1300)$	1338 ± 10	370 ± 21
$\rho(1450)$	1448 ± 10	362 ± 35

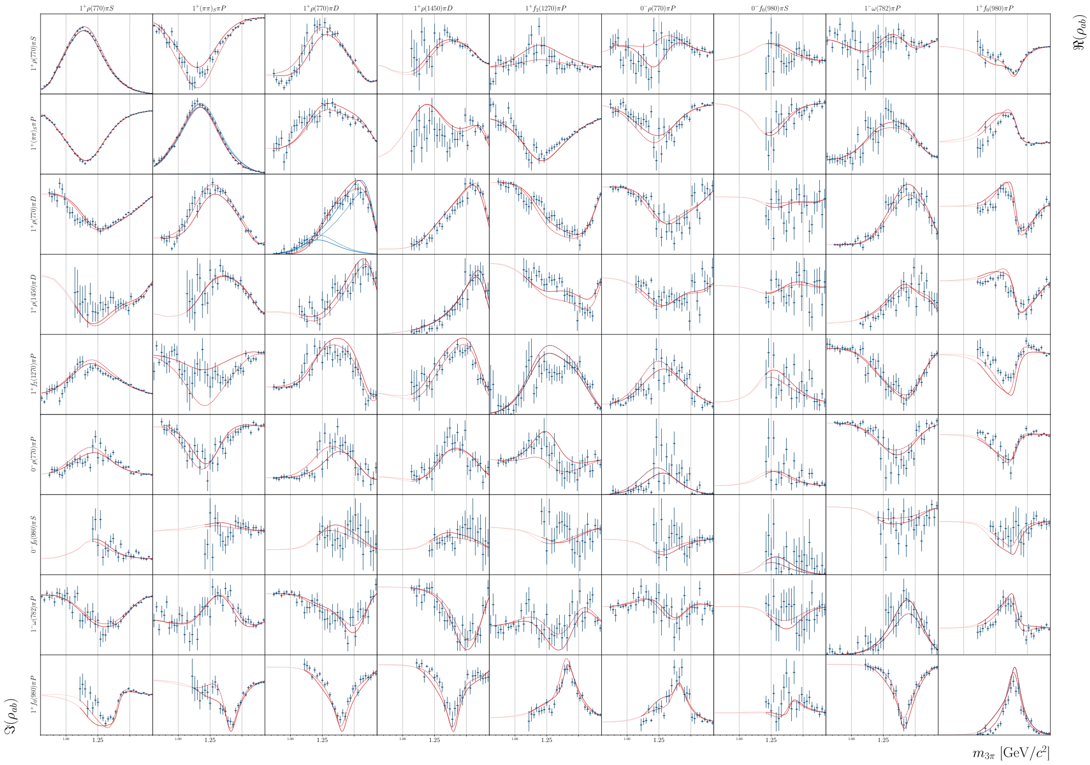

Figure B.2: Same as fig. A.1, but for the study *BW COMPASS* fitted with a triangle singularity component in the $1^+ f_0(980)\pi P$ wave.

Table B.3: Same as table B.1, but for the *BW COMPASS 10x* study fitted with a Breit–Wigner component.

resonance	m_0 [MeV/c^2]	Γ_0 [MeV/c^2]
$a_1(1260)$	1228.1 ± 0.4	426.0 ± 1.0
$a_1(1420)$	1412.2 ± 1.0	162.1 ± 2.0
$a_1(1640)$	1648.7 ± 3.3	254 ± 6
$\pi(1300)$	1315 ± 10	310 ± 23
$\rho(1450)$	1446 ± 9	323 ± 27

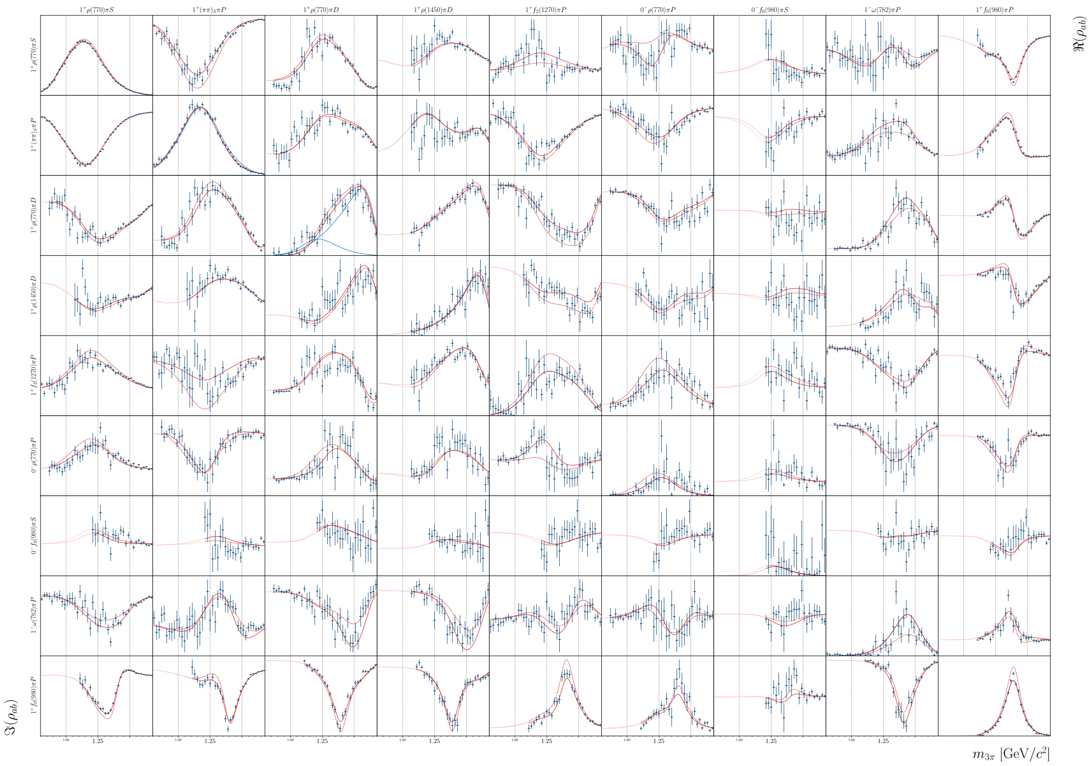

Figure B.3: Same as fig. A.1, but for the study *BW COMPASS 10x* fitted with a Breit–Wigner component in the $1^+ f_0(980)\pi P$ wave.

Table B.4: Same as table B.1, but for the *BW COMPASS 10x* study fitted with a triangle singularity component.

resonance	m_0 [MeV/c^2]	Γ_0 [MeV/c^2]
$a_1(1260)$	1229.2 ± 0.4	426.3 ± 1.0
$a_1(1640)$	1652 ± 4	292 ± 7
$\pi(1300)$	1309 ± 9	305 ± 21
$\rho(1450)$	1441 ± 8	290 ± 23

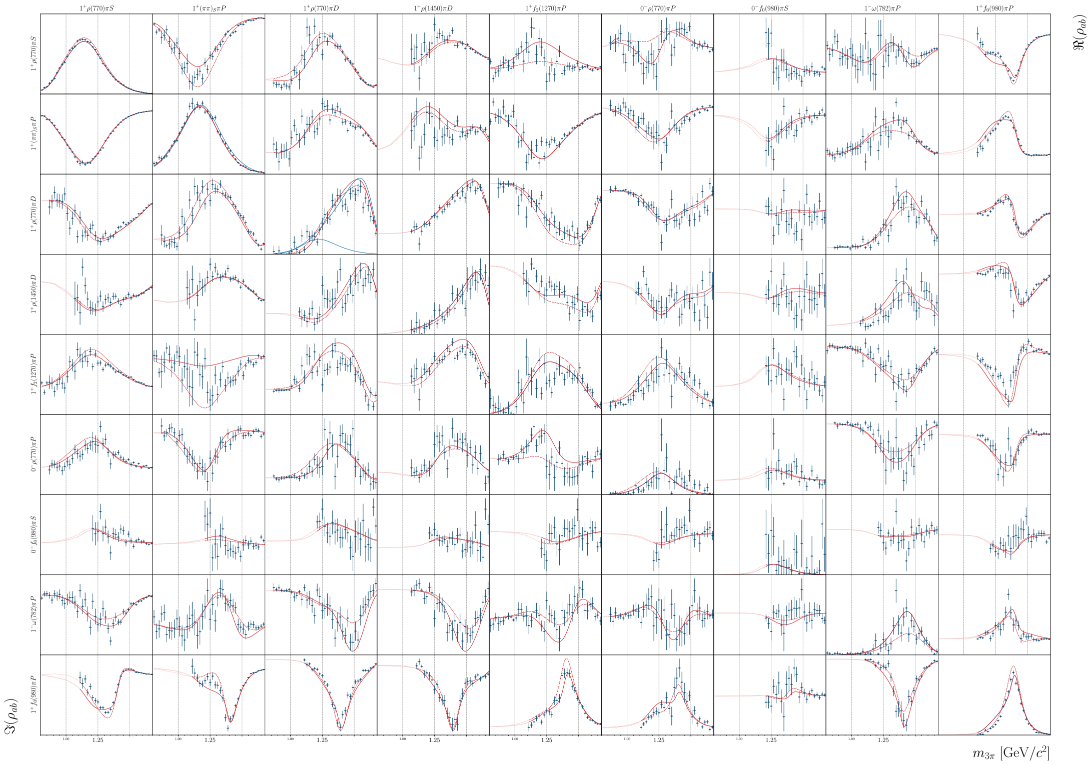

Figure B.4: Same as fig. A.1, but for the study *BW COMPASS 10x* fitted with a triangle singularity component in the $1^+ f_0(980)\pi P$ wave.

Table B.5: Same as table B.1, but for the *TS* study fitted with a Breit–Wigner component.

resonance	m_0 [MeV/c^2]	Γ_0 [MeV/c^2]
$a_1(1260)$	1226.3 ± 0.4	428.3 ± 0.9
$a_1(1420)$	1425.8 ± 2.3	169 ± 6
$a_1(1640)$	1649.1 ± 3.0	281 ± 6
$\pi(1300)$	1324 ± 9	362 ± 19
$\rho(1450)$	1455 ± 10	350 ± 40

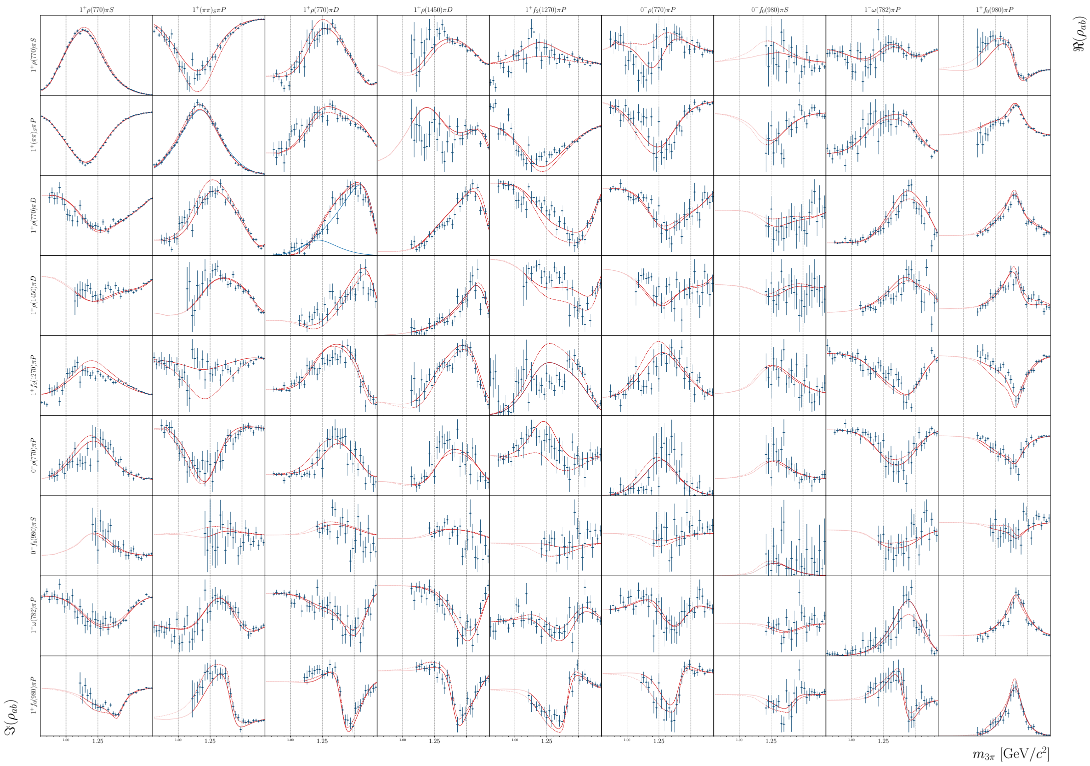

Figure B.5: Same as fig. A.1, but for the study *TS* fitted with a Breit–Wigner component in the $1^+ f_0(980)\pi P$ wave.

Table B.6: Same as table B.1, but for the *TS* study fitted with a triangle singularity component.

resonance	m_0 [MeV/c^2]	Γ_0 [MeV/c^2]
$a_1(1260)$	1226.6 ± 0.4	428.9 ± 0.9
$a_1(1640)$	1648.2 ± 3.0	284 ± 6
$\pi(1300)$	1325 ± 9	361 ± 20
$\rho(1450)$	1458 ± 9	350 ± 40

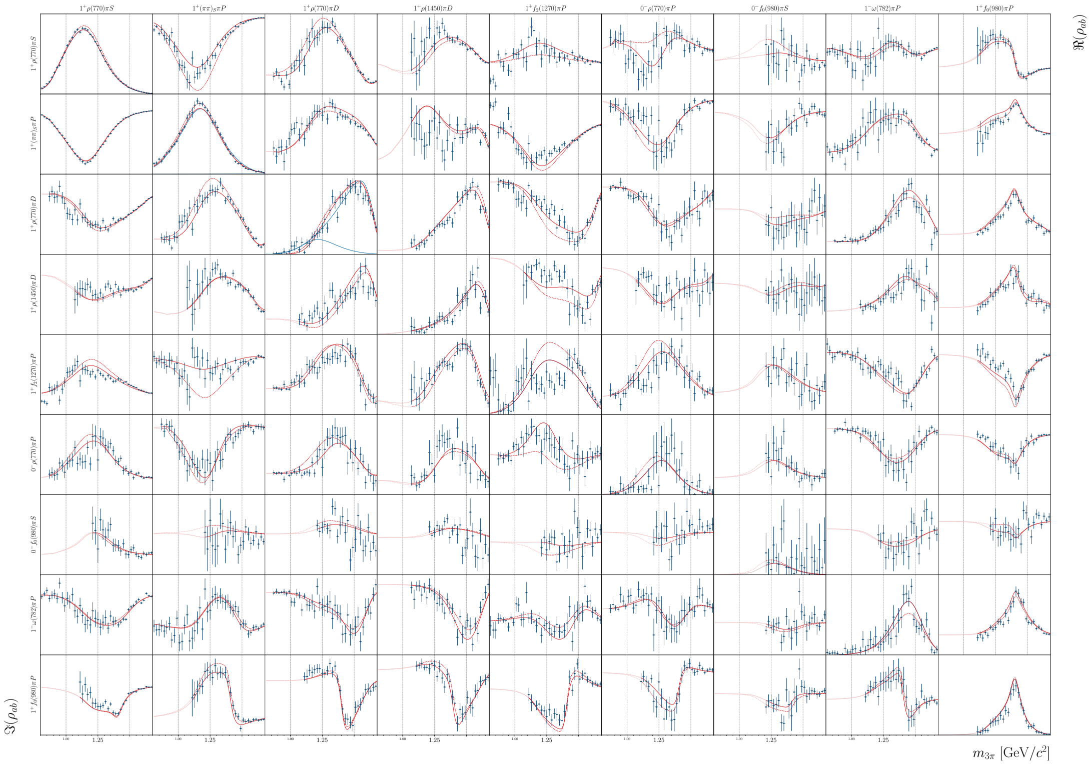

Figure B.6: Same as fig. A.1, but for the study *TS* fitted with a triangle singularity component in the $1^+ f_0(980)\pi P$ wave.

Table B.7: Same as table B.1, but for the *TS 10x* study fitted with a Breit–Wigner component.

resonance	m_0 [MeV/c^2]	Γ_0 [MeV/c^2]
$a_1(1260)$	1225.5 ± 0.4	431.2 ± 1.1
$a_1(1420)$	1420.1 ± 1.1	181.6 ± 2.9
$a_1(1640)$	1657 ± 4	259 ± 8
$\pi(1300)$	1339 ± 16	400 ± 40
$\rho(1450)$	1427 ± 22	550 ± 50

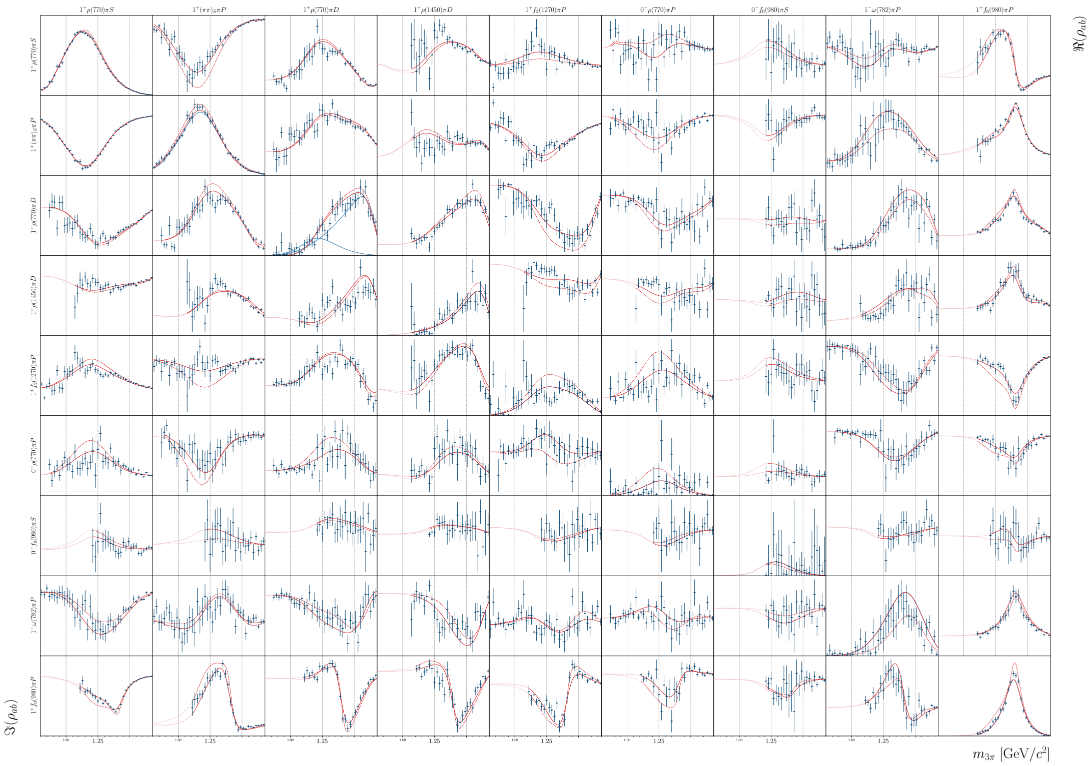

Figure B.7: Same as fig. A.1, but for the study *TS 10x* fitted with a Breit–Wigner component in the $1^+ f_0(980)\pi P$ wave.

Table B.8: Same as table B.1, but for the *TS 10x* study fitted with a triangle singularity component.

resonance	m_0 [MeV/c^2]	Γ_0 [MeV/c^2]
$a_1(1260)$	1226.8 ± 0.4	433.2 ± 1.1
$a_1(1640)$	1657 ± 4	273 ± 8
$\pi(1300)$	1343 ± 16	400 ± 40
$\rho(1450)$	1462 ± 21	520 ± 50

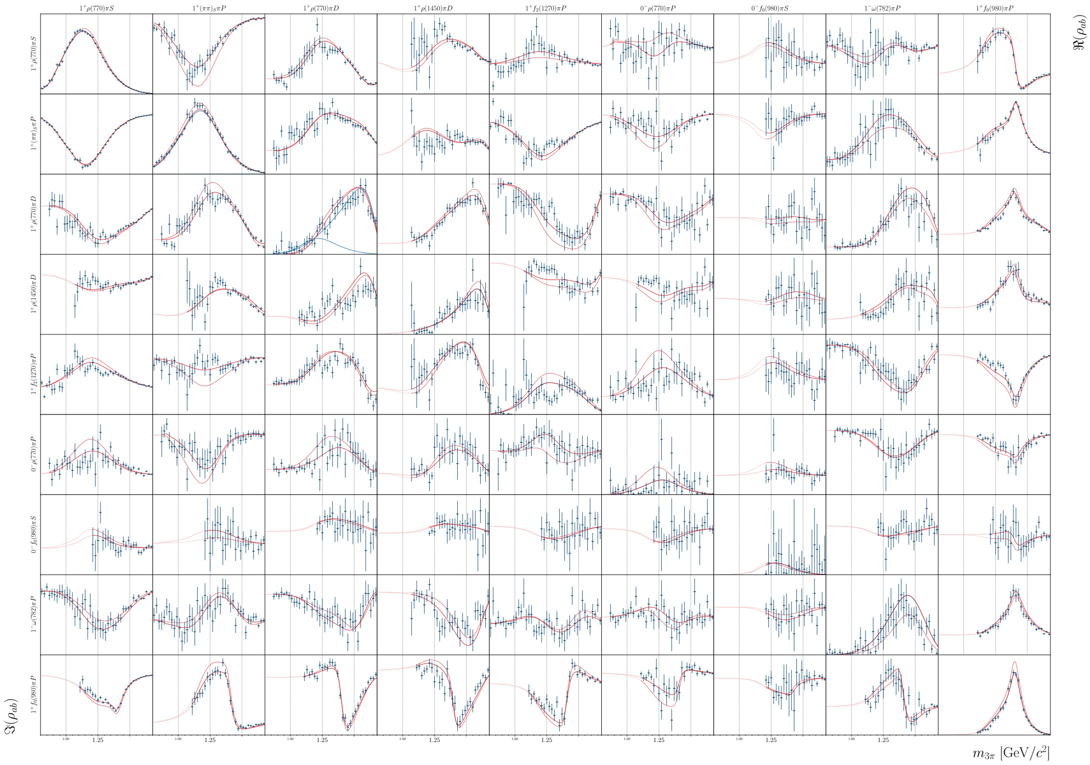

Figure B.8: Same as fig. A.1, but for the study *TS 10x* fitted with a triangle singularity component in the $1^{+}f_0(980)\pi P$ wave.

Table B.9: Same as table B.1, but for the *BW of TS* study fitted with a Breit–Wigner component.

resonance	m_0 [MeV/c^2]	Γ_0 [MeV/c^2]
$a_1(1260)$	1228.6 ± 0.4	429.9 ± 0.9
$a_1(1420)$	1431.4 ± 2.9	150 ± 5
$a_1(1640)$	1639.7 ± 2.6	233 ± 5
$\pi(1300)$	1320 ± 9	359 ± 20
$\rho(1450)$	1433 ± 13	410 ± 40

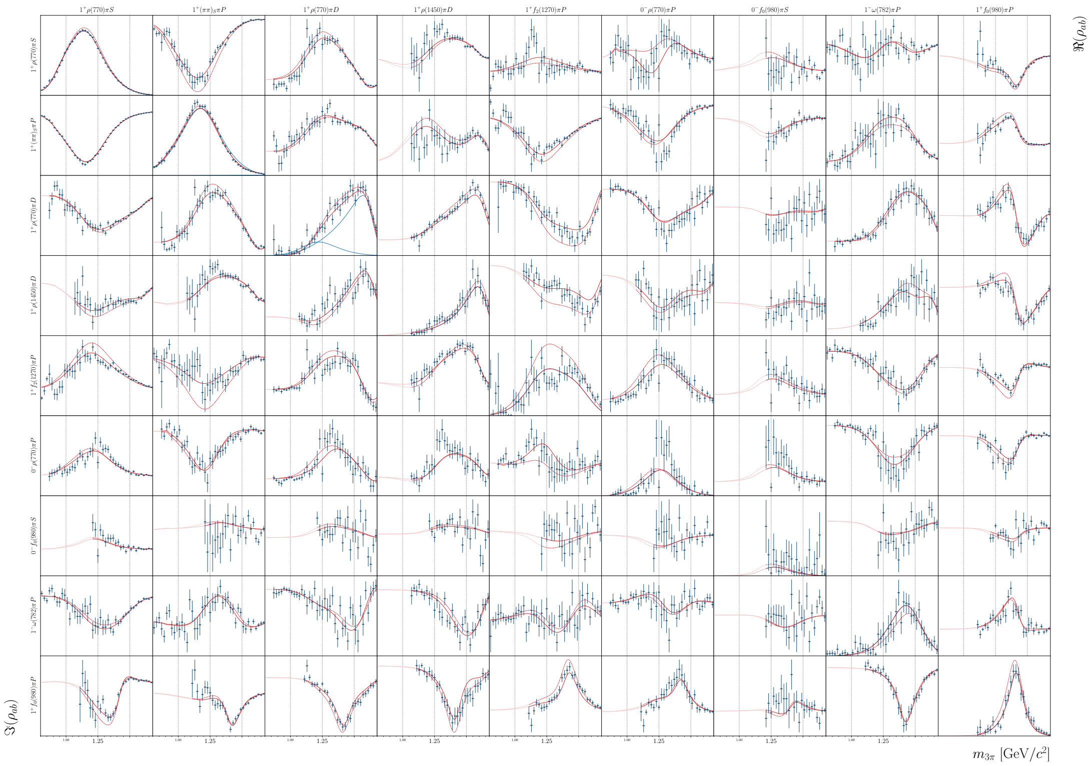

Figure B.9: Same as fig. A.1, but for the study *BW of TS* fitted with a Breit–Wigner component in the $1^+ f_0(980)\pi P$ wave.

Table B.10: Same as table B.1, but for the *BW of TS* study fitted with a triangle singularity component.

resonance	m_0 [MeV/c^2]	Γ_0 [MeV/c^2]
$a_1(1260)$	1228.6 ± 0.4	429.5 ± 0.9
$a_1(1640)$	1639.8 ± 2.6	241 ± 5
$\pi(1300)$	1318 ± 8	355 ± 19
$\rho(1450)$	1441 ± 12	390 ± 40

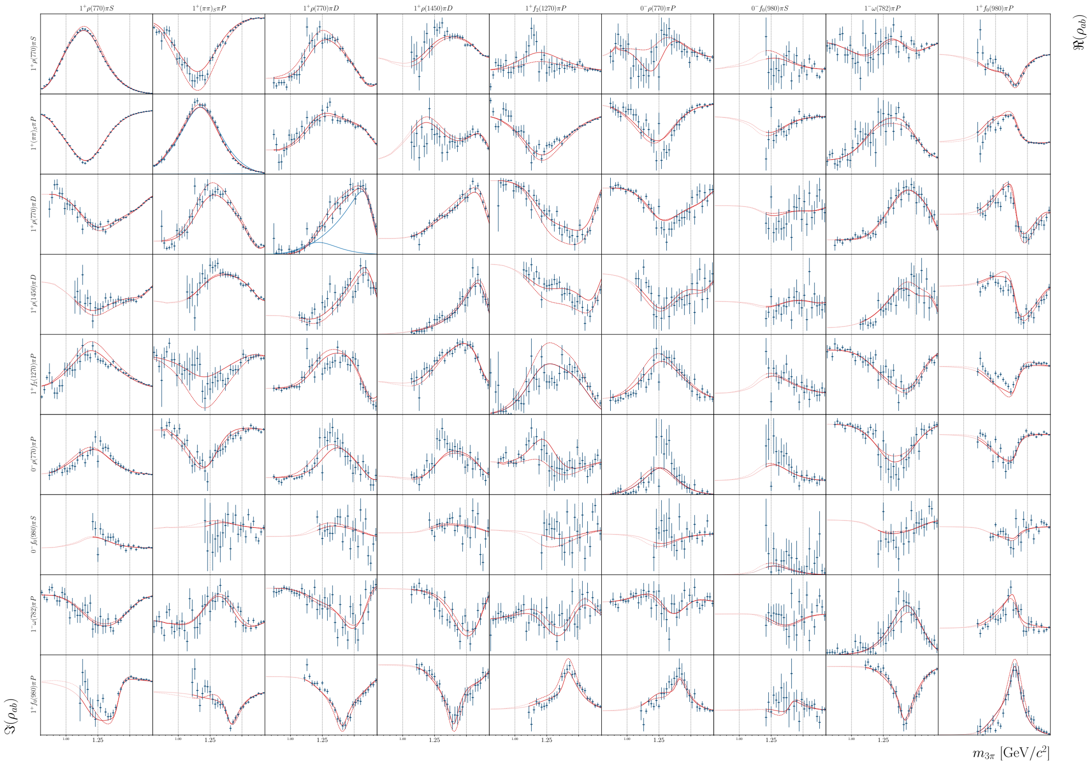

Figure B.10: Same as fig. A.1, but for the study *BW of TS* fitted with a triangle singularity component in the $1^+ f_0(980)\pi P$ wave.

Table B.11: Same as table B.1, but for the *BW of TS 10x* study fitted with a Breit–Wigner component.

resonance	m_0 [MeV/c^2]	Γ_0 [MeV/c^2]
$a_1(1260)$	1228.4 ± 0.4	425.6 ± 1.1
$a_1(1420)$	1430.8 ± 1.0	168.3 ± 2.2
$a_1(1640)$	1646.9 ± 3.5	271 ± 7
$\pi(1300)$	1314 ± 12	383 ± 28
$\rho(1450)$	1464 ± 19	550 ± 50

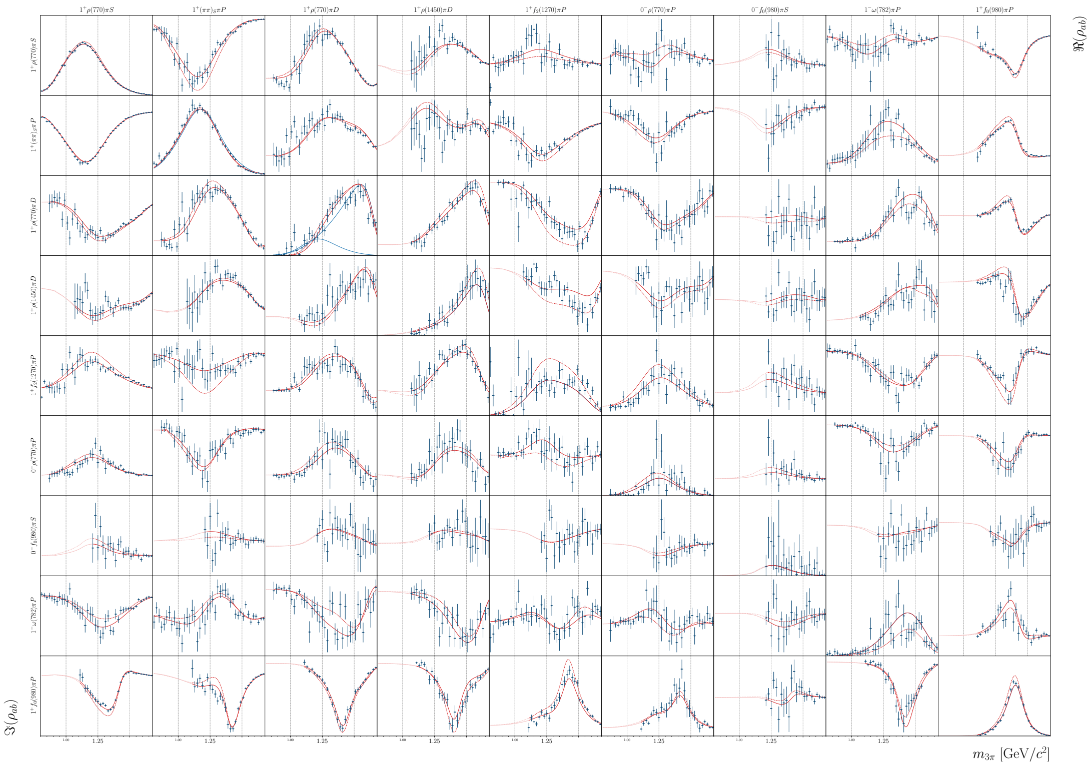

Figure B.11: Same as fig. A.1, but for the study *BW of TS 10x* fitted with a Breit–Wigner component in the $1^+ f_0(980)\pi P$ wave.

Table B.12: Same as table B.1, but for the *BW of TS 10x* study fitted with a triangle singularity component.

resonance	m_0 [MeV/c^2]	Γ_0 [MeV/c^2]
$a_1(1260)$	1230.1 ± 0.4	428.3 ± 1.1
$a_1(1640)$	1644 ± 4	306 ± 7
$\pi(1300)$	1309 ± 11	366 ± 26
$\rho(1450)$	1480 ± 18	490 ± 60

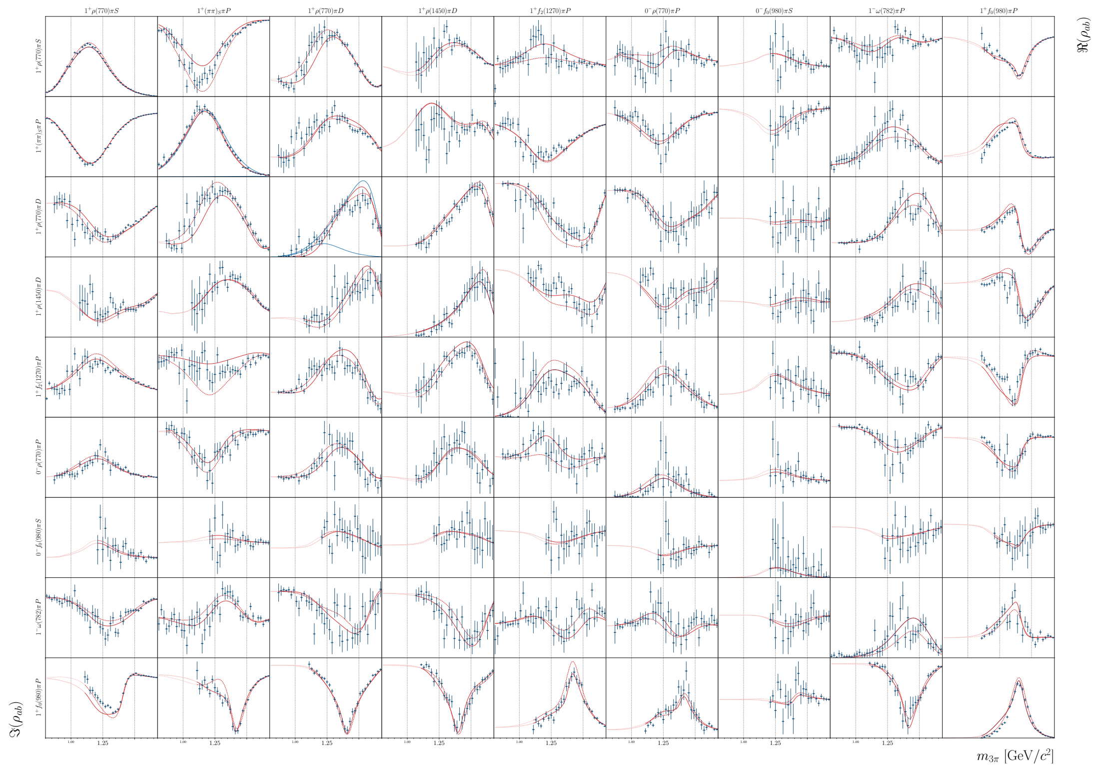

Figure B.12: Same as fig. A.1, but for the study *BW of TS 10x* fitted with a triangle singularity component in the $1^+ f_0(980)\pi P$ wave.

B.2 Sensitivity to a Mass Offset of the $a_1(1420)$

Table B.13: Same as table B.1, but for the *Mass Up* study fitted with a Breit–Wigner component.

resonance	m_0 [MeV/c^2]	Γ_0 [MeV/c^2]
$a_1(1260)$	1228.4 ± 0.4	429.8 ± 0.9
$a_1(1420)$	1471.2 ± 2.8	179 ± 5
$a_1(1640)$	1655.2 ± 3.2	272 ± 6
$\pi(1300)$	1329 ± 10	395 ± 25
$\rho(1450)$	1449 ± 8	317 ± 27

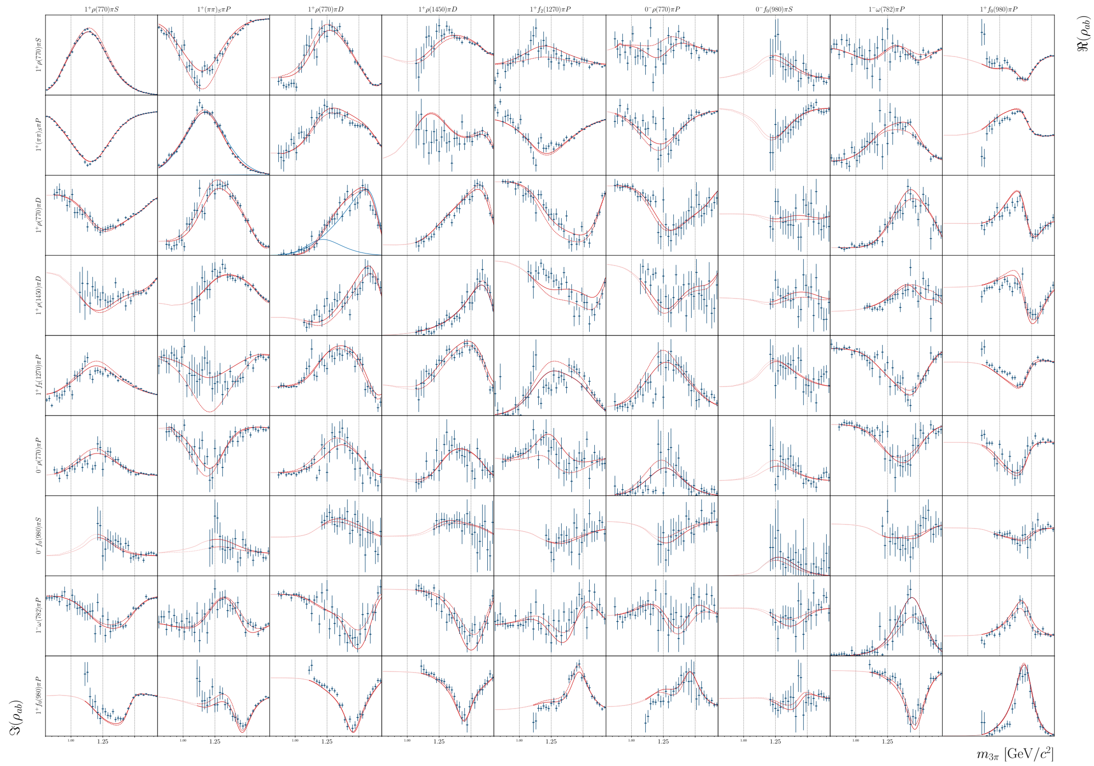

Figure B.13: Same as fig. A.1, but for the study *Mass Up* fitted with a Breit–Wigner component in the $1^+ f_0(980)\pi P$ wave.

Table B.14: Same as table B.1, but for the *Mass Up* study fitted with a triangle singularity component.

resonance	m_0 [MeV/c^2]	Γ_0 [MeV/c^2]
$a_1(1260)$	1228.8 ± 0.4	430.7 ± 0.9
$a_1(1640)$	1648.5 ± 3.1	272 ± 6
$\pi(1300)$	1330 ± 11	393 ± 26
$\rho(1450)$	1446 ± 8	289 ± 27

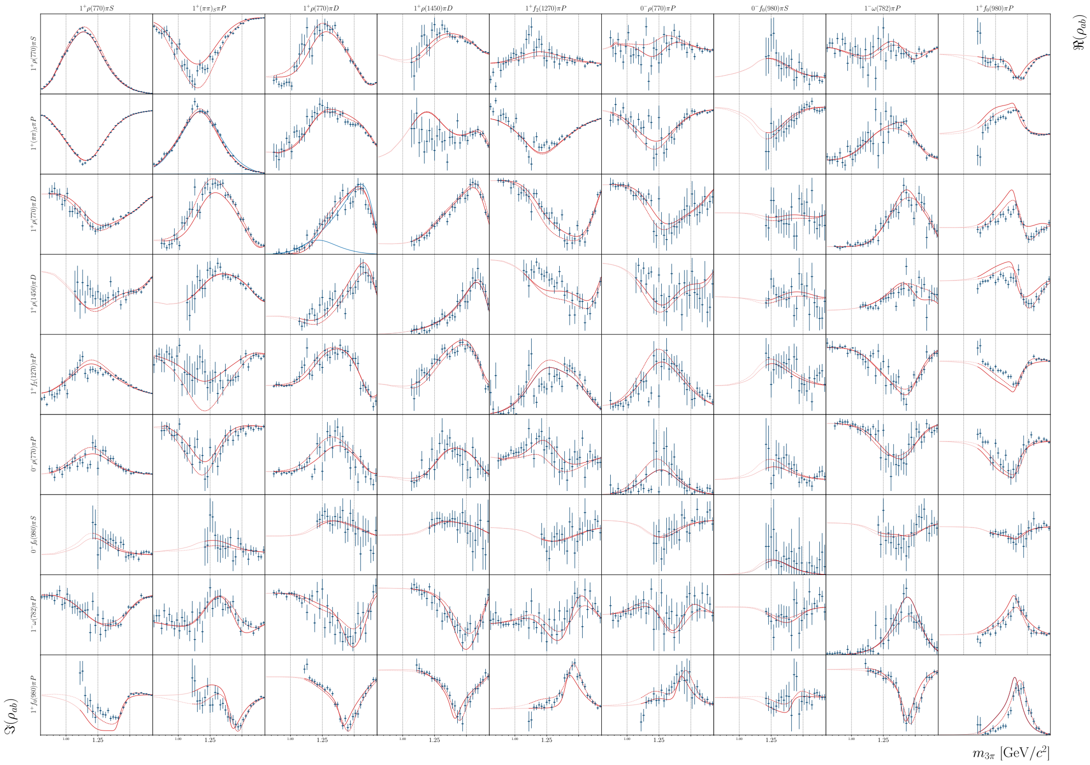

Figure B.14: Same as fig. A.1, but for the study *Mass Up* fitted with a triangle singularity component in the $1^+ f_0(980)\pi P$ wave.

Table B.15: Same as table B.1, but for the *Mass Up 10x* study fitted with a Breit–Wigner component.

resonance	m_0 [MeV/c^2]	Γ_0 [MeV/c^2]
$a_1(1260)$	1227.0 ± 0.5	424.8 ± 1.3
$a_1(1420)$	1476.6 ± 1.4	178.6 ± 2.9
$a_1(1640)$	1643 ± 4	252 ± 8
$\pi(1300)$	1323 ± 15	349 ± 35
$\rho(1450)$	1477 ± 13	350 ± 40

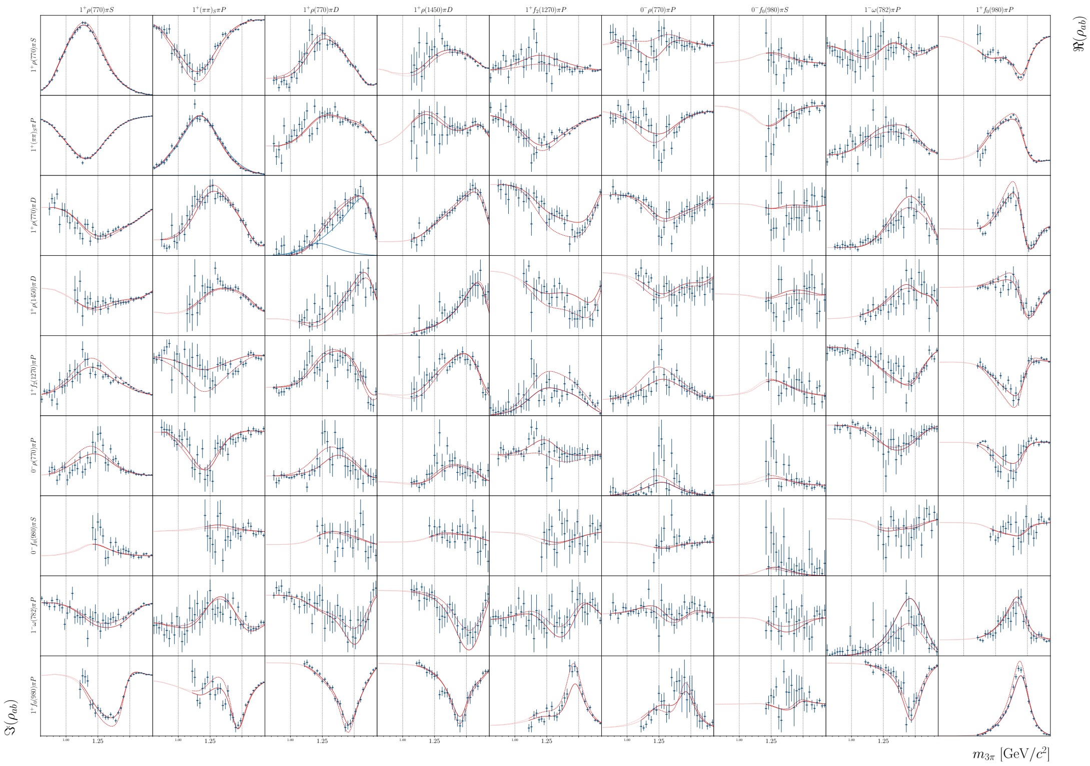

Figure B.15: Same as fig. A.1, but for the study *Mass Up 10x* fitted with a Breit–Wigner component in the $1^+ f_0(980)\pi P$ wave.

Table B.16: Same as table B.1, but for the *Mass Up 10x* study fitted with a triangle singularity component.

resonance	m_0 [MeV/c^2]	Γ_0 [MeV/c^2]
$a_1(1260)$	1230.6 ± 0.5	432.3 ± 1.3
$a_1(1640)$	1622 ± 4	257 ± 7
$\pi(1300)$	1332 ± 17	340 ± 40
$\rho(1450)$	1464 ± 9	270 ± 40

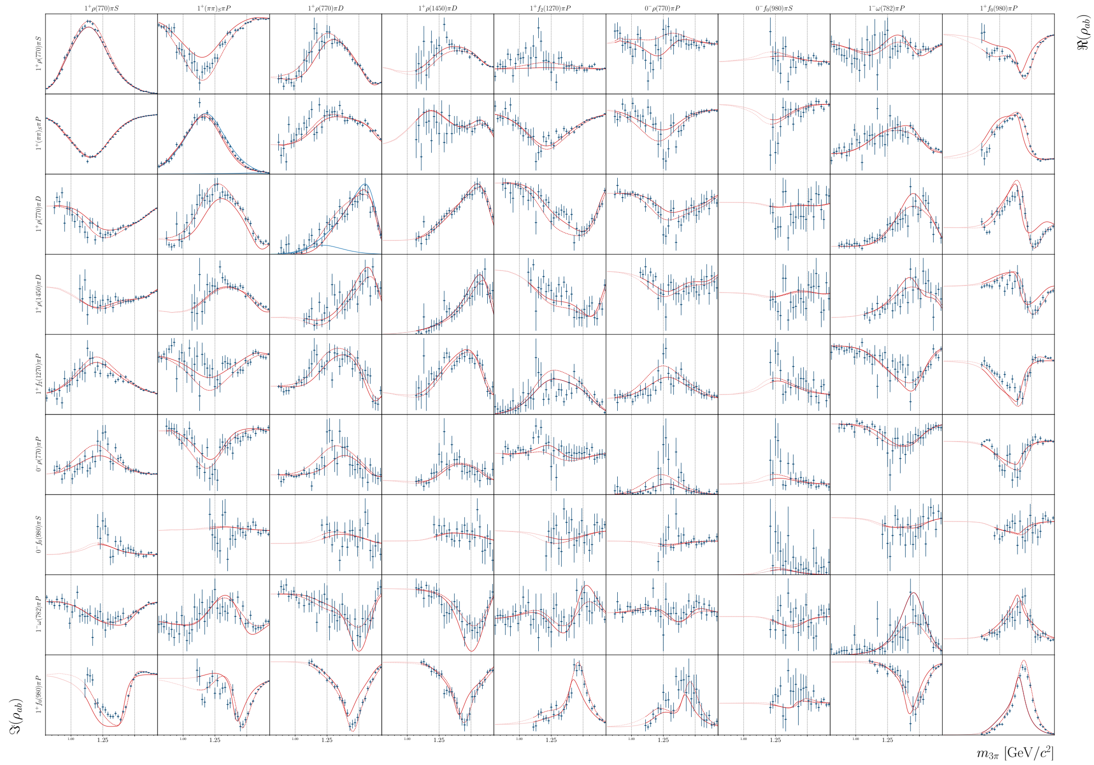

Figure B.16: Same as fig. A.1, but for the study *Mass Up 10x* fitted with a triangle singularity component in the $1^+ f_0(980)\pi P$ wave.

Table B.17: Same as table B.1, but for the *Mass Down* study fitted with a Breit–Wigner component.

resonance	m_0 [MeV/c^2]	Γ_0 [MeV/c^2]
$a_1(1260)$	1228.0 ± 0.4	429.3 ± 0.9
$a_1(1420)$	1412.4 ± 3.1	207 ± 7
$a_1(1640)$	1645.5 ± 3.0	276 ± 6
$\pi(1300)$	1323 ± 10	404 ± 23
$\rho(1450)$	1439 ± 9	343 ± 28

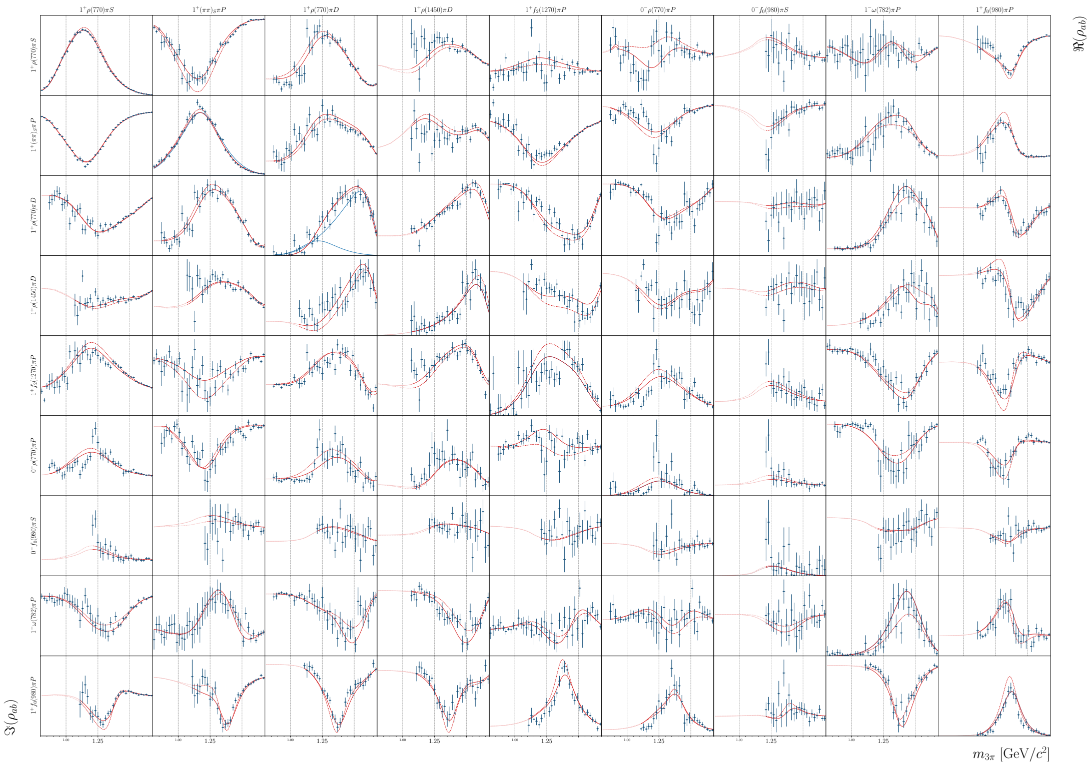

Figure B.17: Same as fig. A.1, but for the study *Mass Down* fitted with a Breit–Wigner component in the $1^+ f_0(980)\pi P$ wave.

Table B.18: Same as table B.1, but for the *Mass Down* study fitted with a triangle singularity component.

resonance	m_0 [MeV/c^2]	Γ_0 [MeV/c^2]
$a_1(1260)$	1228.0 ± 0.4	429.0 ± 0.9
$a_1(1640)$	1646.3 ± 3.0	282 ± 6
$\pi(1300)$	1321 ± 10	407 ± 23
$\rho(1450)$	1435 ± 9	340 ± 27

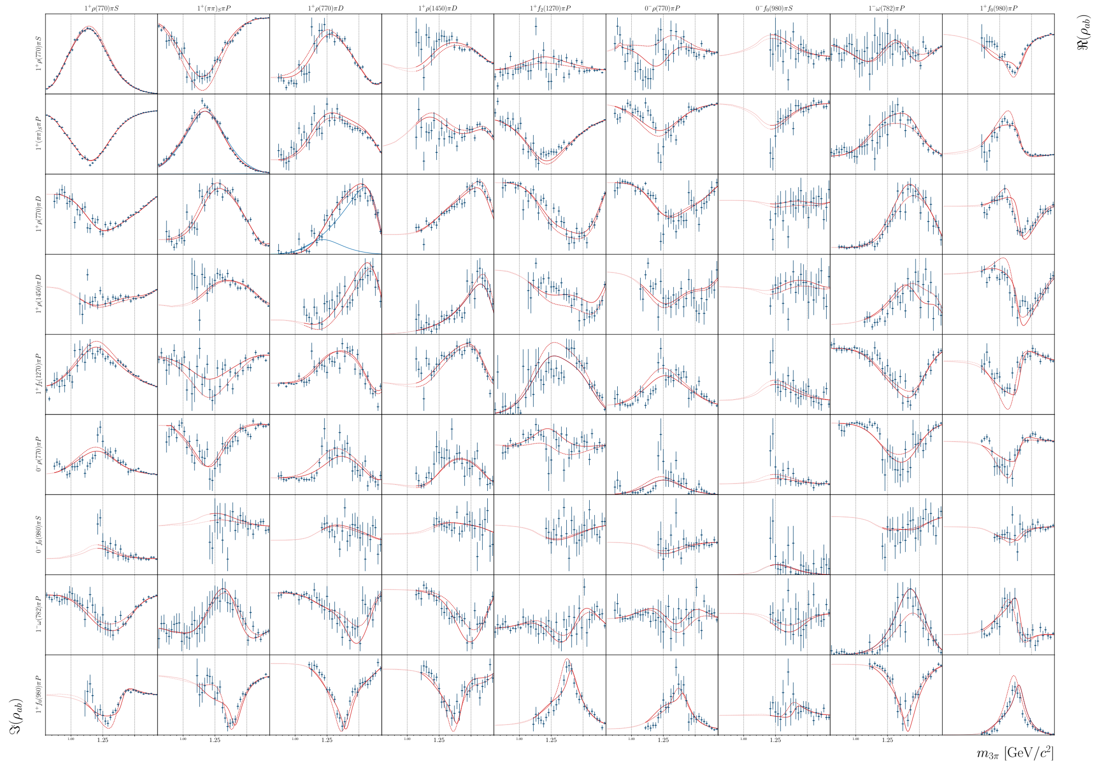

Figure B.18: Same as fig. A.1, but for the study *Mass Down* fitted with a triangle singularity component in the $1^+ f_0(980)\pi P$ wave.

Table B.19: Same as table B.1, but for the *Mass Down 10x* study fitted with a Breit–Wigner component.

resonance	m_0 [MeV/c^2]	Γ_0 [MeV/c^2]
$a_1(1260)$	1227.9 ± 0.4	424.4 ± 1.0
$a_1(1420)$	1392.7 ± 1.0	184.7 ± 2.3
$a_1(1640)$	1647.0 ± 3.3	266 ± 6
$\pi(1300)$	1329 ± 12	353 ± 26
$\rho(1450)$	1432 ± 12	370 ± 40

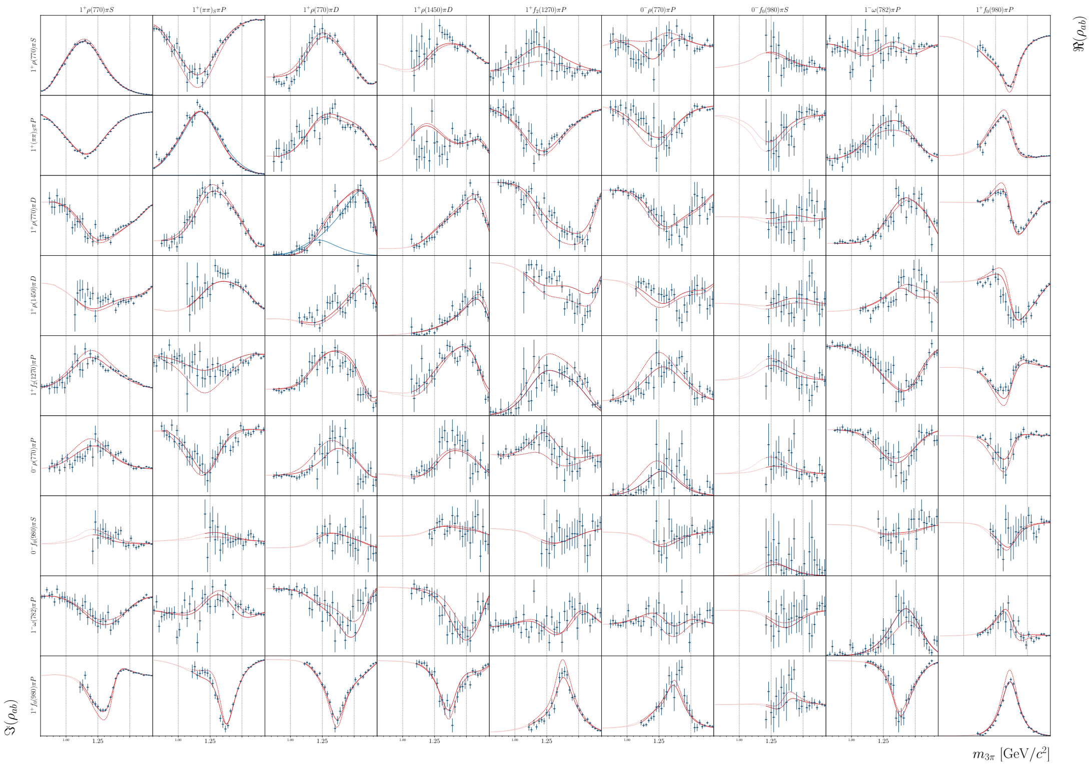

Figure B.19: Same as fig. A.1, but for the study *Mass Down 10x* fitted with a Breit–Wigner component in the $1^+ f_0(980)\pi P$ wave.

Table B.20: Same as table B.1, but for the *Mass Down 10x* study fitted with a triangle singularity component.

resonance	m_0 [MeV/c^2]	Γ_0 [MeV/c^2]
$a_1(1260)$	1227.6 ± 0.4	420.8 ± 1.0
$a_1(1640)$	1653.5 ± 3.5	284 ± 7
$\pi(1300)$	1325 ± 12	373 ± 27
$\rho(1450)$	1420 ± 12	365 ± 34

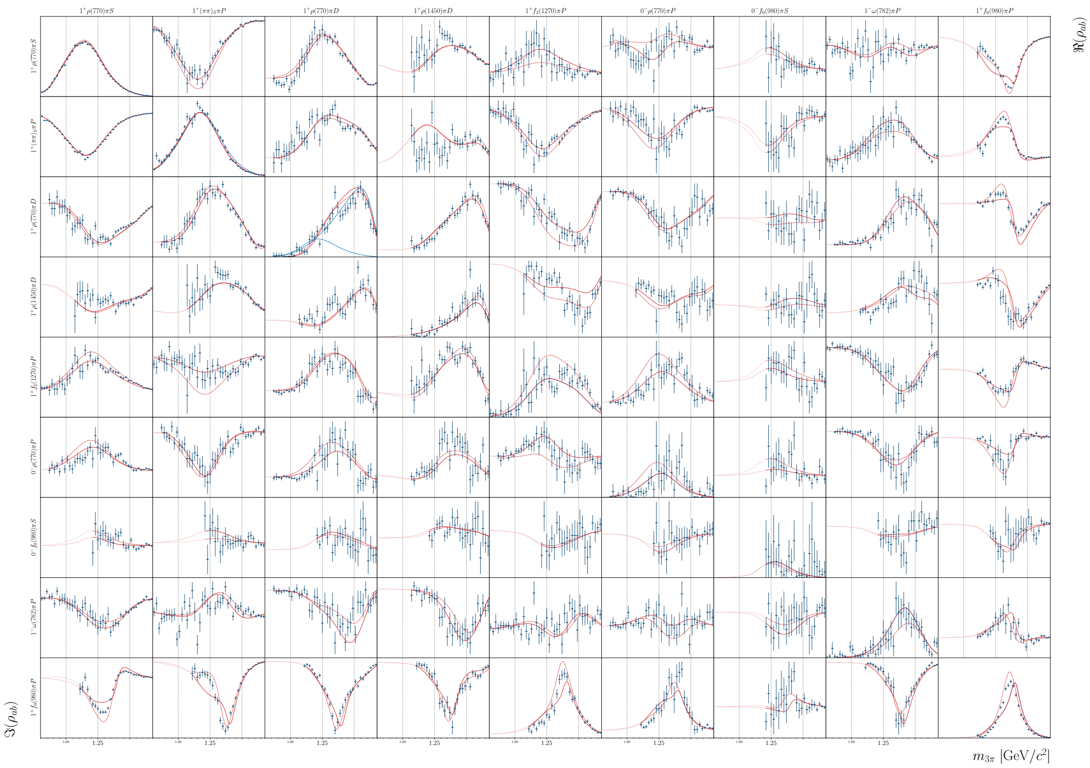

Figure B.20: Same as fig. A.1, but for the study *Mass Down 10x* fitted with a triangle singularity component in the $1^+ f_0(980)\pi P$ wave.

B.3 Sensitivity to a Width Offset of the $a_1(1420)$

Table B.21: Same as table B.1, but for the *Width Up* study fitted with a Breit–Wigner component.

resonance	m_0 [MeV/c^2]	Γ_0 [MeV/c^2]
$a_1(1260)$	1226.9 ± 0.4	426.2 ± 0.9
$a_1(1420)$	1444 ± 4	219 ± 8
$a_1(1640)$	1644.1 ± 2.7	249 ± 5
$\pi(1300)$	1329 ± 9	367 ± 21
$\rho(1450)$	1451 ± 9	377 ± 34

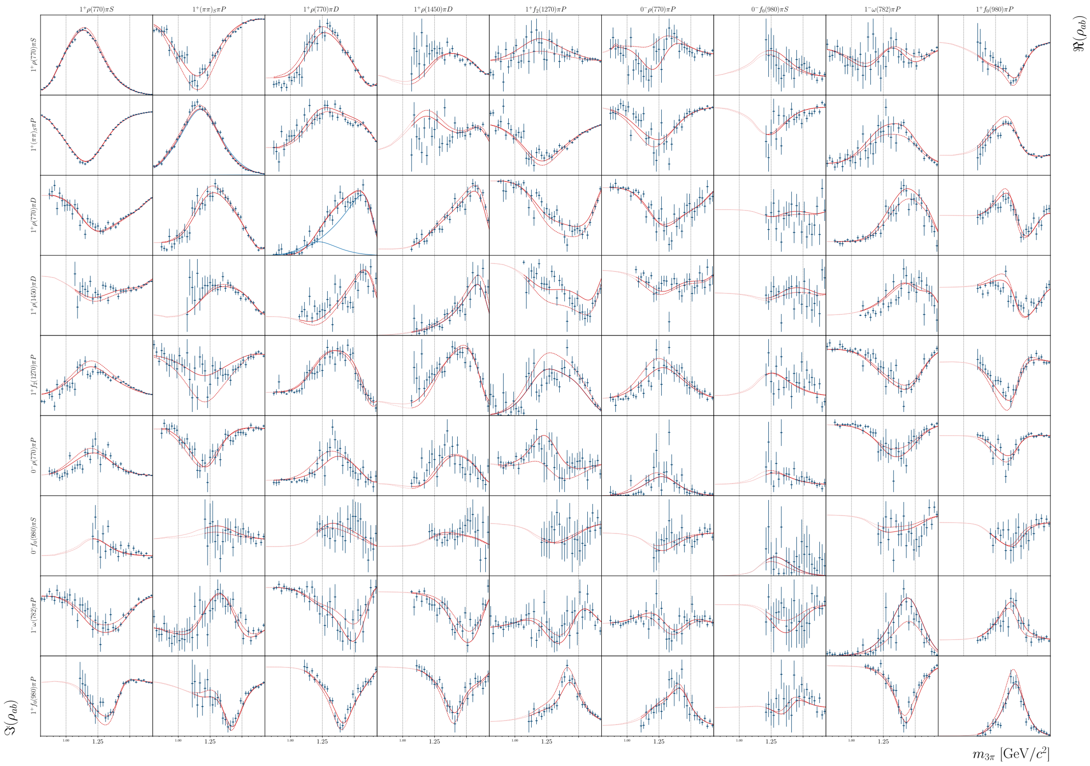

Figure B.21: Same as fig. A.1, but for the study *Width Up* fitted with a Breit–Wigner component in the $1^+ f_0(980)\pi P$ wave.

Table B.22: Same as table B.1, but for the *Width Up* study fitted with a triangle singularity component.

resonance	m_0 [MeV/c^2]	Γ_0 [MeV/c^2]
$a_1(1260)$	1227.1 ± 0.4	426.4 ± 0.9
$a_1(1640)$	1642.9 ± 2.7	255 ± 5
$\pi(1300)$	1329 ± 10	367 ± 22
$\rho(1450)$	1450 ± 9	356 ± 33

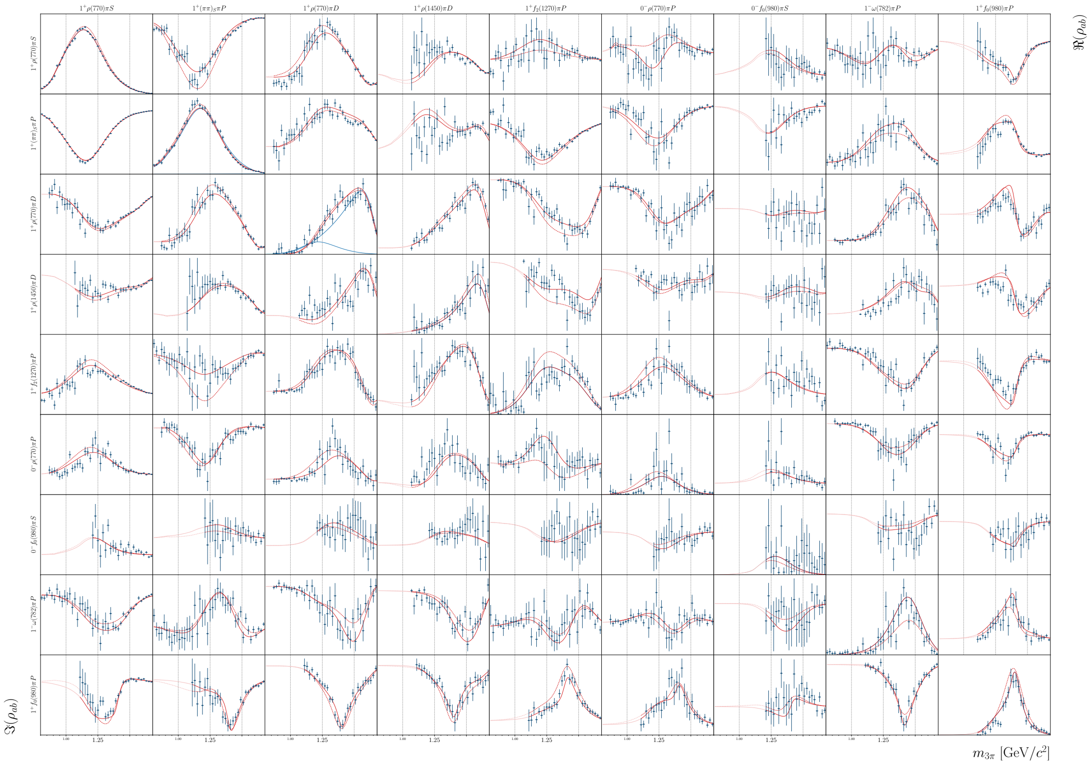

Figure B.22: Same as fig. A.1, but for the study *Width Up* fitted with a triangle singularity component in the $1^+ f_0(980)\pi P$ wave.

Table B.23: Same as table B.1, but for the *Width Up 10x* study fitted with a Breit–Wigner component.

resonance	m_0 [MeV/c^2]	Γ_0 [MeV/c^2]
$a_1(1260)$	1227.9 ± 0.4	424.7 ± 1.0
$a_1(1420)$	1431.8 ± 1.3	228.4 ± 2.8
$a_1(1640)$	1649.1 ± 3.4	280 ± 6
$\pi(1300)$	1307 ± 9	340 ± 22
$\rho(1450)$	1470 ± 9	290 ± 28

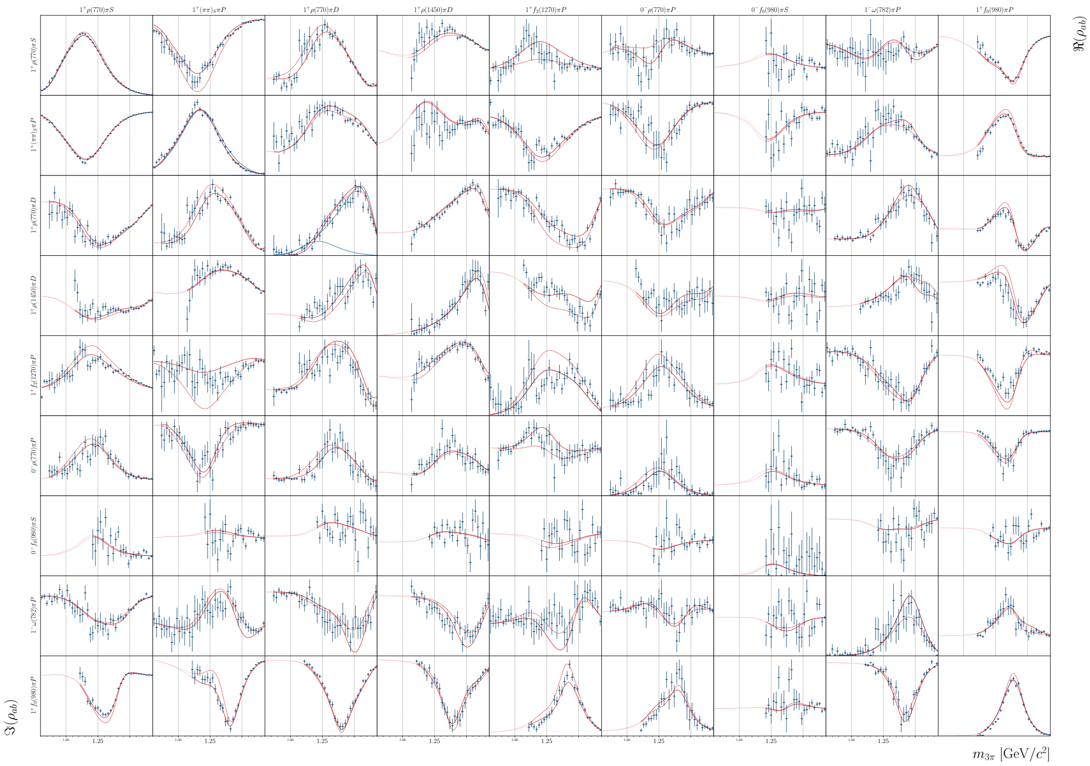

Figure B.23: Same as fig. A.1, but for the study *Width Up 10x* fitted with a Breit–Wigner component in the $1^+ f_0(980)\pi P$ wave.

Table B.24: Same as table B.1, but for the *Width Up 10x* study fitted with a triangle singularity component.

resonance	m_0 [MeV/c^2]	Γ_0 [MeV/c^2]
$a_1(1260)$	1228.9 ± 0.4	425.4 ± 1.0
$a_1(1640)$	1643.2 ± 3.5	307 ± 7
$\pi(1300)$	1306 ± 10	342 ± 23
$\rho(1450)$	1466 ± 7	264 ± 25

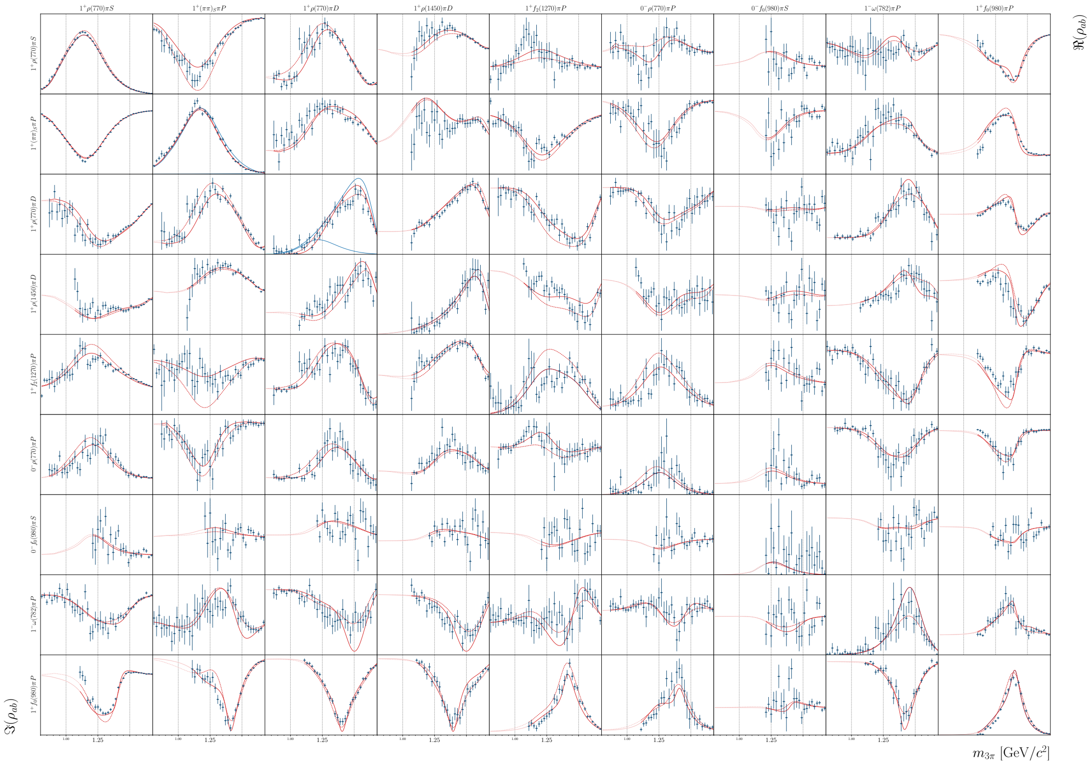

Figure B.24: Same as fig. A.1, but for the study *Width Up 10x* fitted with a triangle singularity component in the $1^+ f_0(980)\pi P$ wave.

Table B.25: Same as table B.1, but for the *Width Down* study fitted with a Breit–Wigner component.

resonance	m_0 [MeV/c^2]	Γ_0 [MeV/c^2]
$a_1(1260)$	1229.2 ± 0.4	429.9 ± 0.9
$a_1(1420)$	1429.7 ± 2.0	121 ± 4
$a_1(1640)$	1638.9 ± 2.6	236 ± 5
$\pi(1300)$	1329 ± 8	341 ± 18
$\rho(1450)$	1475 ± 16	480 ± 50

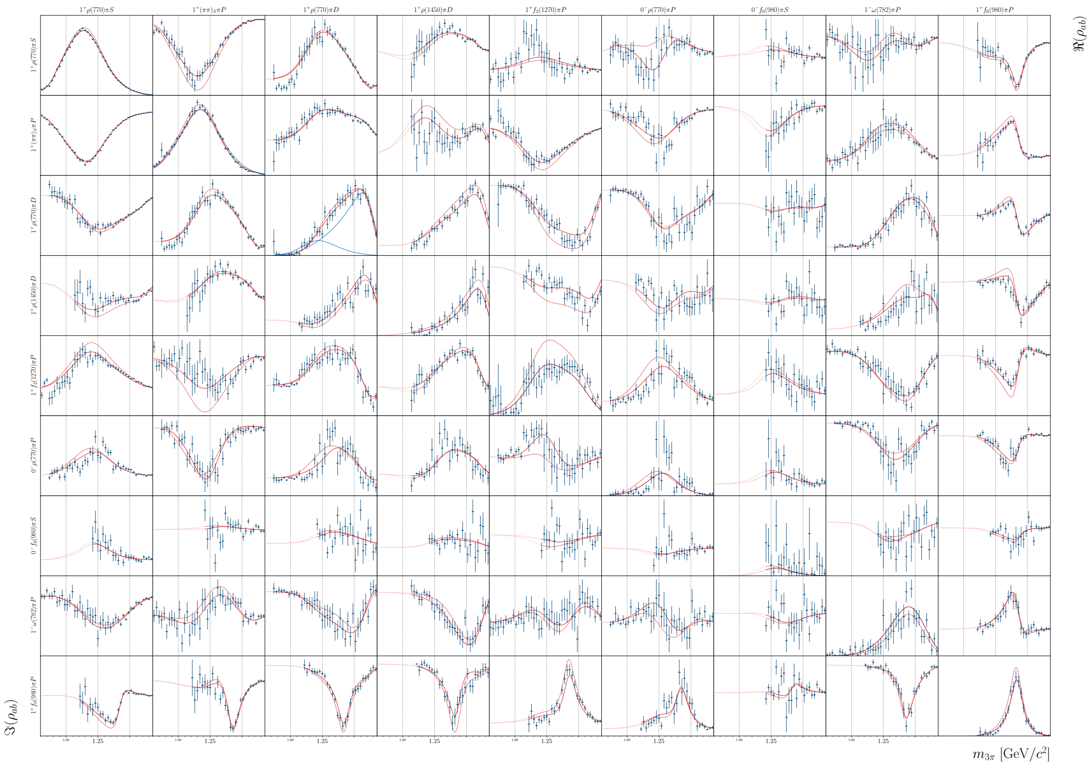

Figure B.25: Same as fig. A.1, but for the study *Width Down* fitted with a Breit–Wigner component in the $1^+ f_0(980)\pi P$ wave.

Table B.26: Same as table B.1, but for the *Width Down* study fitted with a triangle singularity component.

resonance	m_0 [MeV/c^2]	Γ_0 [MeV/c^2]
$a_1(1260)$	1229.1 ± 0.4	429.4 ± 0.9
$a_1(1640)$	1639.6 ± 2.7	247 ± 5
$\pi(1300)$	1326 ± 8	333 ± 18
$\rho(1450)$	1488 ± 14	440 ± 50

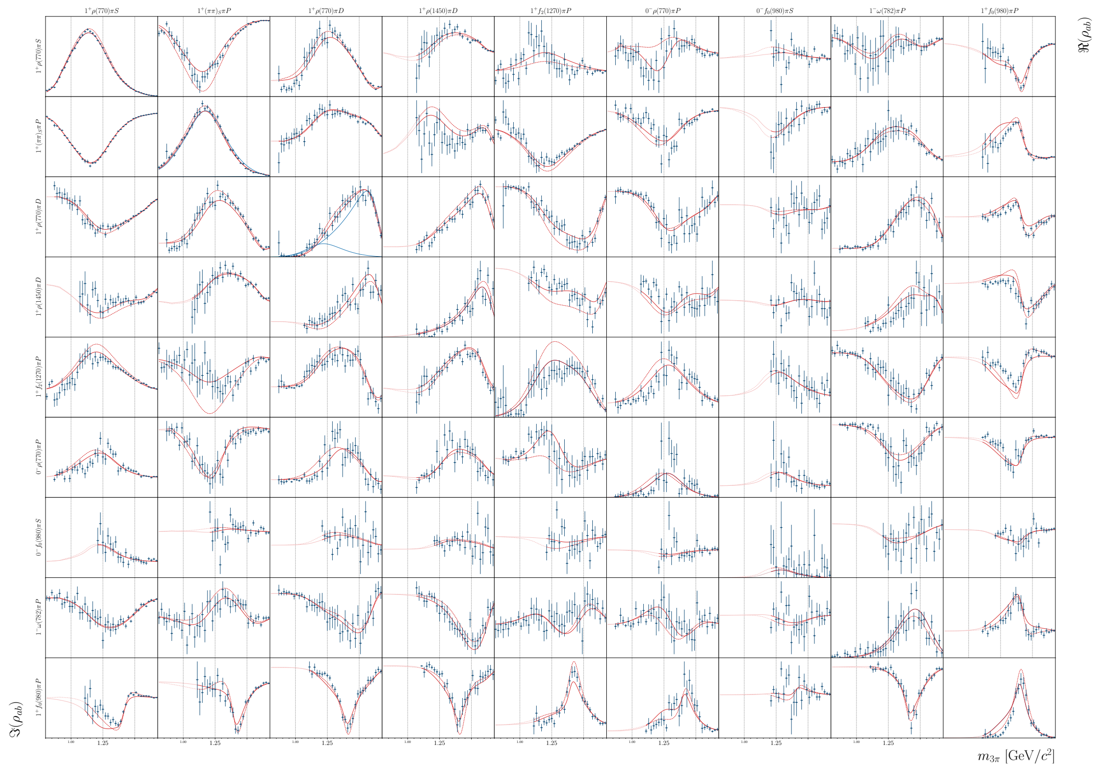

Figure B.26: Same as fig. A.1, but for the study *Width Down* fitted with a triangle singularity component in the $1^+ f_0(980)\pi P$ wave.

Table B.27: Same as table B.1, but for the *Width Down 10x* study fitted with a Breit–Wigner component.

resonance	m_0 [MeV/c^2]	Γ_0 [MeV/c^2]
$a_1(1260)$	1228.0 ± 0.5	427.8 ± 1.2
$a_1(1420)$	1428.9 ± 0.8	133.9 ± 1.8
$a_1(1640)$	1652 ± 4	289 ± 8
$\pi(1300)$	1317 ± 13	355 ± 28
$\rho(1450)$	1458 ± 15	400 ± 40

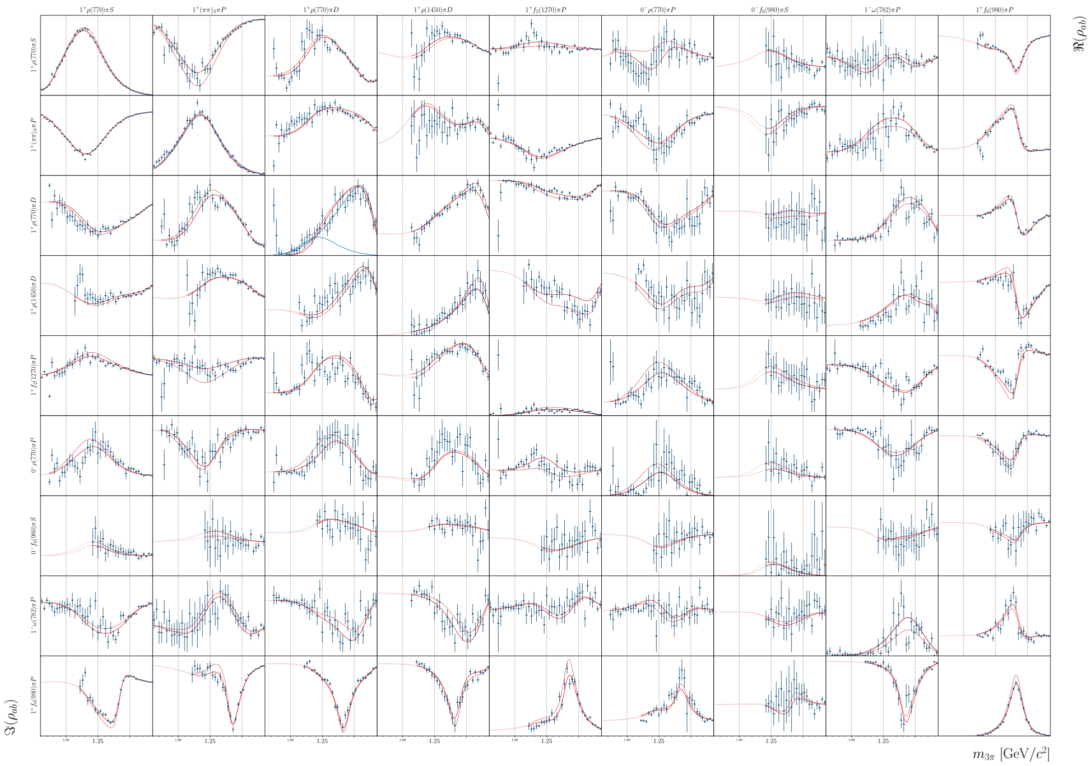

Figure B.27: Same as fig. A.1, but for the study *Width Down 10x* fitted with a Breit–Wigner component in the $1^+ f_0(980)\pi P$ wave.

Table B.28: Same as table B.1, but for the *Width Down 10x* study fitted with a triangle singularity component.

resonance	m_0 [MeV/c^2]	Γ_0 [MeV/c^2]
$a_1(1260)$	1230.2 ± 0.5	431.8 ± 1.2
$a_1(1640)$	1653 ± 5	338 ± 9
$\pi(1300)$	1310 ± 11	335 ± 25
$\rho(1450)$	1468 ± 15	380 ± 50

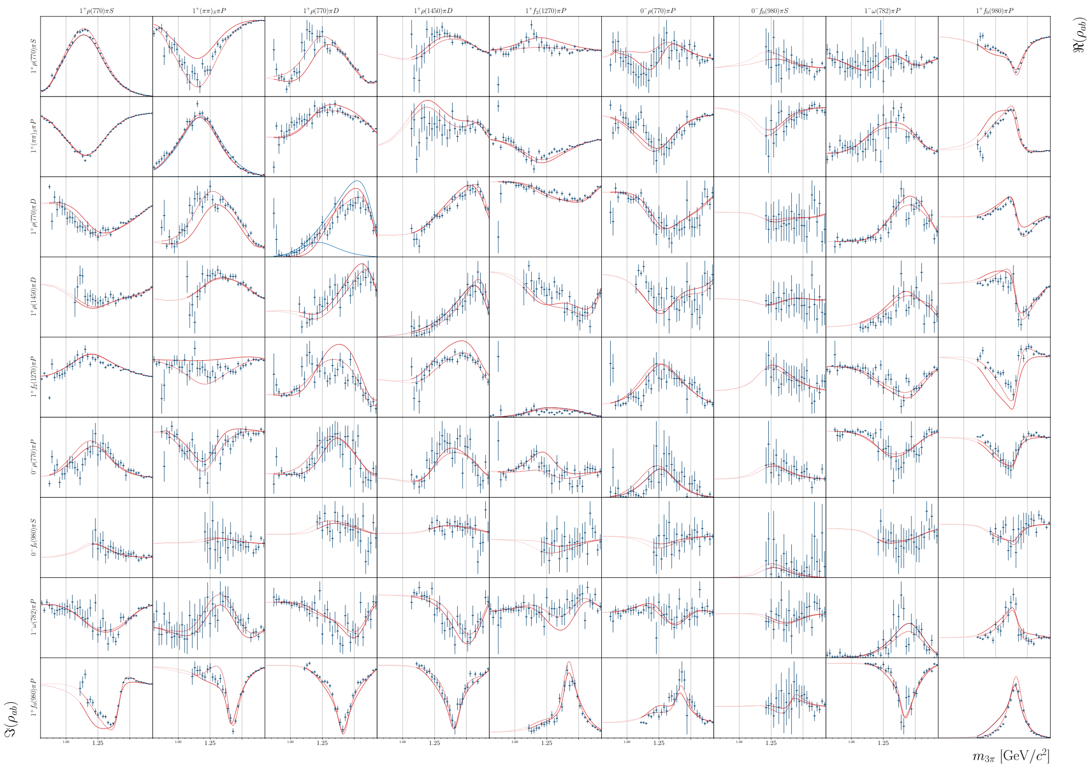

Figure B.28: Same as fig. A.1, but for the study *Width Down 10x* fitted with a triangle singularity component in the $1^+ f_0(980)\pi P$ wave.

B.4 Sensitivity Based on $a_1(1260)$ Width

Table B.29: Same as table B.1, but for the $a_1(1260)$ *Width Up* study fitted with a Breit–Wigner component.

resonance	m_0 [MeV/c^2]	Γ_0 [MeV/c^2]
$a_1(1260)$	1229.3 ± 0.6	609.5 ± 1.8
$a_1(1420)$	1429.7 ± 2.9	170 ± 7
$a_1(1640)$	1643.1 ± 2.5	229 ± 5
$\pi(1300)$	1341 ± 9	371 ± 21
$\rho(1450)$	1408 ± 16	500 ± 50

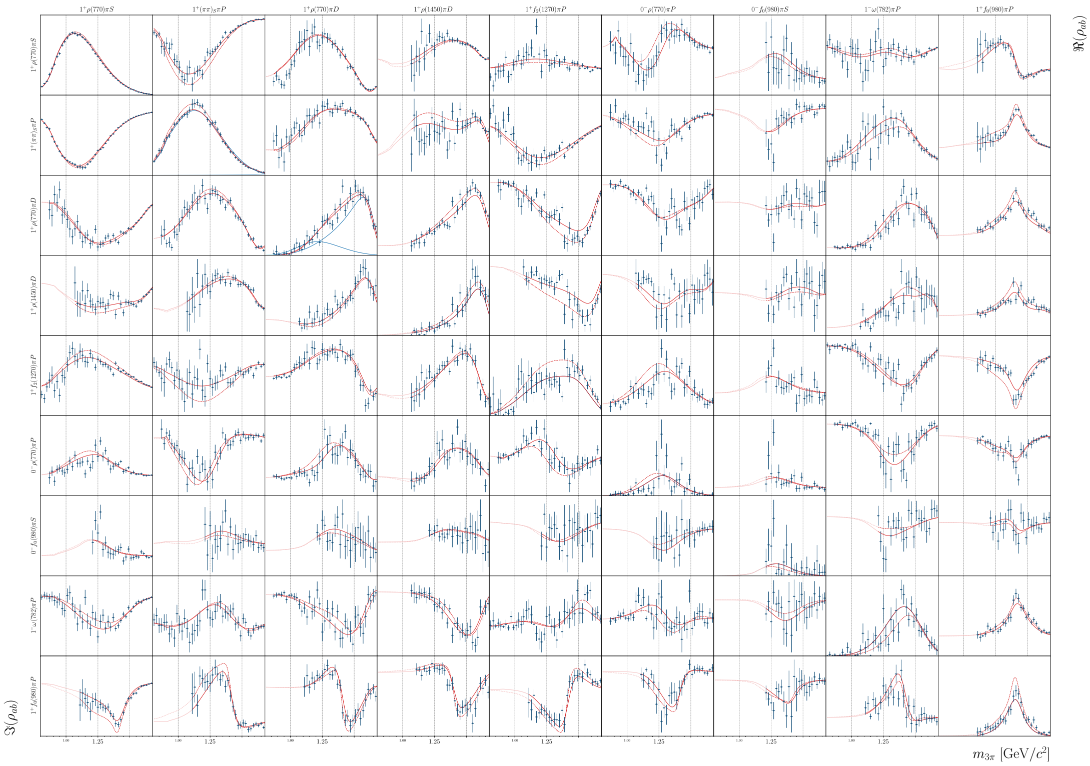

Figure B.29: Same as fig. A.1, but for the study $a_1(1260)$ *Width Up* fitted with a Breit–Wigner component in the $1^+ f_0(980)\pi P$ wave.

Table B.30: Same as table B.1, but for the $a_1(1260)$ *Width Up* study fitted with a triangle singularity component.

resonance	m_0 [MeV/c^2]	Γ_0 [MeV/c^2]
$a_1(1260)$	1229.5 ± 0.6	609.9 ± 1.7
$a_1(1640)$	1642.9 ± 2.5	230 ± 5
$\pi(1300)$	1342 ± 9	370 ± 21
$\rho(1450)$	1413 ± 16	490 ± 50

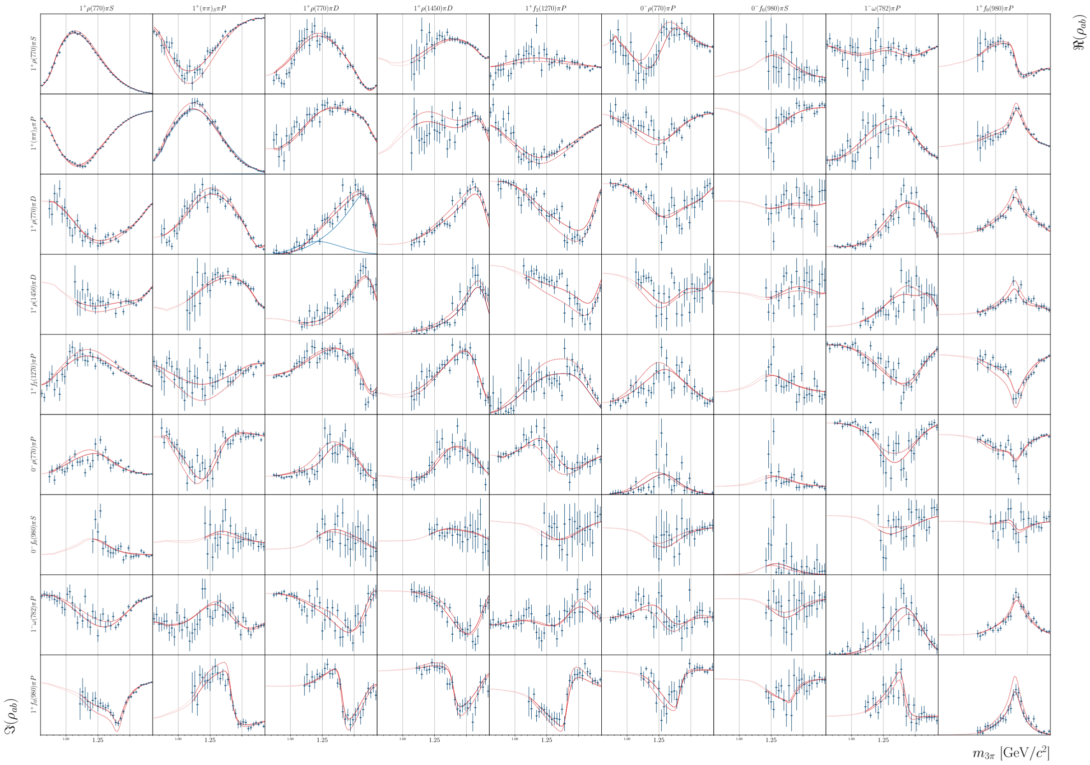

Figure B.30: Same as fig. A.1, but for the study $a_1(1260)$ *Width Up* fitted with a triangle singularity component in the $1^+ f_0(980)\pi P$ wave.

Table B.31: Same as table B.1, but for the $a_1(1260)$ *Width Up 10x* study fitted with a Breit–Wigner component.

resonance	m_0 [MeV/c^2]	Γ_0 [MeV/c^2]
$a_1(1260)$	1226.1 ± 0.7	608.9 ± 2.2
$a_1(1420)$	1441.7 ± 1.3	199.4 ± 3.1
$a_1(1640)$	1657.3 ± 3.2	204 ± 6
$\pi(1300)$	1306 ± 14	400 ± 40
$\rho(1450)$	1452 ± 17	470 ± 50

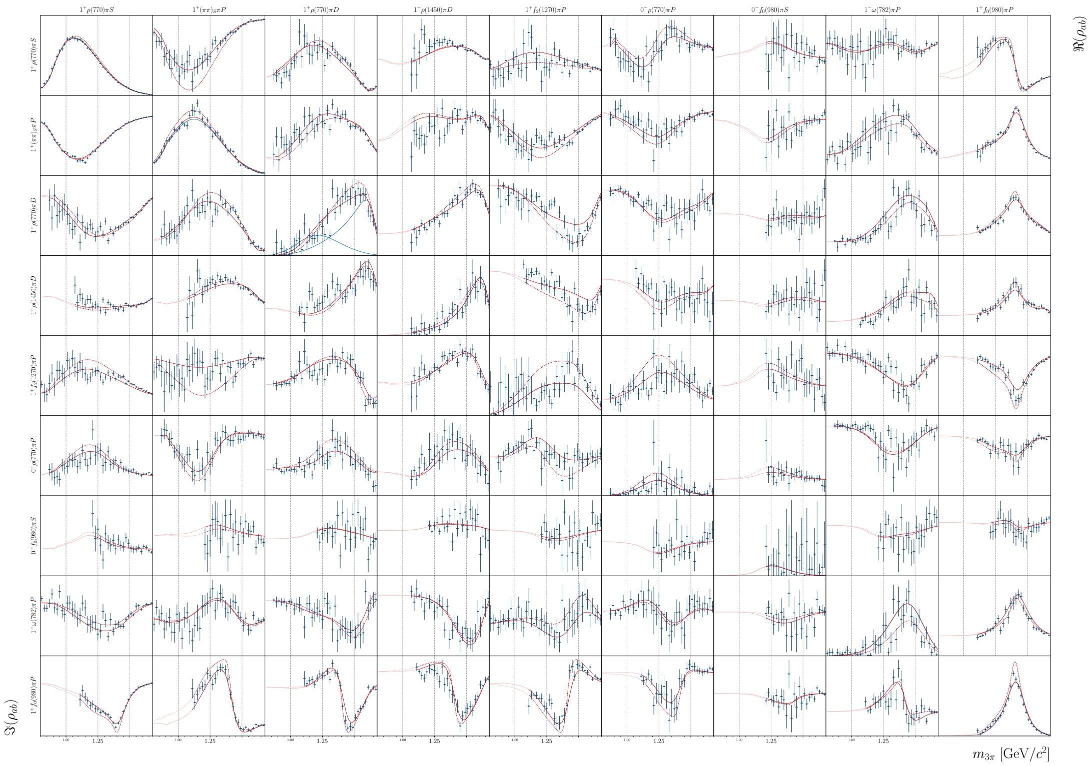

Figure B.31: Same as fig. A.1, but for the study $a_1(1260)$ *Width Up 10x* fitted with a Breit–Wigner component in the $1^+ f_0(980)\pi P$ wave.

Table B.32: Same as table B.1, but for the $a_1(1260)$ *Width Up 10x* study fitted with a triangle singularity component.

resonance	m_0 [MeV/c^2]	Γ_0 [MeV/c^2]
$a_1(1260)$	1228.0 ± 0.7	612.6 ± 2.1
$a_1(1640)$	1655.7 ± 3.2	208 ± 6
$\pi(1300)$	1309 ± 14	400 ± 40
$\rho(1450)$	1448 ± 16	450 ± 50

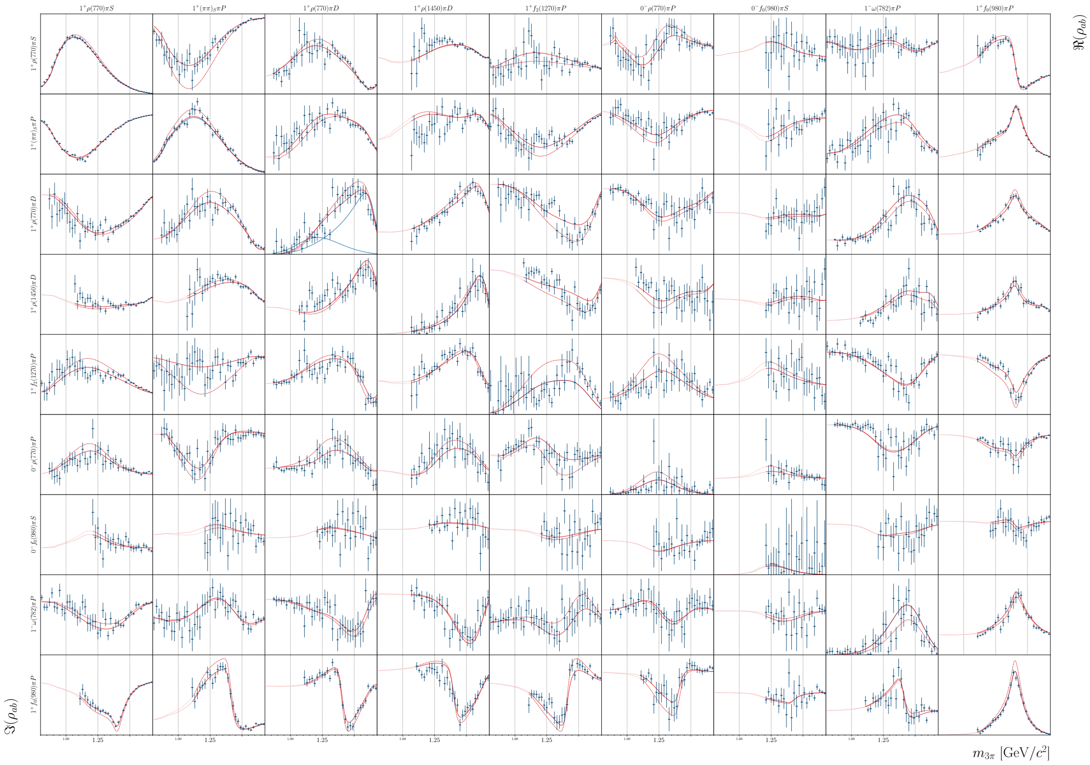

Figure B.32: Same as fig. A.1, but for the study $a_1(1260)$ *Width Up 10x* fitted with a triangle singularity component in the $1^+ f_0(980)\pi P$ wave.

Table B.33: Same as table B.1, but for the $a_1(1260)$ *Width Down* study fitted with a Breit–Wigner component.

resonance	m_0 [MeV/c^2]	Γ_0 [MeV/c^2]
$a_1(1260)$	1228.69 ± 0.17	255.7 ± 0.4
$a_1(1420)$	1408.0 ± 3.4	215 ± 8
$a_1(1640)$	1644.4 ± 2.5	228 ± 4
$\pi(1300)$	1317 ± 11	407 ± 25
$\rho(1450)$	1469 ± 12	380 ± 40

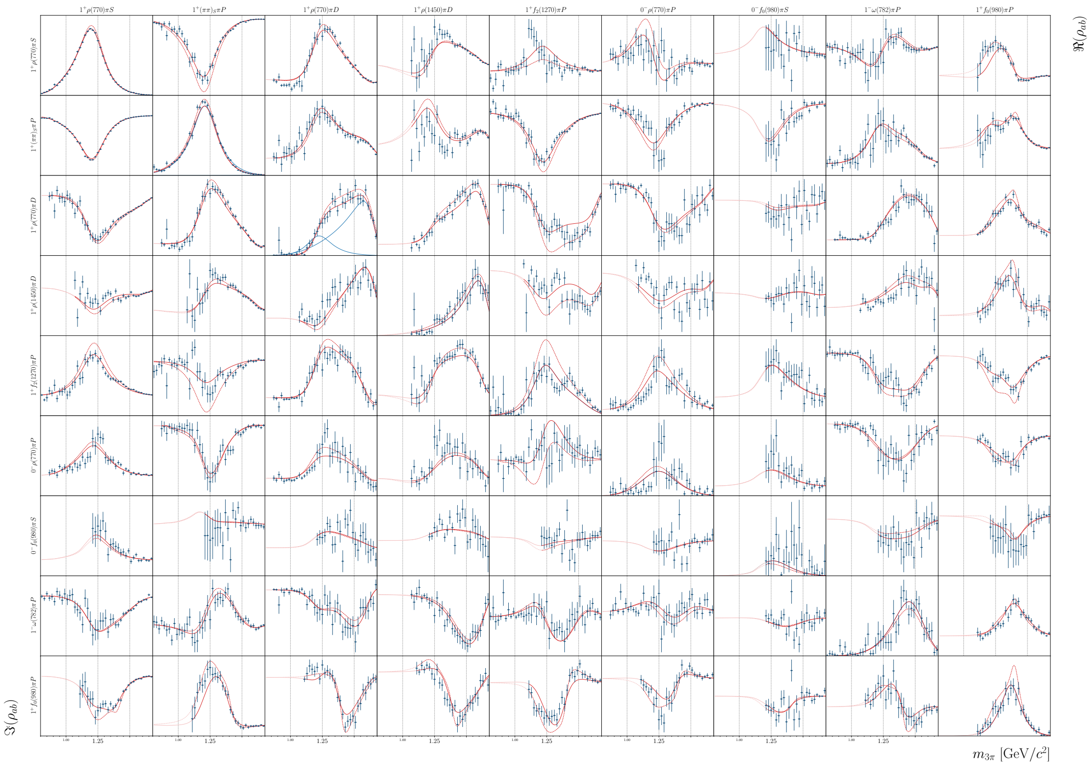

Figure B.33: Same as fig. A.1, but for the study $a_1(1260)$ *Width Down* fitted with a Breit–Wigner component in the $1^+ f_0(980)\pi P$ wave.

Table B.34: Same as table B.1, but for the $a_1(1260)$ *Width Down* study fitted with a triangle singularity component.

resonance	m_0 [MeV/c^2]	Γ_0 [MeV/c^2]
$a_1(1260)$	1228.93 ± 0.17	256.1 ± 0.4
$a_1(1640)$	1645.8 ± 2.6	232 ± 4
$\pi(1300)$	1322 ± 11	411 ± 25
$\rho(1450)$	1475 ± 12	378 ± 35

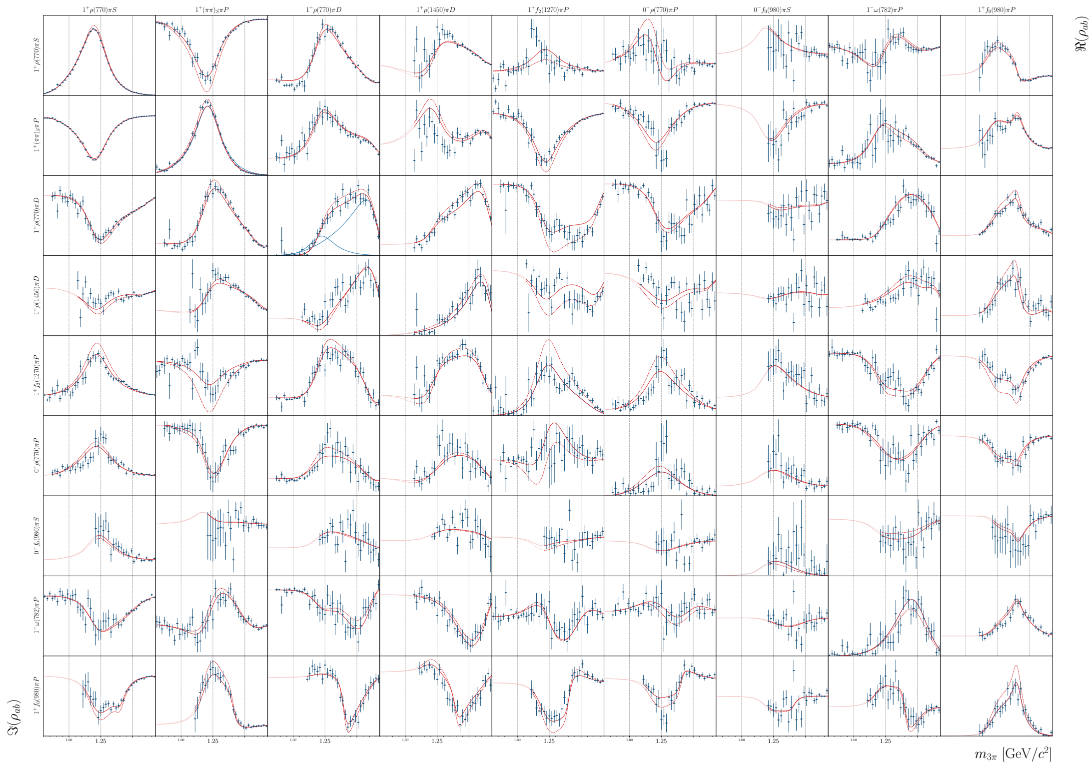

Figure B.34: Same as fig. A.1, but for the study $a_1(1260)$ *Width Down* fitted with a triangle singularity component in the $1^+ f_0(980)\pi P$ wave.

Table B.35: Same as table B.1, but for the $a_1(1260)$ *Width Down 10x* study fitted with a Breit–Wigner component.

resonance	m_0 [MeV/c^2]	Γ_0 [MeV/c^2]
$a_1(1260)$	1228.03 ± 0.20	256.1 ± 0.5
$a_1(1420)$	1404.2 ± 1.1	198.0 ± 2.8
$a_1(1640)$	1651.4 ± 2.9	193 ± 4
$\pi(1300)$	1343 ± 18	410 ± 40
$\rho(1450)$	1385 ± 15	390 ± 40

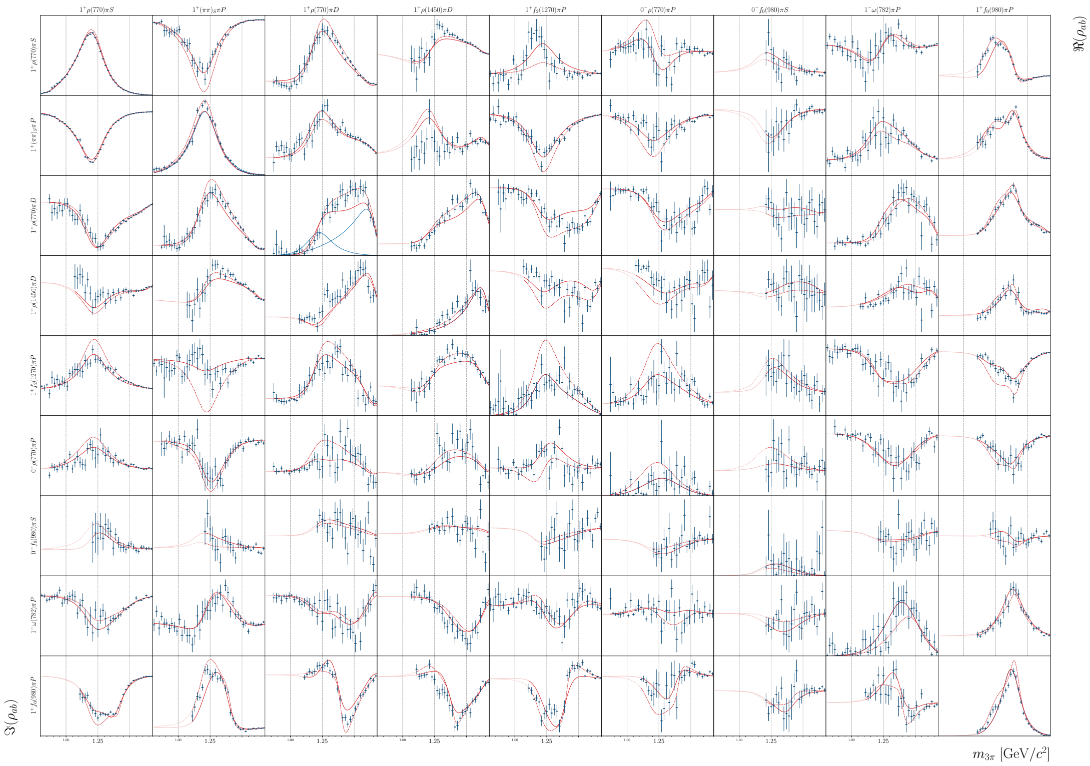

Figure B.35: Same as fig. A.1, but for the study $a_1(1260)$ *Width Down 10x* fitted with a Breit–Wigner component in the $1^+ f_0(980)\pi P$ wave.

Table B.36: Same as table B.1, but for the $a_1(1260)$ *Width Down 10x* study fitted with a triangle singularity component.

resonance	m_0 [MeV/c^2]	Γ_0 [MeV/c^2]
$a_1(1260)$	1229.11 ± 0.19	257.7 ± 0.5
$a_1(1640)$	1653.0 ± 3.2	207 ± 5
$\pi(1300)$	1360 ± 18	390 ± 35
$\rho(1450)$	1404 ± 14	380 ± 40

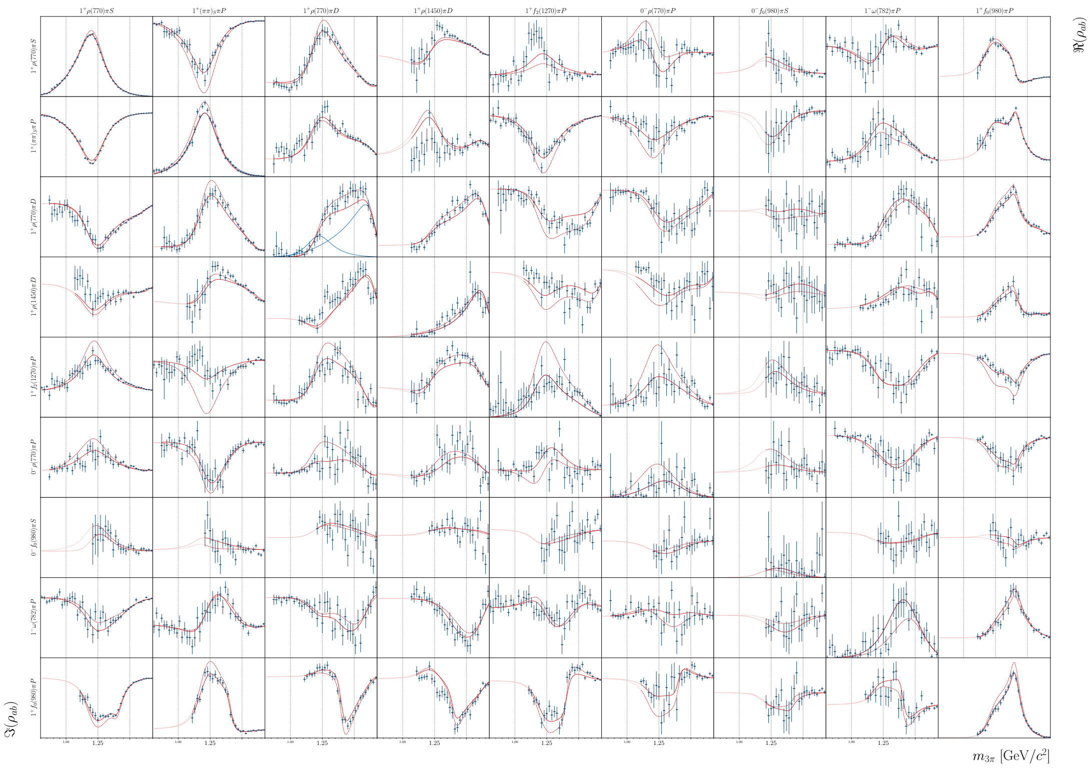

Figure B.36: Same as fig. A.1, but for the study $a_1(1260)$ *Width Down 10x* fitted with a triangle singularity component in the $1^+ f_0(980)\pi P$ wave.

C Additional Cross Checks of Correct Implementation

Chapter 10 introduced the K-matrix in the P-vector approach, which is a more sophisticated parameterization for the invariant amplitudes appearing in our decay than using a sum-of-Breit-Wigner amplitudes. In section 10.2 the resulting amplitude for several simple examples were derived. Due to the complex implementation structure of the K-matrix approach several cross checks were performed to verify the correct implementation. One cross check was already discussed in section 10.2.4. The other two cross checks are briefly described in appendices C.1 and C.2.

C.1 Cross Check for a Double Pole in a Single Channel

In order to test the examples discussed in section 10.2.2 the amplitude for the $\rho(770)$ and $\rho(1450)$ decaying into 2π were calculated. As a cross check the analytical solution of that amplitude given in eq. (10.21) was also calculated. Both these amplitudes are compared to one another in fig. C.1. The upper two plots show both the real and imaginary parts obtained from the K-matrix formalism as well as the analytic function obtained from it. Both curves overlap. Looking at the deviations plotted below, one notices that the deviation of the analytical function to the K-matrix approach is in the order of $\mathcal{O}(10^{-16})$. This means that also for this case the deviations are in the order of the precision of the 64-bit double-precision floating-point numbers used to evaluate the amplitudes.

C.2 Cross Check for a Single Pole in a Two Channels

An analogous cross check was performed for a single pole in two channels (see section 10.2.3), using the amplitude for the $f_0(980)$ decaying into the $\pi\pi$ and $K\bar{K}$ channels. Figure C.2 shows that the deviations are also in the order of $\mathcal{O}(10^{-16})$, demonstrating

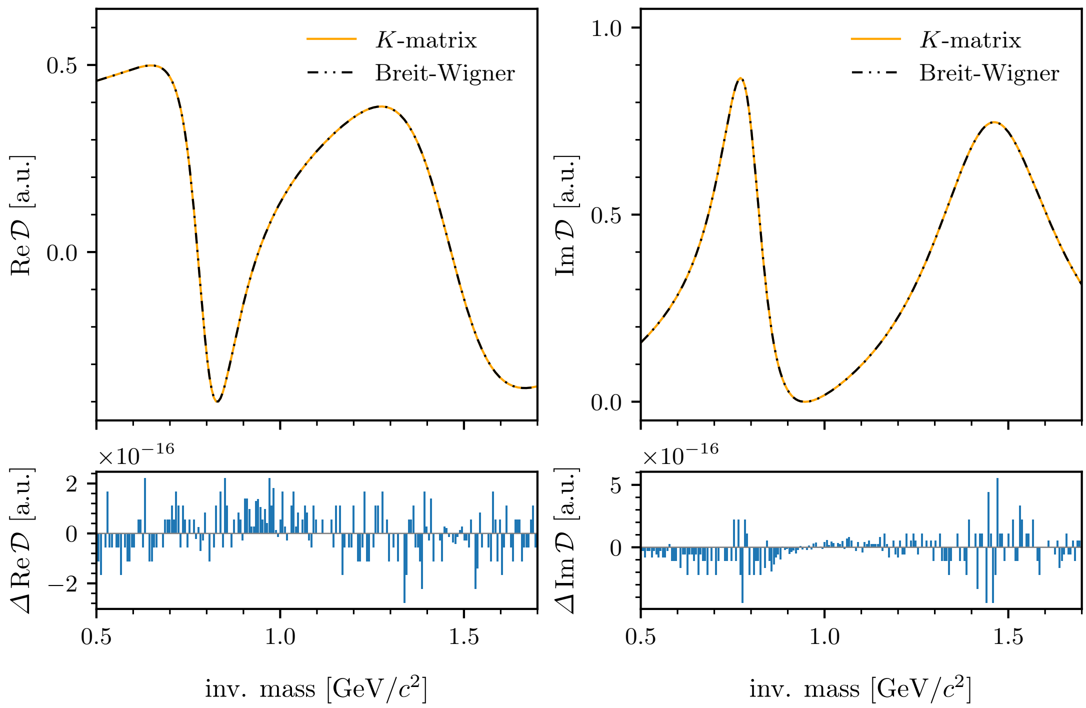

Figure C.1: Same as fig. 10.5, but for the cross check for two poles in a single channel K-matrix in the P-vector approach.

that the Flatté parameterization is reproduced up to the precision of 64-bit double-precision floating-point numbers.

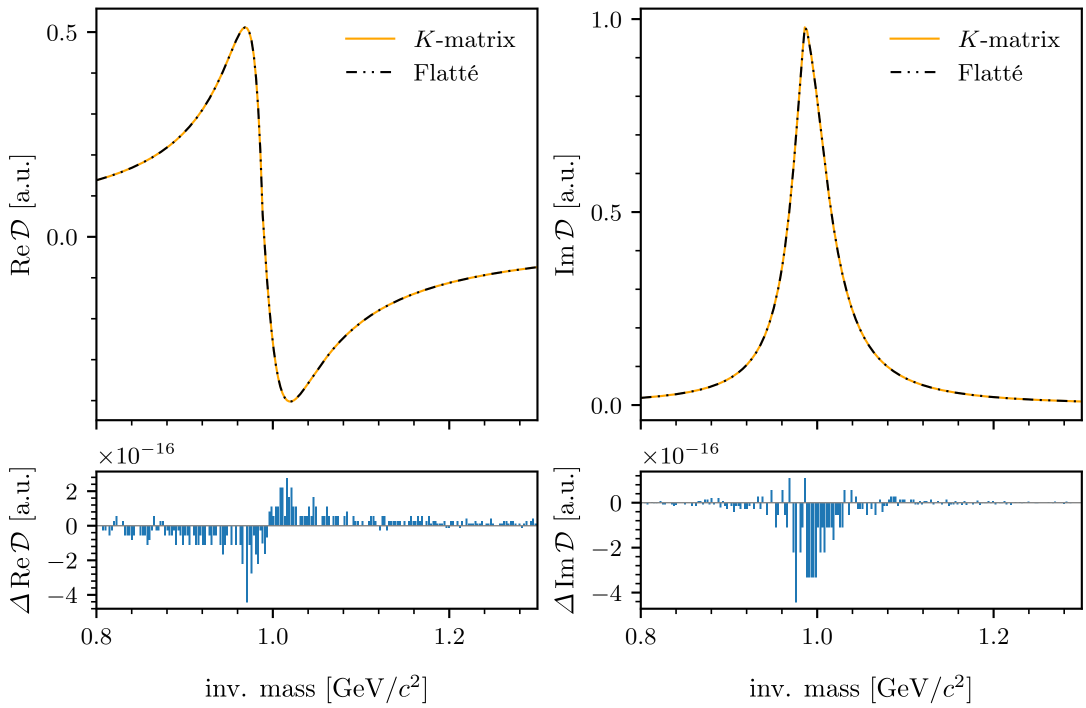

Figure C.2: Same as fig. 10.5, but for the cross check for a single pole decaying into two channels K-matrix in the P-vector approach.

List of Figures

List of Tables

Bibliography

[1] A. Einstein. “Zur Allgemeinen Relativitätstheorie.” In: *Sitzungsber. Preuss. Akad. Wiss. Berlin (Math. Phys.)* 1915 (1915). [Addendum: Sitzungsber. Preuss. Akad. Wiss. Berlin (Math. Phys.) 1915, 799–801 (1915)], pp. 778–786. URL: https://archive.org/details/sitzungsberichte1915deut/page/778/mode/2up.

[2] M. K. Gaillard, P. D. Grannis, and F. J. Sciulli. “The standard model of particle physics.” In: *Rev. Mod. Phys.* 71 (2 Mar. 1999), S96–S111. DOI: 10.1103/RevModPhys.71.S96.

[3] V. Trimble. “Existence and Nature of Dark Matter in the Universe.” In: *Ann. Rev. Astron. Astrophys.* 25 (1987), pp. 425–472. DOI: 10.1146/annurev.aa.25.090187.002233.

[4] L. Canetti, M. Drewes, and M. Shaposhnikov. “Matter and antimatter in the universe.” In: *New Journal of Physics* 14.9 (Sept. 2012), p. 095012. DOI: 10.1088/1367-2630/14/9/095012.

[5] W. E. Lamb and R. C. Retherford. “Fine Structure of the Hydrogen Atom by a Microwave Method.” In: *Phys. Rev.* 72 (1947), p. 241. DOI: 10.1103/PhysRev.72.241.

[6] H. A. Bethe. “The Electromagnetic Shift of Energy Levels.” In: *Phys. Rev.* 72 (1947), p. 339. DOI: 10.1103/PhysRev.72.339.

[7] M. Gell-Mann. “A Schematic Model of Baryons and Mesons.” In: *Phys. Lett.* 8 (1964), p. 214. DOI: 10.1016/S0031-9163(64)92001-3.

[8] G. Zweig. “An SU_3 model for strong interaction symmetry and its breaking. Version 1.” In: (1964). URL: https://cds.cern.ch/record/352337.

[9] K. G. Wilson. “Confinement of quarks.” In: *Phys. Rev. D* 10 (8 Oct. 1974), pp. 2445–2459. DOI: 10.1103/PhysRevD.10.2445.

[10] S. Navas et al. “Review of particle physics.” In: *Phys. Rev. D* 110 (2024), p. 030001. DOI: 10.1103/PhysRevD.110.030001.

[11] P. Abbon et al. “The COMPASS experiment at CERN.” In: *Nucl. Instrum. Meth. A* 577 (2007), p. 455. DOI: 10.1016/j.nima.2007.03.026.

[12] C. Adolph et al. "Resonance production and $\pi\pi$ S-wave in $\pi^- + p \to \pi^-\pi^-\pi^+ + p_{\text{recoil}}$ at 190 GeV/c." In: *Phys. Rev. D* 95 (2017), p. 032004. DOI: 10.1103/PhysRevD.95.032004.

[13] M. Aghasyan et al. "Light isovector resonances in $\pi^- p \to \pi^-\pi^-\pi^+ p$ at 190 GeV/c." In: *Phys. Rev. D* 98 (2018), p. 092003. DOI: 10.1103/PhysRevD.98.092003.

[14] G. D. Alexeev et al. "Spectroscopy of Strange Mesons and First Observation of a Strange Crypto-Exotic State with $J^P = 0^-$." In: (2025). paper submitted to PRL. arXiv: 2504.09470 [hep-ex].

[15] A. Abashian et al. "The Belle detector." In: *Nuclear Instruments and Methods in Physics Research Section A: Accelerators, Spectrometers, Detectors and Associated Equipment* 479.1 (2002). Detectors for Asymmetric B-factories, pp. 117–232. DOI: https://doi.org/10.1016/S0168-9002(01)02013-7.

[16] J. Brodzicka et al. *Physics Achievements from the Belle Experiment.* 2012. arXiv: 1212.5342 [hep-ex].

[17] A. Rabusov. "Partial-Wave Analysis of $\tau^- \to \pi^-\pi^-\pi^+\nu_\tau$ at Belle II." PhD thesis. Technical University of Munich, 2023. URL: https://mediatum.ub.tum.de/1715742.

[18] A. Rabusov, D. Greenwald, and S. Paul. "Measurement of the presence of $a_1(1420)$ and $\omega(782)$ in $\tau^- \to \pi^-\pi^+\pi^-\nu_\tau$ at Belle." In: *SciPost Phys. Proc.* 17 (2025), p. 008. DOI: 10.21468/SciPostPhysProc.17.008.

[19] S. U. Chung et al. "Partial wave analysis in K matrix formalism." In: *Annalen Phys.* 4 (1995), pp. 404–430. DOI: 10.1002/andp.19955070504.

[20] C. Adolph et al. "Observation of a New Narrow Axial-Vector Meson $a_1(1420)$." In: *Phys. Rev. Lett.* 115 (2015), p. 82001. DOI: 10.1103/PhysRevLett.115.082001.

[21] M. Mikhasenko, B. Ketzer, and A. Sarantsev. "Nature of the $a_1(1420)$." In: *Phys. Rev. D* 91.9 (2015), p. 094015. DOI: 10.1103/PhysRevD.91.094015. arXiv: 1501.07023 [hep-ph].

[22] J. D. Hansen, G. T. Jones, G. Otter, and G. Rudolph. "Formalism and assumptions involved in partial-wave analysis of three-meson systems." In: *Nucl. Phys.* B81 (1974), p. 403. DOI: 10.1016/0550-3213(74)90241-7.

[23] D. Herndon, P. Söding, and R. J. Cashmore. "Generalized isobar model formalism." In: *Phys. Rev. D* 11 (1975), p. 3165. DOI: 10.1103/PhysRevD.11.3165.

[24] C. Perez-Orive. *Personal communication.* 2025.

[25] M. Weiskopf. "Background Modeling in Partial-Wave Analysis of $\tau^- \to \pi^+\pi^-\pi^-\nu_\tau$ Decays at Belle II." Master's thesis. Technical University of Munich, May 2026. URL: https://docs.belle2.org/pub_data/documents/5209/.

[26] W. Altmannshofer et al. "The Belle II Physics Book." In: *PTEP* 2019.12 (2019). Ed. by E. Kou and P. Urquijo. [Erratum: PTEP 2020, 029201 (2020)], p. 123C01. DOI: 10.1093/ptep/ptz106. arXiv: 1808.10567 [hep-ex].

[27] T. Abe et al. "Belle II Technical Design Report." In: (Nov. 2010). arXiv: 1011.0352 [physics.ins-det].

[28] A. Olchevski, ed. *High-energy physics. Proceedings, European School, ESHEP'99, Casta-Papiernicka, Slovak Republic, August 22-September 4, 1999.* CERN Yellow Reports: School Proceedings. June 2000. DOI: 10.5170/CERN-2000-007.

[29] K. Akai, K. Furukawa, and H. Koiso. "SuperKEKB collider." In: *Nuclear Instruments and Methods in Physics Research Section A: Accelerators, Spectrometers, Detectors and Associated Equipment* 907 (2018). Advances in Instrumentation and Experimental Methods (Special Issue in Honour of Kai Siegbahn), pp. 188–199. DOI: https://doi.org/10.1016/j.nima.2018.08.017.

[30] KEK Accelerator Laboratory. *SuperKEKB Daily Snapshot*. URL: https://www-linac.kek.jp/skekb/snapshot/dailysnap.html (visited on 06/12/2026).

[31] T. Abe et al. "Achievements of KEKB." In: *Progress of Theoretical and Experimental Physics* 2013.3 (Mar. 2013), 03A001. DOI: 10.1093/ptep/pts102.

[32] Belle II Collaboration. *Luminosity Status*. URL: https://www.belle2.org/info/luminosity_status/ (visited on 06/12/2026).

[33] M. Bertemes. "Search for dark sector physics and performance of the Belle II detector in final state events with muons and large missing energy." PhD thesis. Vienna, Tech. U., Atominst., 2021.

[34] T. Hara, T. Kuhr, and Y. Ushiroda. *Belle II Coordinate System and Guideline of Belle II Numbering Scheme*. 2011. URL: https://indico.mpp.mpg.de/event/2308/contributions/4092/attachments/3414/3799/Belle2NumberingScheme.pdf (visited on 06/14/2026).

[35] S. Tavernier. "Detectors Based on Ionisation in Semiconductor Materials." In: *Experimental Techniques in Nuclear and Particle Physics*. Berlin, Heidelberg: Springer Berlin Heidelberg, 2010. DOI: 10.1007/978-3-642-00829-0_5.

[36] R. Pestotnik et al. "The aerogel Ring Imaging Cherenkov system at the Belle II spectrometer." In: *Nuclear Instruments and Methods in Physics Research Section A: Accelerators, Spectrometers, Detectors and Associated Equipment* 876 (2017). The 9th international workshop on Ring Imaging Cherenkov Detectors (RICH2016), pp. 265–268. DOI: https://doi.org/10.1016/j.nima.2017.04.043.

[37] G. Räuber. "Measurement of $|V_{us}|$ using hadronic tau decays at Belle II." PhD thesis. Vienna, Tech. U., 2024. DOI: 10.34726/hss.2024.111166.

[38] S. Wallner et al. *Event Selection of $\tau^\mp \to \pi^\mp\pi^\mp\pi^\pm\nu_\tau$ and Beyond*. Talk presented at the Belle II τ Group Meeting. Nov. 2024. URL: https://indico.belle2.org/event/13483/contributions/84117/.

[39] J. H. Kuhn and E. Mirkes. "Structure functions in τ decays." In: *Z. Phys. C* 56 (1992). [Erratum: Z.Phys.C 67, 364 (1995)], pp. 661–672. DOI: 10.1007/BF01474741.

[40] J. Kühn and E. Mirkes. "Angular distributions in semileptonic τ decays." In: *Physics Letters B* 286.3 (1992), pp. 381–386. DOI: https://doi.org/10.1016/0370-2693(92)91791-7.

[41] S. Brandt, C. Peyrou, R. Sosnowski, and A. Wroblewski. "The principal axis of jets — an attempt to analyse high-energy collisions as two-body processes." In: *Physics Letters* 12.1 (1964), pp. 57–61. DOI: https://doi.org/10.1016/0031-9163(64)91176-X.

[42] E. Farhi. "Quantum Chromodynamics Test for Jets." In: *Phys. Rev. Lett.* 39 (25 Dec. 1977), pp. 1587–1588. DOI: 10.1103/PhysRevLett.39.1587.

[43] Belle II Collaboration. *MVA Documentation* `basf2`. 2026. URL: https://software.belle2.org/development/sphinx/mva/doc/index-01-mva.html (visited on 06/16/2026).

[44] A. Katscho. "Selection of $\tau^\mp \to K^\mp\pi^\mp\pi^\pm\nu_\tau$ Decays for Data from the Belle II Experiment." Bachelor's thesis. Technical University of Munich, Nov. 2024.

[45] Belle II Collaboration. *Variables Documentation* `basf2`. 2026. URL: https://software.belle2.org/development/sphinx/analysis/doc/Variables.html#variable-kaonIDNN (visited on 06/16/2026).

[46] G. Cordes. "Studying Detector Simulation Corrections for $\tau^- \to \pi^-\pi^-\pi^+\nu_\tau$ Decays at Belle II." Bachelor's thesis. Technical University of Munich, May 2025.

[47] G. Alexander et al. "Evidence for the $\tau \to \nu\rho\pi$ decay mode." In: *Physics Letters B* 73.1 (1978), pp. 99–104. DOI: https://doi.org/10.1016/0370-2693(78)90181-8.

[48] D. M. Asner et al. "Hadronic structure in the decay $\tau^- \to \nu_\tau\pi^-\pi^0\pi^0$ and the sign of the tau neutrino helicity." In: *Phys. Rev. D* 61 (1 Dec. 1999), p. 012002. DOI: 10.1103/PhysRevD.61.012002.

[49] F. Von Hippel and C. Quigg. "Centrifugal-Barrier Effects in Resonance Partial Decay Widths, Shapes, and Production Amplitudes." In: *Phys. Rev. D* 5 (1972), p. 624. DOI: 10.1103/PhysRevD.5.624.

[50] J. M. Blatt and V. F. Weisskopf. *Theoretical nuclear physics*. New York: Springer, 1952. DOI: 10.1007/978-1-4612-9959-2.

[51] B. Ketzer, B. Grube, and D. Ryabchikov. "Light-meson spectroscopy with COMPASS." In: *Prog. Part. Nucl. Phys.* 113 (2020), p. 103755. DOI: 10.1016/j.ppnp.2020.103755.

[52] F. Krinner and S. Paul. "Hadronic currents and form factors in three-body semileptonic τ decays." In: *Eur. Phys. J. C* 81 (2021), p. 1073. DOI: 10.1140/epjc/s10052-021-09876-1.

[53] H. Aihara et al. *The Belle II Detector Upgrades Framework Conceptual Design Report*. 2024. arXiv: 2406.19421 [hep-ex].

[54] C. P. Robert and G. Casella. "Monte Carlo Integration." In: *Monte Carlo Statistical Methods*. New York, NY: Springer New York, 1999, pp. 71–138. DOI: 10.1007/978-1-4757-3071-5_3.

[55] G. J. Gounaris and J. J. Sakurai. "Finite width corrections to the vector meson dominance prediction for $\rho \to e^+e^-$." In: *Phys. Rev. Lett.* 21 (1968), pp. 244–247. DOI: 10.1103/PhysRevLett.21.244.

[56] R. Barate et al. "Measurement of the spectral functions of vector current hadronic tau decays." In: *Z. Phys. C* 76 (1997), pp. 15–33. DOI: 10.1007/s002880050523.

[57] S. M. Flatté. "On the nature of 0^+ mesons." In: *Phys. Lett. B* 63 (1976), p. 228. DOI: 10.1016/0370-2693(76)90655-9.

[58] M. Ablikim et al. "Resonances in $J/\psi \to \phi\pi^+\pi^-$ and ϕK^+K^-." In: *Phys. Lett. B* 607 (2005), p. 243. DOI: 10.1016/j.physletb.2004.12.041.

[59] K. L. Au, D. Morgan, and M. R. Pennington. "Meson dynamics beyond the quark model: Study of final-state interactions." In: *Phys. Rev. D* 35 (1987), p. 1633. DOI: 10.1103/PhysRevD.35.1633.

[60] Igor A. Kachaev. "Structure of $\pi\pi$ S-wave in $\pi^+\pi^-\pi^-$ system." In: *3rd International Conference on Quarks and Nuclear Physics QNP*. Bloomington, IN, U.S.A., 2004.

[61] T. A. Collaboration. "An implementation of neural simulation-based inference for parameter estimation in ATLAS." In: *Reports on Progress in Physics* 88.6 (May 2025), p. 067801. DOI: 10.1088/1361-6633/add370.

[62] K. Cranmer, J. Pavez, and G. Louppe. *Approximating Likelihood Ratios with Calibrated Discriminative Classifiers*. 2016. arXiv: 1506.02169 [stat.AP].

[63] H. Dembinski and P. O. Et al. "scikit-hep/iminuit." In: (2020). DOI: 10.5281/zenodo.3949207.

[64] F. James and M. Roos. "Minuit - a system for function minimization and analysis of the parameter errors and correlations." In: *Computer Physics Communications* 10.6 (1975), pp. 343–367. DOI: https://doi.org/10.1016/0010-4655(75)90039-9.

[65] N. Braun, M. Eliachevitch, and The Belle II Collaboration. *b2luigi*. Version 1.2.4. GPLv3. 2025. URL: https://github.com/belle2/b2luigi/releases/tag/v1.2.4.

[66] N. Braun, M. Eliachevitch, and The Belle II Collaboration. *b2luigi Documentation*. https://b2luigi.belle2.org. Accessed: 2026-06-21.

[67] E. Bernhardsson, E. Freider, and Spotify. *luigi.* Accessed: 2026-06-21. 2012. URL: https://github.com/spotify/luigi.

[68] S. A. Dupree and S. K. Fraley. "Monte Carlo Sampling Techniques." In: *A Monte Carlo Primer: A Practical Approach to Radiation Transport.* Boston, MA: Springer US, 2002, pp. 21–56. DOI: 10.1007/978-1-4419-8491-3_2.

[69] L. Demortier and L. Lyons. "Everything you always wanted to know about pulls." In: URL: https://api.semanticscholar.org/CorpusID:19545670.

[70] M. G. Alexeev et al. "Triangle Singularity as the Origin of the $a_1(1420)$." In: *Phys. Rev. Lett.* 127 (2021), p. 82501. DOI: 10.1103/PhysRevLett.127.082501.

[71] S. U. Chung and T. L. Trueman. "Positivity conditions on the spin density matrix: A simple parametrization." In: *Phys. Rev. D* 11 (1975), p. 633. DOI: 10.1103/PhysRevD.11.633.

[72] F. Krinner. "Freed-Isobar Partial-Wave Analysis." Ph.D. thesis. TU München, 2018. URL: https://cds.cern.ch/record/2783415.

[73] F. Krinner et al. "Ambiguities in model-independent partial-wave analysis." In: *Phys. Rev. D* 97 (2018), p. 114008. DOI: 10.1103/PhysRevD.97.114008.

[74] K. Chen, C.-Q. Pang, X. Liu, and T. Matsuki. "Light axial vector mesons." In: *Phys. Rev. D* 91 (7 Apr. 2015), p. 074025. DOI: 10.1103/PhysRevD.91.074025.

[75] A. V. Anisovich, V. V. Anisovich, and A. V. Sarantsev. "Systematics of $q\bar{q}$ states in the (n, M^2) and (J, M^2) planes." In: *Phys. Rev. D* 62 (5 July 2000), 051502(R). DOI: 10.1103/PhysRevD.62.051502.

[76] Z.-G. Wang. "Light axial-vector tetraquark state candidate: $a_1(1420)$." In: (Jan. 2014). arXiv: 1401.1134 [hep-ph].

[77] J.-L. Basdevant and E. L. Berger. "The twofold emergence of the a_1 axial vector meson in high energy hadronic production." In: (Jan. 2015). arXiv: 1501.04643 [hep-ph].

[78] J.-L. Basdevant and E. L. Berger. "Peak Locations and Relative Phase of Different Decay Modes of the a_1 Axial Vector Resonance in Diffractive Production." In: *Phys. Rev. Lett.* 114 (19 May 2015), p. 192001. DOI: 10.1103/PhysRevLett.114.192001.

[79] M. Wagner, M. Mikhasenko, B. Ketzer, and the hadron analysis subgroup. *Mass-dependent fit of $a_1(1420)$ via the "Triangle Singularity".* COMPASS Release Note. Internal document, restricted access. COMPASS Collaboration, 2017.

[80] M. Ablikim et al. "Resonances in $J/\psi \to \phi\pi^+\pi^-$ and ϕK^+K^-." In: *Phys. Lett. B* 607 (2005), pp. 243–253. DOI: 10.1016/j.physletb.2004.12.041. arXiv: hep-ex/0411001.

[81] I. Aitchison. "The K-matrix formalism for overlapping resonances." In: *Nuclear Physics A* 189.2 (1972), pp. 417–423. DOI: https://doi.org/10.1016/0375-9474(72)90305-3.

[82] R. T. Deck. “Kinematical Interpretation of the First π-ρ Resonance.” In: *Phys. Rev. Lett.* 13 (1964), p. 169. DOI: 10.1103/PhysRevLett.13.169.

[83] M. G. Bowler. “A Simple Analytic Treatment of Rescattering Effects in the Deck Model.” In: *J. Phys. G* 5 (1979), p. 203. DOI: 10.1088/0305-4616/5/2/007.

[84] M. G. Bowler, M. A. V. Game, I. J. R. Aitchison, and J. B. Dainton. “Diffraction Dissociation, the Deck Mechanism and Diffractive Resonance Production.” In: *Nucl. Phys. B* 97 (1975), pp. 227–255. DOI: 10.1016/0550-3213(75)90033-4.

[85] F. U. Bernlochner and S. Wallner. “Role of $\rho - \omega$ interference in semileptonic $B \to \pi^+\pi^-\ell\bar{\nu}_\ell$ decays.” In: *Phys. Rev. D* 109 (2024), p. 074040. DOI: 10.1103/PhysRevD.109.074040.

[86] A. M. Badalian, L. P. Kok, M. I. Polikarpov, and Y. A. Simonov. “Resonances in Coupled Channels in Nuclear and Particle Physics.” In: *Phys. Rept.* 82 (1982), pp. 31–177. DOI: 10.1016/0370-1573(82)90014-X.

[87] IEEE Standards Association. “IEEE Standard for Floating-Point Arithmetic.” In: *IEEE Std 754-2019 (Revision of IEEE 754-2008)* (2019), pp. 1–84. DOI: 10.1109/IEEESTD.2019.8766229.

Acknowledgments

Above all, I would like to thank Prof. Stephan Paul and Dr. Hans-Günther Moser for providing the opportunity to work on such an interesting topic. It was a pleasure, and I learned a great deal about collaborative work and about how analyses are carried out.

I am deeply grateful for the guidance Dr. Stefan Wallner provided to me, not only throughout this master's thesis but ever since we started working together more than four years ago. You always had an answer to my problems, while helping me understand the deeper issue behind them, and you consistently challenged my knowledge to deepen my understanding of the topic. Thanks to you, I learned a great deal about high-energy particle physics, and you sparked my interest in continuing as a PhD student in the field. I hope we have many more years of working together within the Belle II collaboration.

I would also like to thank the whole Belle II MPP group. I had a lot of fun on our trips to Japan and to the DPG in Erlangen, and you made the whole time truly enjoyable. In particular, I would like to thank my two office mates, Dr. Justin Skorupa and Martin Bartl, for their tireless willingness to answer every question I thought was too stupid to ask Stefan. I would also like to thank Robert Mundzeck for taking over my work and continuing on the topic. It is always a pleasure discussing the physics with you, and I hope you will have as much fun during your master's thesis as I had during mine. Lastly, I would like to thank Miriam Weiskopf. It was a real pleasure working with you on this topic, and I enjoyed our discussions not only on the physics but also on everything else, from finding PhD positions to life in general.
To all of you: I wish you the best, and I hope we meet again at collaboration meetings or that we continue working together.

Special thanks to my friends Jakob Gerstmayer and Paul Odendahl for proofreading the thesis and for many never-ending, enjoyable discussions.

Finally, and most importantly, I would like to thank my parents. You have always given me your love and the confidence that I would find my way, and it is only thanks to you that I am the person I am today.